ANL/FE--90/2

DE91 005749

ARGONNE NATIONAL LABORATORY
9700 South Cass Avenue, Argonne, Illinois 60439

ANL/FE-90/2

THE ROLE OF Zr AND Nb IN OXIDATION/SULFIDATION BEHAVIOR OF Fe–Cr–Ni ALLOYS

by

K. Natesan and D. J. Baxter*

Materials and Components Technology Division

November 1990

Work sponsored by

U.S. DEPARTMENT OF ENERGY
Office of Fossil Energy
Advanced Research and Technology Development Materials Program

*INCO Alloy Limited, Hereford, England.

CONTENTS

FIGURES

TABLES

THE ROLE OF Zr AND Nb IN OXIDATION/SULFIDATION BEHAVIOR OF Fe–Cr–Ni ALLOYS

by

K. Natesan and D. J. Baxter

Abstract

Structural Fe-Cr-Ni alloys may undergo rapid degradation at elevated temperatures unless protective surface oxide scales are formed and maintained. The ability of alloys to resist rapid degradation strongly depends on their Cr content and the chemistry of the exposure environment. Normally, 20 wt.% Cr is required for service at temperatures up to 1000°C; the presence of sulfur, however, inhibits formation of a protective surface oxide scale. The oxidation and sulfidation behavior of Fe-Cr-Ni alloys is examined over a wide temperature range (650 to 1000°C), with particular emphasis on the effects of alloy Cr content and the addition of reactive elements such as Nb and Zr. Both Nb and Zr are shown to promote protective oxidation behavior on the 12 wt.% Cr alloy in oxidizing environments and to suppress sulfidation in mixed oxygen/sulfur environments. Additions of Nb and Zr at 3 wt.% level resulted in stabilization of Cr_2O_3 scale and led to a barrier layer of Nb- or Zr-rich oxide at the scale/metal interface, which acted to minimize the transport of base metal cations across the scale. Oxide scales were preformed in sulfur-free environments and subsequently exposed to oxygen/sulfur mixed-gas atmospheres. Preformed scales were found to delay the onset of breakaway corrosion. Corrosion test results obtained under isothermal and thermal cycling conditions are presented.

1 Background

The resistance of structural alloys to rapid degradation in aggressive environments at elevated temperatures usually depends on the ability of the alloys to form and maintain protective surface oxide scales. Cr_2O_3 is expected to be the predominant constituent of protective scales on Fe-Cr-Ni alloys. In gaseous environments typical of those encountered in high-temperature coal gasifiers, experience shows that a thermodynamically stable protective oxide may not form because of the sulfur that originated as an impurity in the coal feedstock.[1] An excess concentration of oxygen above the level associated with the Cr_2O_3-"CrS" equilibrium is required for Cr_2O_3 to form a continuous, rate-controlling layer under practical conditions. The threshold oxygen partial pressure (pO_2) for protective scale formation on Fe-Cr-Ni alloys is generally 10^3 to 10^5 times the Cr_2O_3-"CrS" equilibrium level in the temperature range of 650 to 1000°C.[2-4] The experimentally determined boundaries[2,3] that separate the oxide- and sulfide-scale-forming regions are termed "kinetic boundaries" (see Fig. 1). In the absence of protective oxide layers, the rates of alloy degradation due to sulfur attack are prohibitively high for practical applications.

Research sponsored by the U. S. Department of Energy, Fossil Energy AR&TD Materials Program, DOE/FE AA 15 10 10 0, Work Breakdown Structure Element ANL–3.

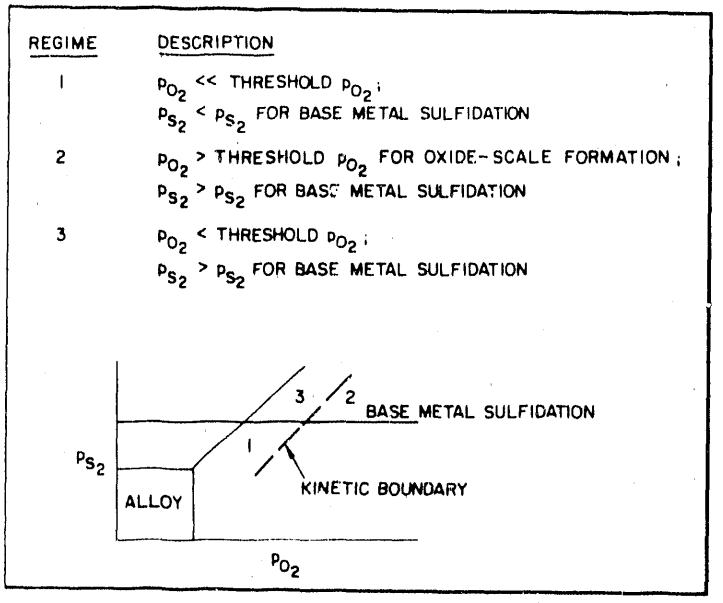

Fig. 1.
Schematic diagram depicting different regions of corrosion-product development

Alloy composition plays an important role in averting rapid alloy degradation. A minimum Cr content of 14 wt.% should allow a protective scale to form on austenitic Fe base alloys in a CO/CO_2 environment at 850°C,[5] although significantly higher levels are usually considered necessary for long-term scale stability and for protection at higher temperatures. Stable oxide-forming elements can promote the formation of protective oxide scales[6] and change the growth mechanism and mechanical behavior of the oxide.[7-9]

The mechanism by which the corrosion process proceeds in a given alloy is strongly dependent on both the alloy chemistry and the oxygen/sulfur partial pressures in the exposure environment. For example, in the case of chromia-forming alloys, competition between oxide and base-metal sulfide determines the type of scale that forms on a metal surface when the exposure environment has a sulfur partial pressure higher than that for base-metal sulfide formation (and to the left of the kinetic boundary in Fig. 1). On the other hand, under exposure conditions that depict sulfur partial pressure (pS_2) above the base-metal sulfidation potential (and to the right of the kinetic boundary in Fig. 1), the same alloys develop oxide scales. The threshold pO_2 values for oxide formation are temperature-dependent, but are influenced little by the chromium content in the range of 20-50 wt.%. Minor alloying additions primarily influence the type (binary oxides, spinels, and duplex layers) and porosity of the scales, as well as the adhesion of the oxide scale to the substrate material. Even if an alloy develops a protective oxide scale after short-term exposures to mixed-gas environments, the long-term behavior and thus life expectation for the alloy is strongly dependent on whether the alloy exhibits "breakaway" or "accelerated" corrosion.

Several possible breakaway processes can be identified, including:

1. Mechanical and thermal-cycling damage.
2. Development of short-circuit and impurity transport paths in the oxide scale.
3. Changes in the oxide composition with time.
4. Depletion of the protective scale-forming element in the substrate as a result of repeated spalling and reforming of the protective scale.

5. Transport of base-metal cations through the oxide scale to the gas/scale interface and subsequent sulfidation of these elements.

6. Transport of sulfur through the oxide scale into the substrate and sulfidation of the chromium- or aluminum-depleted (i.e., Fe-, Ni-, Co-enriched) region in the vicinity of the scale/metal interface.

In general, most of the alloys exhibit breakaway corrosion, especially in oxygen/sulfur mixed-gas atmospheres; the exposure time at which it occurs is dependent on temperature, gas chemistry, alloy composition, and scale microstructure. In most applications of heat-resistant alloys, the materials are subjected to temperature-cycling conditions. Breakdown of scales can occur due to the difference in thermal expansion properties between scales and alloy substrates and due to growth stresses that are generated during oxidation. Baxter and Natesan have discussed various mechanical considerations in the degradation of structural materials exposed to several environments at elevated temperatures.[10]

In the presence of oxygen/sulfur mixed-gas atmospheres, processes 2 through 6 above can play dominant roles in the initiation of breakaway corrosion in structural alloys. In numerous studies, oxide scales were preformed in sulfur-free low-pO_2 gas atmospheres, and the preoxidized specimens were subsequently exposed to sulfur-containing atmospheres (e. g., O_2-SO_2, H_2-H_2S, H_2-H_2O-H_2S) to examine the role of various processes in initiating breakaway corrosion.[11-16] The effect of initial composition of preformed oxide scale on breakaway corrosion of Incoloy 800 and pure Cr specimens has been studied by Natesan.[13,17] The preformed oxide scales on Incoloy 800 consisted of (Cr,Mn) spinel, while those on pure Cr specimens were Cr_2O_3. Exposure of the preoxidized specimens to oxygen/sulfur mixed-gas atmospheres resulted in the formation of (Mn,Cr) sulfide crystals on the external surface, whereas the oxide underneath consisted of (Cr,Mn) oxide. The sulfide crystals were located predominantly at the preformed-oxide/gas interface, and virtually no sulfur was detected either in the oxide itself or in the substrate alloy.

For pure Cr specimens, the preoxidized layer consisted of Cr_2O_3, and subsequent exposure of the specimens to sulfur-containing environments resulted in only Cr sulfide particles at the Cr oxide/gas interface. Although the scale structure exhibited discrete particles of Cr_2O_3 with some porosity, no sulfur was detected in the interior of the scale, indicating that the scale formation in mixed gas is largely determined by Cr rather than by S diffusion in the Cr_2O_3 scale. Similar observations have been reported by LaBranche et al., who also concluded that once the initial oxide spalls, the scale formed during subsequent exposure is a mixture of oxide and sulfide.[18] This scale is nonprotective and leads to accelerated corrosion.

Another aspect of the oxidation/sulfidation of structural alloys is the transport of the more noble base-metal elements such as Fe, Ni, and Co from the substrate to the gas/scale interface. Extensive studies have been conducted on preformed oxide scales for a variety of commercial and model alloys.[11-17] Failure of iron-base alloys exposed to oxygen/sulfur mixed-gas atmospheres (with the low pO_2 typical of coal gasification processes) was predominantly due to the nucleation and growth of base-metal sulfides on the surface of an otherwise protective oxide scale. Prater and Baer preoxidized a sputter-deposited, fine-grain Type 304 stainless steel and subsequently exposed the specimen to an H_2S-containing atmosphere.[16] Sulfur was found on the surface of the oxidized specimen and it enhanced

transport of iron to the scale surface. The mode of iron transport through the scale was not identified; however, the experiment showed convincingly that sulfur present in the external gas phase was influential in drawing iron preferentially to the scale surface.

Huang et al. examined the oxidation/sulfidation behavior of preoxidized Fe-30 wt.% Cr and Co-30 wt.% Cr alloys in H_2-H_2O-H_2S atmospheres.[11] X-ray photoelectron spectroscopy (XPS) and Auger electron spectroscopy (AES) of the Fe-Cr alloy specimens showed significant iron transport outward from the substrate through the Cr_2O_3 scale to the gas/scale interface, which eventually formed (Fe,Cr) sulfide. The study also concluded that the predominant mode of failure of scales is due to iron transport outward rather than to sulfur transport inward. Natesan examined the influence of sulfur in the gas environment on the chemical changes in preformed Cr–oxide scales on a high-purity Fe-25 wt.% Cr- 20 wt.% Ni alloy.[19] The XPS technique was used to evaluate the compositional changes at the scale surfaces. Figure 2 shows the XPS spectra of surfaces of preformed oxide layers before and after exposure to sulfur-containing environments. Also shown in the figure for comparison are the spectra for the Cr_2O_3 and Cr_2S_3 phases. The data, with a lineup of Cr 3p peaks, show that the counts for Fe 3p increase with an increase in time of exposure in a sulfur-containing atmosphere. In addition, with an increase in the Fe 3p peak, the S 3s peak also increases, indicating that sulfur adsorption is associated with the iron content of the oxide surface. Figure 3 shows the counts as a function of binding energy for Fe 2p in the two states, normalized with respect to the chromium peak. With such a normalization procedure, the Fe/Cr ratio at the surface of the oxide scale can be quantified as shown in the figure. With an increase in exposure time to a sulfur-containing environment, the Fe/Cr ratio increases by a factor of 4.5 after 24 h. Enrichment of iron at the gas/oxide scale interface is an essential step in the eventual breakdown of the scale in the bioxidant environments.

In general, the diffusivities of various elements in decreasing order are: $D_{Mn} > D_{Fe} > D_{Cr} > D_{Co} > D_{Ni}$. As a result, even among chromia-forming alloys, high iron- and manganese–containing alloys are much more susceptible to sulfidation than are the cobalt- and nickel-base alloys. Sulfur, however, can and does transport through chromia scales, and the formation of low-melting nickel/nickel sulfide eutectic in the vicinity of the scale/substrate interface can lead to catastrophic corrosion in nickel-base alloys.

Although the onset of breakaway corrosion is difficult to predict, studies have been conducted to determine the morphological changes that occur when structural alloys are exposed to mixed-gas atmospheres and to develop approaches to extend the time of initiation of breakaway corrosion. Natesan and Baxter studied morphological developments (see Fig. 4) in a high-purity Fe-25 wt.% Cr-20 wt.% Ni alloy by preoxidizing specimens for 72 h in a sulfur-free low-pO_2 environment and subsequently exposing them to a sulfur-containing atmosphere for time periods of 5, 7, and 22 h.[20] Preoxidation of the alloy in a low-pO_2 (2×10^{-18} atm) environment resulted in an external Cr_2O_3 scale of ≈4 μm in thickness. After a 5-h exposure to a sulfur–containing atmosphere, the preoxidized specimen developed an (Fe,Cr) sulfide phase at the gas/scale interface, indicating significant transport of Fe and Cr through the oxide scale and subsequent sulfidation of the transported elements. Small precipitates of Cr-rich sulfide particles were also observed at the grain boundaries in the substrate material, indicating some transport of sulfur inwards. After a 7-h exposure, the continuous oxide scale was breached, and sulfidation occurred at the substrate/oxide interface. The sulfide particles at the grain boundaries became larger

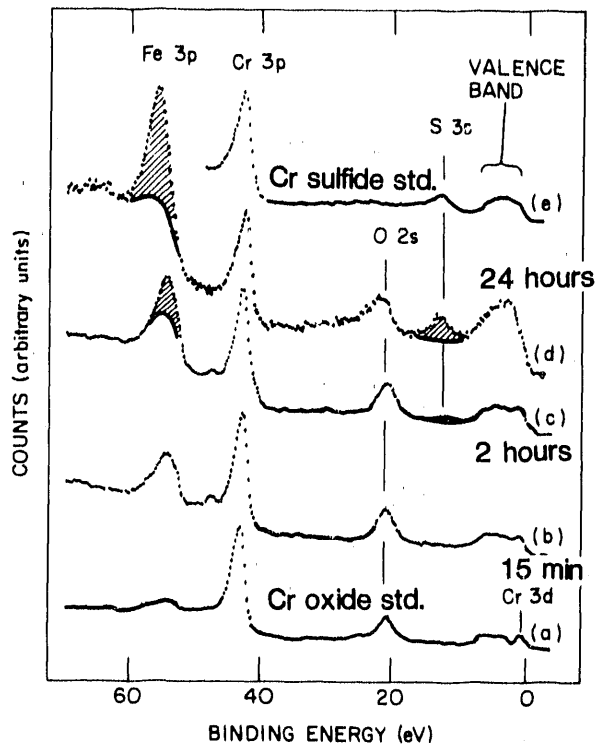

Fig. 2.
X-ray photoelectron spectroscopy data for surfaces of preformed oxide layers before and after exposure to sulfur-containing environments

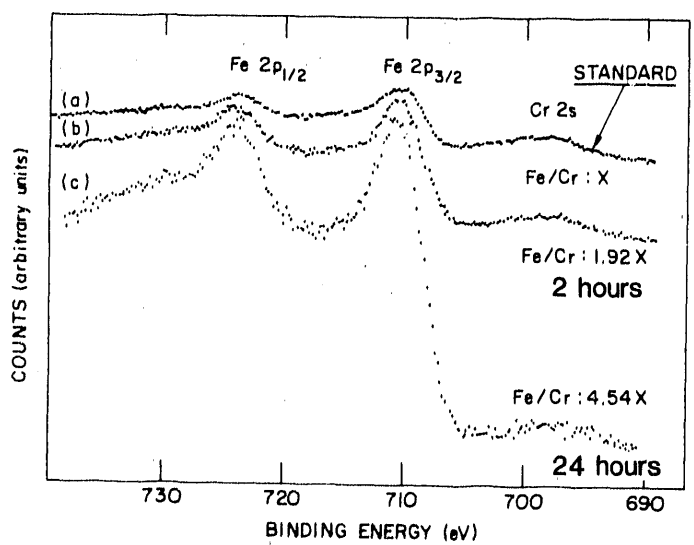

Fig. 3.
X-ray photoelectron spectroscopy counts as a function of binding energy for the Fe 2p in two states, normalized with respect to chromium peak

due to increased sulfur penetration. After 22 h of exposure, the oxide scale was virtually destroyed, and the scale consisted predominantly of (Fe,Cr) sulfide accompanied by substantial internal sulfidation of the alloy.

Figure 5 is a schematic representation of corrosion scale development and morphological changes that occur in Cr_2O_3-forming alloys exposed to low-pO_2 and moderate-to-high pS_2 atmospheres at elevated temperatures. The alloy in the early stages of exposure develops oxide and sulfide nuclei. Eventually, the thermodynamic conditions establish a continuous Cr_2O_3 scale via reoxidation of sulfide particles, while the released sulfur is driven into the substrate along the grain boundaries. Oxide growth occurs via chromium transport across the scale to the scale/gas interface, where it is oxidized, leading to

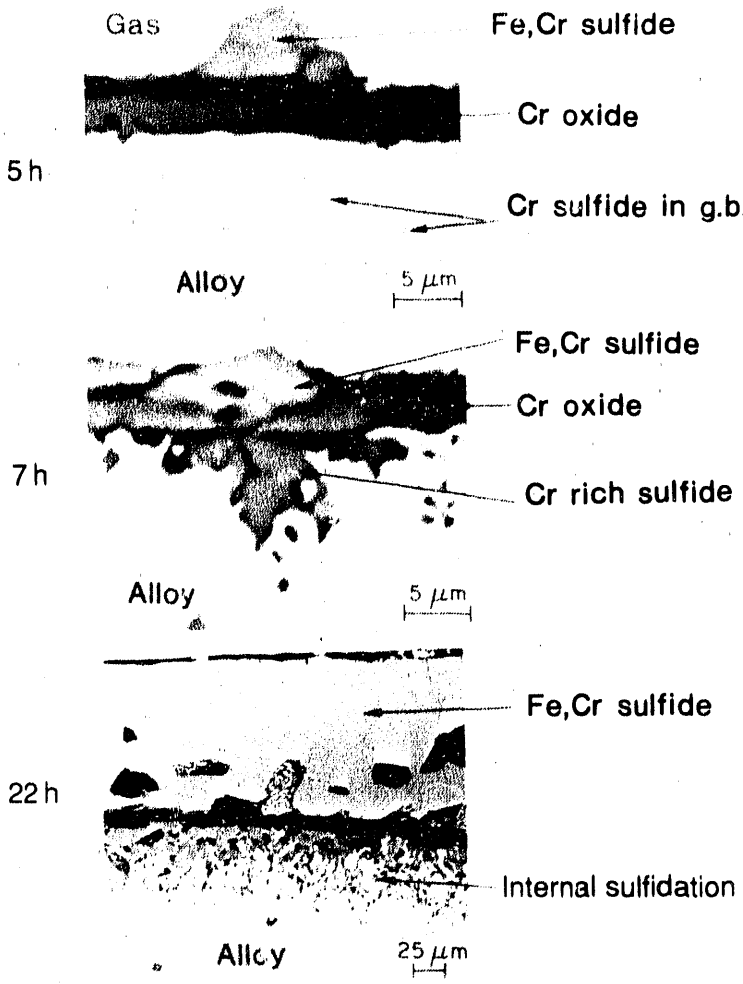

Fe–25Cr–20Ni
Preoxidized for 72 h (p_{O2} = 2 x 10^{-18} atm)
Sulfidized for times shown (p_{S2} = 4 x 10^{-8} atm)

Fig. 4. Morphological changes observed in an Fe–25 wt.% Cr-20 wt.% Ni specimen pre-oxidized in low-pO_2 atmosphere and subsequently exposed to sulfur-containing atmosphere for different times at 875°C

increased thickness. At the same time, sulfur in the gas phase is adsorbed onto the scale/gas interface, and channels are established in the fine-grain oxide scale through which transport of base-metal cations (Cr, Fe, Ni, Co, etc.) to the scale/gas interface is accentuated. If the sulfur pressure in the gas phase exceeds the metal/metal sulfide equilibria for the base-metal elements, their sulfides form at the oxide scale/gas interface. As the sulfide grows, stresses develop in the oxide and the oxide scale is breached, thereby resulting in sulfidation at the oxide scale/substrate interface. Because transport rates of cations and sulfur through the sulfide phase are orders of magnitude faster than those through the oxide scale, sulfidation attack continues in an accelerated manner. At longer exposure times, the oxide is virtually destroyed, and a massive sulfide scale develops -- a condition that represents breakaway corrosion for the alloy.

Based on the information reviewed thus far, it is evident that a viable alloy for application in bioxidant environments at elevated temperatures should develop protective oxide scales in the exposure environment. The long-term performance of an alloy, even if it initially develops an oxide scale, will be determined by the onset of breakaway corrosion in the service environment. Three avenues to minimize the outward transport of cations and

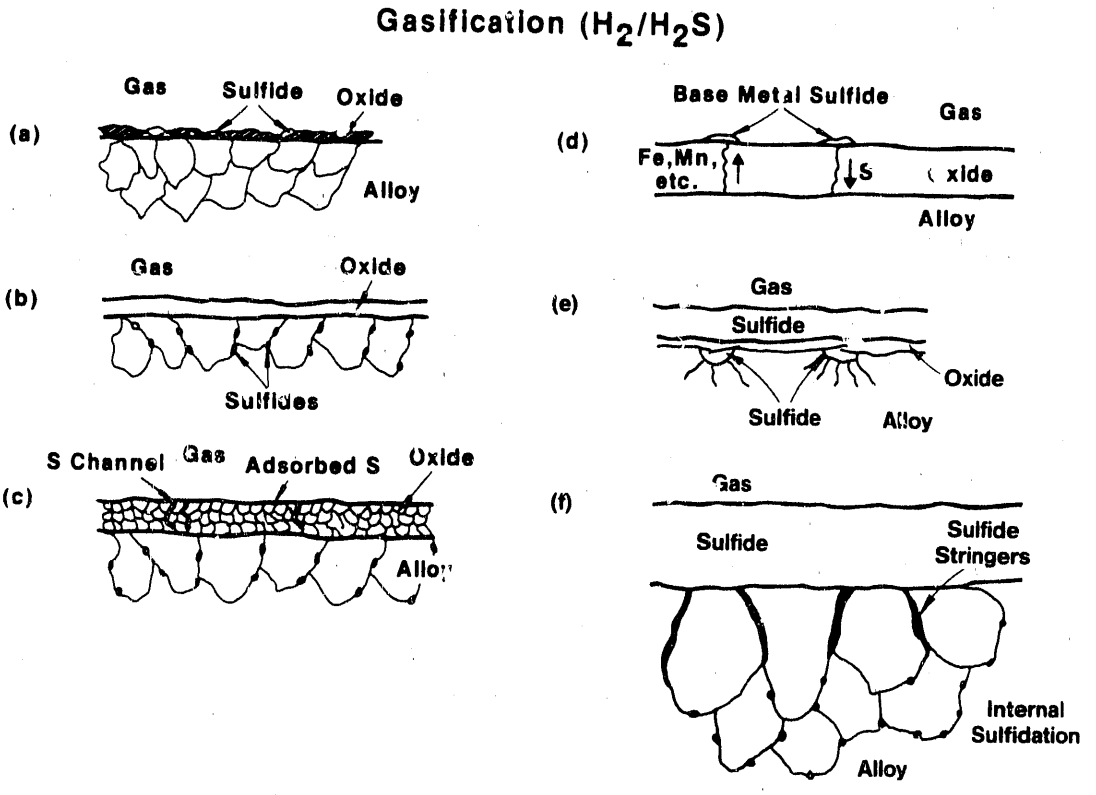

Fig. 5. Schematic representation of reaction sequence for chromia-forming alloys exposed to low-pO_2 and moderate-to-high pS_2 environments

inward transport of sulfur can be envisioned: (1) development of a scale whose growth rate is faster than the transport rate of either base-metal elements or sulfur; (2) control of the scale microstructure (grain size, grain boundary distribution, porosity, beneficial segregation, etc.) to minimize cation and sulfur transport through the scales; and (3) development of a barrier layer, which may or may not be oxide, with an inherently lower diffusivity for cations and sulfur and that has adequate adhesion to the external scale and the substrate material. In general, avenue 1 can rarely be achieved in chromia-forming alloys. Other scales such as refractory metal oxides should be examined; however, a higher growth rate of oxide will lead to thicker scales that may be susceptible to mechanically or thermally induced spallation. Control of microstructure (avenue 2) has potential as a means to minimize breakaway corrosion, and the influence of various physical and chemical parameters on the scale morphology and microstructure needs to be understood and quantified. The concept of a barrier layer (avenue 3) has much greater potential, especially if the barriers can be developed during exposure in the service environment. Alloying elements, which are potential in forming barrier layers, can be added to the base alloy via bulk alloying approach.

Because the mode of interaction of heat-resistant materials with oxygen/sulfur mixed-gas environments is the formation of chromium-rich oxide or chromium-rich sulfide, it is pertinent to consider the thermodynamic stability of the oxides and sulfides of other alloying elements relative to those of chromium. Elements that form oxides and sulfides of greater stability than those of chromium are indicated in Fig. 6. Manganese and silicon,

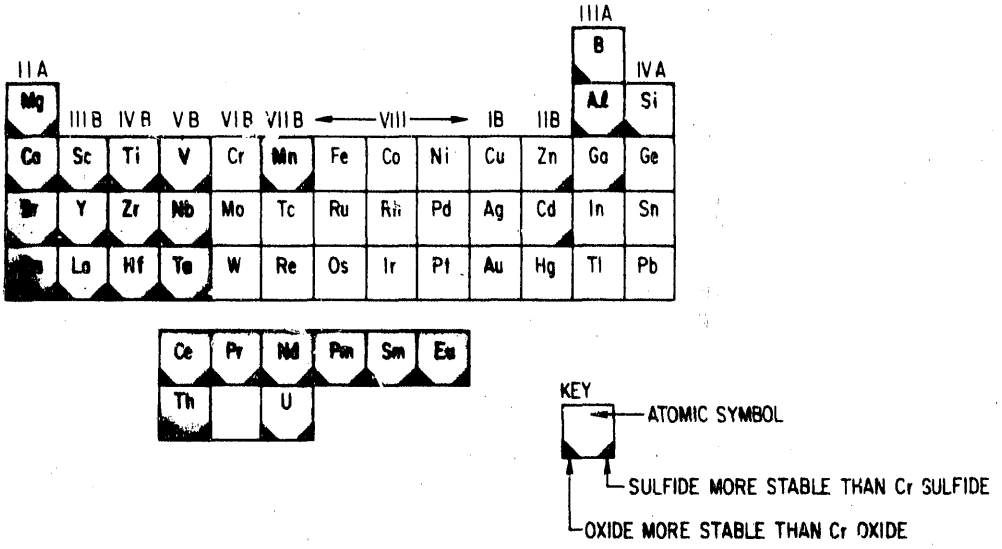

Fig. 6. Periodic table showing elements that form oxides and sulfides of greater stability than those of chromium

which form oxides that are more stable than chromium oxide, have a tendency to migrate from the bulk of the alloy to the scale/substrate interface. However, at high concentrations, the formation of manganese sulfide is a distinct possibility that would lead to enhanced corrosion rates, as observed by Perkins and Bhat.[21] In the oxide mode of interaction, manganese preferentially segregates in the scale and has an adverse effect on the scale spallation, leading to enhanced corrosion rates. A silicon content of up to 4 wt.% is beneficial for the formation of protective layers in oxidation studies; however, the mobility of Si (because of its much larger ionic radius) is much lower than those of Fe, Cr, and Mn. Consequently, formation of an external silica scale is virtually impossible even in high-silicon alloys. Silicon generally segregates to the oxide/alloy interface, especially in chromia-forming alloys. In fact, in the majority of corrosion/mechanical-property tests conducted on silicon-containing alloys exposed to oxygen/sulfur mixed-gas atmospheres in the temperature range of 750 to 982°C, the alloys developed sulfide scales, and silicon in the alloy rarely had any beneficial effect in protective scale development.

Refractory metals such as Ti, Zr, V, and Ta can form oxides and sulfides that exhibit greater thermodynamic stability than do chromium oxide and sulfide. On the other hand, chromium oxide and sulfide phases are more stable than sulfides and oxides of metals such as Mo and W. Figure 7 shows a comparison of thermogravimetric test data for several refractory metals/alloys with those for conventional alloys exposed to mixed-gas atmospheres with a relatively high pS_2 of 9.4×10^{-7} atm at 871°C. The morphology of the exposed specimens (see Figs. 8 and 9) shows that Incoloy 800 and Type 310 stainless steel undergo catastrophic sulfidation corrosion, whereas metals such as Ta, V, and Nb exhibit oxidation attack. Among these, only Ta developed a nonprotective oxide scale that contained substantial internal cracking. Vanadium developed a subscale of sulfide, indicative of the less protective nature of vanadium oxide. No sulfur was detected in the niobium specimen. Molybdenum and TZM develop very thin, adherent sulfide scales. The parabolic rate constants[22] for the oxidation/sulfidation reactions for several of these metals/alloys and for chromium are listed in Table 1.

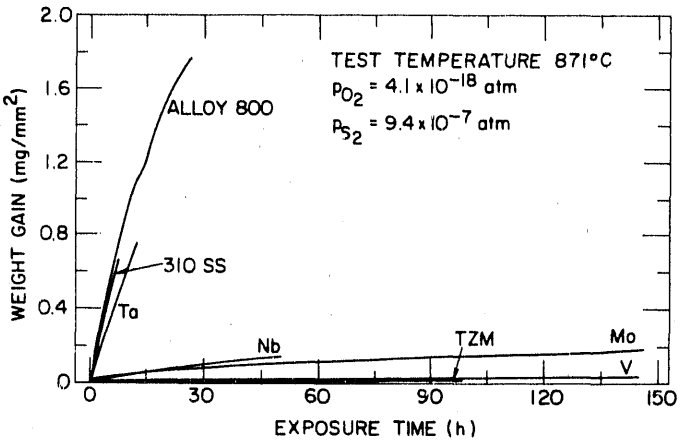

Fig. 7. Comparison of thermogravimetric test data for several refractory metals/alloys with those for conventional alloys exposed to oxygen/sulfur mixed-gas atmospheres

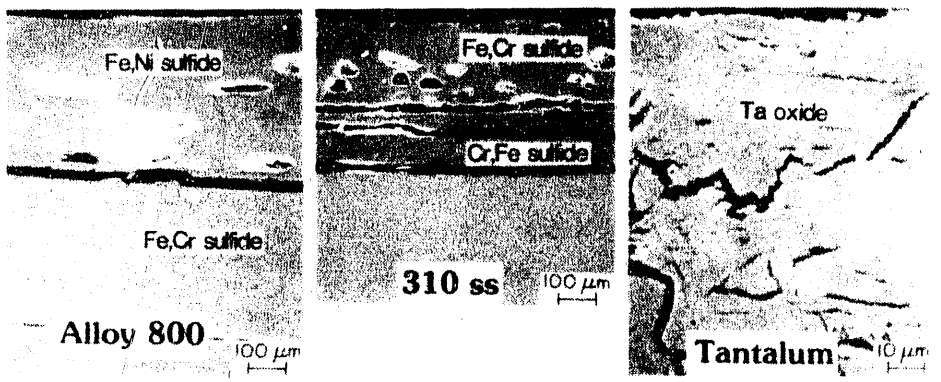

Fig. 8. Morphology of corrosion-product layers developed on Incoloy 800, Type 310 stainless steel, and tantalum specimens exposed to oxygen/sulfur mixed-gas atmospheres

Even though the refractory metals and alloys exhibit low corrosion rates when exposed to mixed-gas atmospheres, use of these materials as structural materials in fossil energy systems is not feasible in view of the difficulty in fabrication, inadequate mechanical properties, and cost. However, extensive studies were undertaken to evaluate the benefits of adding reactive, stable-oxide-forming elements such as Zr and Nb to model commercial alloys. The effectiveness of Zr and Nb as replacements for Cr was also investigated through the use of a series of Zr- and Nb-modified alloys containing only 12 wt.% Cr. Corrosion results obtained in air and low-oxygen environments and after exposure to oxygen/sulfur mixed gas atmospheres are presented in this report. In addition, tests were conducted to evaluate the beneficial effects, if any, of preformed oxide scales in retarding sulfidation. The influence of thermal cycling on the mechanical integrity of scale layers was also expored.

2 Experimental Procedure

Two series of model alloys containing Fe-12 wt.% Cr-8 to 12 wt.% Ni and Fe-25 wt.% Cr-20 wt.% Ni with nominal Zr and Nb contents of 0, 1, 3, and 6 wt.% were used in the investigation. Alloy compositions are given in Table 2. The alloys were produced from high-purity metal stock by melting in an environment that minimized oxidation of the melt and were cast in ingot form. The ingots were cold-rolled with intermediate annealing to

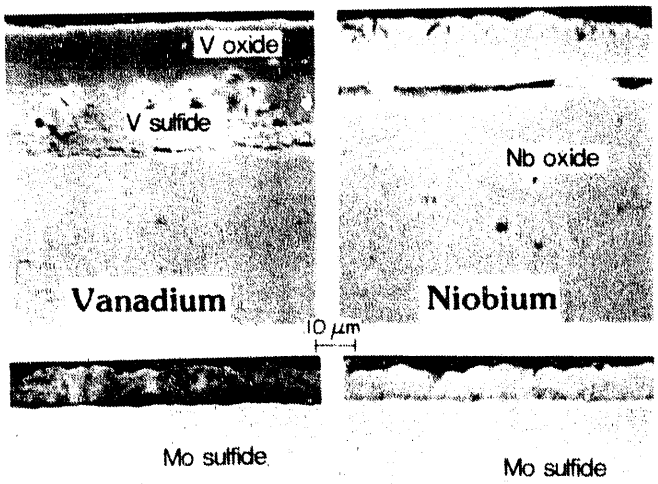

Fig. 9.
Morphology of corrosion-product layers developed on V, Nb, Mo, and TZM specimens exposed to oxygen/sulfur mixed-gas atmospheres

Table 1. Parabolic rate constants for reaction of several metals/alloys in oxygen/sulfur atmospheres at 871°C

Metal/Alloy	Rate Constant (g^2 cm^{-4} s^{-1})
Alloy 800	3.6×10^{-7}
310 SS	3.4×10^{-7}
Cr Sulfidation	5.0×10^{-7}
Ta	1.7×10^{-7}
Nb	1.2×10^{-9}
V	2.7×10^{-11}
Mo	7.0×10^{-10}
TZM	1.8×10^{-11}
Cr Oxidation in Air	2.1×10^{-12}

sheets of 1.25 mm thickness. The base alloys were annealed at 1050°C for 1 h to remove the effects of a final 50% cold reduction and to homogenize the structures. The Zr- and Nb-containing alloys were annealed at 1100°C for 7 h and 1050°C for 8 h, respectively. Because of the very low solubility of Zr and Nb in the alloys, intermetallic particles containing Zr or Nb with Fe and Ni were formed. These particles ranged in size from 4 to 8 μm, independent of the alloy Zr or Nb content, and had a spheroidized morphology. In the Zr-modified 12 wt.% Cr alloys, the intermetallic particles had the general composition of M_5Zr, where M was approximately $(Fe_{3.51}Ni_{1.07}Cr_{0.42})$. The particle composition in the

Table 2. Chemical compositions (in wt.%) of Fe-base alloys used in the present investigation

Nominal Composition	Ni	Cr	Zr	Nb	Mn	Si
Fe-12Cr-12Ni-0Zr	12.13	11.90	–	–	0.03	<0.1
1Zr	12.01	12.00	0.89	–	0.05	<0.1
3Zr	11.99	12.00	2.76	–	0.10	<0.1
6Zr	12.13	11.98	6.25	–	0.05	<0.1
Fe-25Cr-20Ni-0Zr	20.01	24.87	–	–	0.05	<0.1
1Zr	19.98	24.96	0.77	–	0.05	<0.1
3Zr	19.78	24.83	3.14	–	0.05	<0.1
6Zr	20.18	24.82	5.95	–	0.03	<0.01
Fe-12Cr-8Ni-0Nb	8.29	12.20	–	–	0.12	0.23
1Nb	8.10	12.50	–	1.13	0.16	0.21
3Nb	8.17	12.47	–	3.21	0.19	0.17
6Nb	8.17	12.83	–	6.67	0.21	0.25
Fe-25Cr-20Ni-0Nb	19.80	24.60	–	–	0.14	0.38
1Nb	19.90	25.30	–	0.93	0.17	0.23
3Nb	20.00	24.00	–	3.28	0.14	0.27
6Nb	20.60	25.00	–	6.75	0.15	0.42

Zr-modified 25 wt.% Cr was $Fe_{1.5}Ni_{3.5}Zr$. The particles in the Nb-containing alloys had compositions of $Fe_{2.39}Cr_{0.36}Ni_{0.19}Si_{0.06}$ in the 12 wt.% Cr alloys and $Fe_{1.64}Cr_{0.75}Ni_{0.55}Si_{0.06}$ in the 25 wt.% Cr alloys.

Alloy matrix compositions and grain sizes of the starting alloys are listed in Table 3. With the exception of the Si content in Nb-containing alloys, the compositions of the intermetallic particles, determined by energy-dispersive X-ray analyses in an electron microprobe, were found to vary little within each base alloy composition. In the Si-containing alloys, essentially all of the available Si was contained in the intermetallic particles. The fine distribution and stability of the particles during heat treatment resulted in grain refinement in the alloys, as shown in Table 3.

After heat treatment, the specimens (13 x 10 x 0.8 mm with a 1-mm-diameter drilled hole for suspension) were ground with 240-, 400-, and 600-grit SiC paper, cleaned, and dried before testing. The test facilities include a rig in which up to 32 specimens could be exposed simultaneously to flowing gas, and a thermobalance in which weight changes of a single specimen can be recorded continuously. Mixtures of the gases CO, CO_2, CH_4, H_2S, and H_2 produced a range of oxygen and sulfur partial pressures at test temperatures of 650, 875, and 1000°C. Table 4 lists the compositions of various mixed gases (used in various experiments) and the corresponding values for oxygen and sulfur partial pressures that were calculated by assuming thermodynamic equilibria between different gas species.

Table 3. Volume fractions of intermetallics, alloy matrix compositions, and grain sizes of several model alloys

Nominal Composition	Matrix Grain Size (μm)	Volume Fraction of Intermetallic (%)	Calculated Matrix Composition (wt %)[a]			Actual Composition (wt.%)		
			Cr	Ni	Fe	Cr	Ni	Fe
Fe-12Cr-12Ni-0Zr	50	–	–	–	–	11.9	12.1	74.7
1Zr	30	4	12.2	11.8	75.9	12.1	11.3	76.5
3Zr	15	11	12.9	11.4	76.3	13.6	10.4	76.0
6Zr	8	25	14.2	11.3	74.0	14.3	10.4	75.3
Fe-25Cr-20Ni-0Zr	50	–	–	–	–	24.9	20.0	54.1
1Zr	20	3	25.4	19.2	55.2	25.6	19.2	55.2
3Zr	12	13	28.0	14.7	57.6	26.2[b]	16.0	57.5
6Zr	6	24	33.3	8.7	58.0	31.2[b]	12.8	56.0
Fe-12Cr-8Ni-0Nb	80	–	–	–	–	12.2	8.3	79.1
1Nb	20	4	12.7	8.2	78.8	12.0	7.5	80.2
3Nb	12	11	13.0	8.6	78.1	12.5	7.7	79.8
6Nb	6	25	14.1	9.0	76.5	13.0	8.2	78.7
Fe-25Cr-20Ni-0Nb	80	–	–	–	–	24.6	19.8	55.1
1Nb	22	3	25.6	20.1	53.9	nd[c]	nd	nd
3Nb	12	13	24.9	20.7	49.7	nd	nd	nd
6Nb	6	24	27.3	22.4	49.7	nd	nd	nd

[a]Based on the assumption that all the Zr and Nb were present as intermetallic compounds of experimentally determined compositions.

[b]Matrix actually duplex; values given are net concentrations of elements in the matrices.

[c]nd = not determined.

Exposure environments were selected with the aid of oxygen/sulfur thermochemical diagrams (Figs. 10-12) based on published thermodynamic data.[23-25] The diagrams shown in Figs. 10-12 are actually the stability diagrams for Cr-S-O, Fe-S-O, Ni-S-O, Zr-S-O, and Nb-S-O, all superimposed on common log pS_2 and log pO_2 axes for each temperature. In the diagrams, solid lines represent equilibrium-phase boundaries for the pure metals and reaction products at unit activity. In general, spinel oxides and sulfides were ignored for simplicity in construction of these diagrams. In certain cases, comparisons of the behavior of the 12 wt.% Cr alloys modified with Zr or Nb with Fe-25 wt.% Cr-20 wt.% Ni alloy were made, because the latter is a commonly used base commercial alloy composition for use at high temperatures where a high level of corrosion resistance is required.

Table 4. Gas compositions and partial pressures of oxygen and sulfur in gas mixtures used in the present investigation

Gas Mix	Gas Composition (vol.%)					T (°C)	Reactant Activities (atm)	
	CO	CO_2	CH_4	H_2S	H_2		pO_2	pS_2
1	16.5	33.0	5.5	0.078	44.922	650	8.07×10^{-24}	3.61×10^{-11}
						875	2.15×10^{-18}	2.41×10^{-9}
						1000	4.87×10^{-16}	1.94×10^{-8}
2	1.8	3.6	0.6	0.015	93.985	650	4.18×10^{-25}	2.95×10^{-13}
						875	1.82×10^{-20}	2.04×10^{-11}
						1000	2.80×10^{-18}	1.41×10^{-10}
3	6.0	12.0	2.0	0.135	79.865	650	2.43×10^{-24}	4.40×10^{-11}
						875	2.10×10^{-19}	2.63×10^{-9}
						1000	3.78×10^{-17}	1.70×10^{-8}
4	1.8	3.6	0.6	0.171	93.829	650	4.19×10^{-25}	3.84×10^{-11}
						875	1.82×10^{-20}	2.90×10^{-9}
						1000	2.81×10^{-18}	1.83×10^{-8}
5	6.0	12.0	2.0	1.276	79.485	650	2.43×10^{-24}	4.24×10^{-9}
						875	2.07×10^{-19}	2.49×10^{-7}
						1000	3.76×10^{-17}	1.60×10^{-6}
6	16.5	33.0	5.5	0.711	44.289	650	8.08×10^{-24}	3.06×10^{-9}
						875	2.19×10^{-18}	2.38×10^{-7}
						1000	4.96×10^{-16}	1.65×10^{-6}
7	6.0	12.0	2.0	0.515	79.485	650	2.43×10^{-24}	6.46×10^{-10}
						875	2.11×10^{-19}	3.87×10^{-8}
						1000	3.81×10^{-17}	2.49×10^{-7}
8	16.5	33.0	5.5	0.284	44.716	650	8.07×10^{-24}	4.81×10^{-10}
						875	2.16×10^{-18}	3.71×10^{-8}
						1000	4.90×10^{-16}	2.59×10^{-7}
9	0.5	44.5	-	0.450	54.550	650	2.22×10^{-23}	1.72×10^{-9}
						875	1.26×10^{-17}	1.97×10^{-7}
						1000	2.86×10^{-15}	1.44×10^{-6}
10	0.5	44.5	-	0.205	54.795	650	2.22×10^{-23}	3.53×10^{-10}
						875	1.27×10^{-17}	3.88×10^{-8}
						1000	2.86×10^{-15}	2.96×10^{-7}

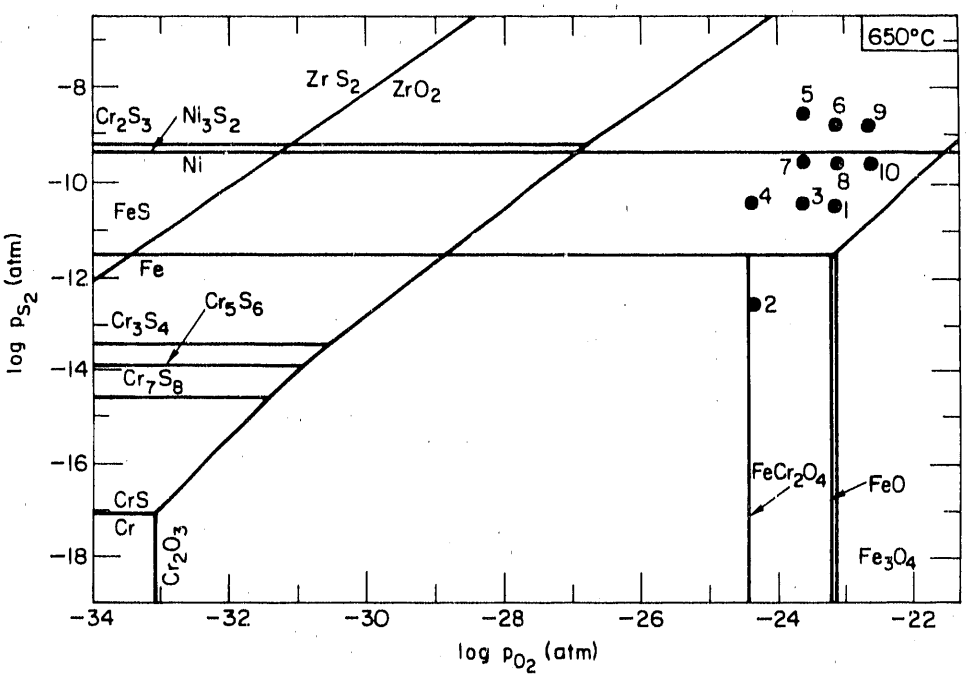

Fig. 10. Thermochemical stability diagram for Cr–S–O, Fe–S–O, Ni–S–O, Zr–S–O, and Nb–O systems at 650°C

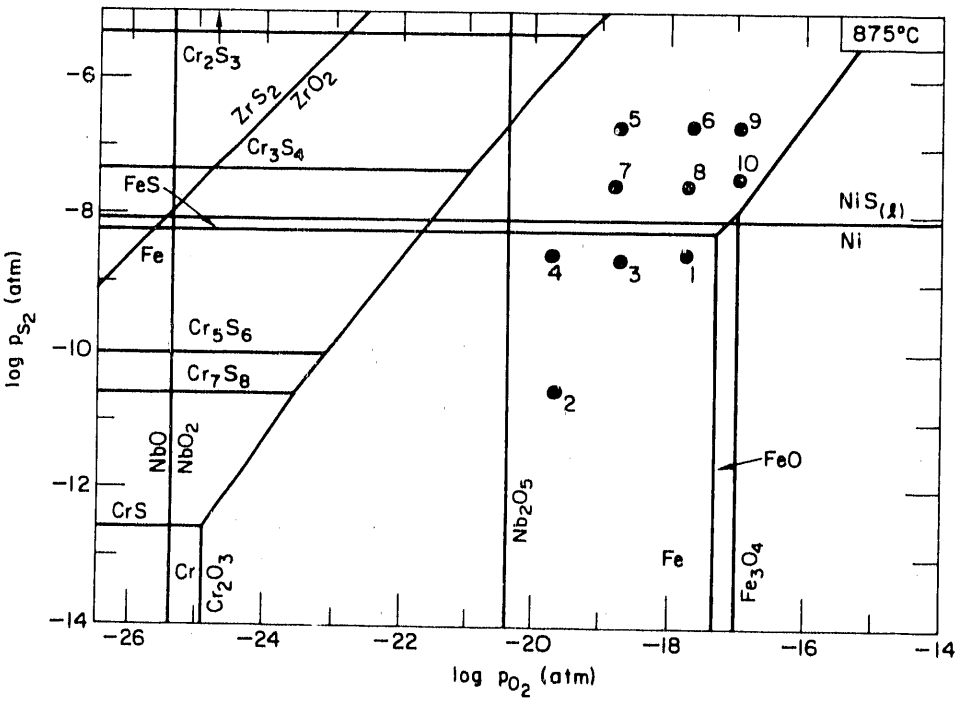

Fig. 11. Thermochemical stability diagram for Cr–S–O, Fe–S–O, Ni–S–O, Zr–S–O, and Nb–O systems at 875°C

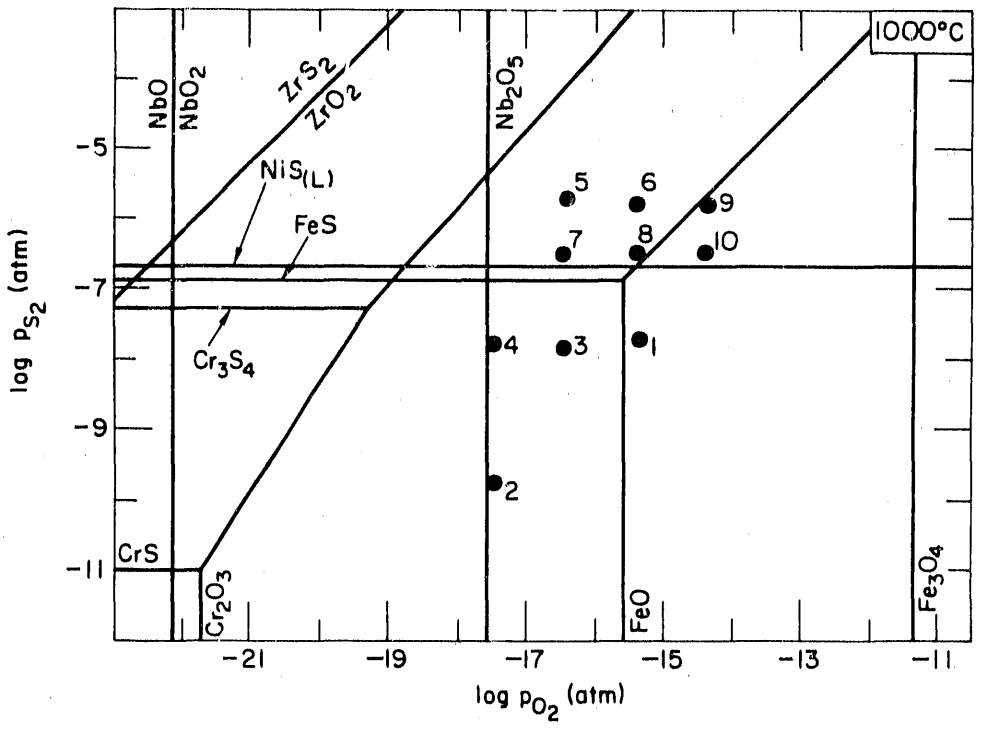

Fig. 12. Thermochemical stability diagram for Cr–S–O, Fe–S–O, Ni–S–O, Zr–S–O, and Nb–O systems at 1000°C

3 Results and Discussion

3.1 Fe-12 wt.% Cr-8 to 12 wt.% Ni-Zr/Nb Alloys

3.1.1 Oxidation in Air

Specimens of each alloy were oxidized in dry air for up to 120 h at 875°C. The continuously recorded weight changes obtained during oxidation are displayed in Fig. 13. The high rates of weight gain of the unmodified Fe-12 wt.% Cr-12 wt.% Ni alloys reflect formation of scales under parabolic breakaway conditions, i.e., scale growth with periods of parabolic behavior interrupted at frequent intervals with accelerated rates of scale formation due to loss of protection. The breakaway kinetics, however, are not resolvable with the scale of the axes used in Fig. 13. Examination of the oxidized, unmodified alloys revealed multilayer scales that were rich in Fe and that had poor adhesion to the substrate (see Fig. 14). The outer layers of such scales were composed of a mixed (Fe, Cr) oxide with a hexagonal structure [$(Fe,Cr)_2O_3$]. In regions where spalling had occurred, even under isothermal oxidation conditions, an Fe-rich oxide formed. Both the spinel oxide $FeCr_2O_4$ and Fe_3O_4 were detected.

For all alloys containing Zr or Nb, breakaway oxidation kinetics were not observed and the steady-state rate of scale growth could be described by the expression

$$w^n = kt \qquad (1)$$

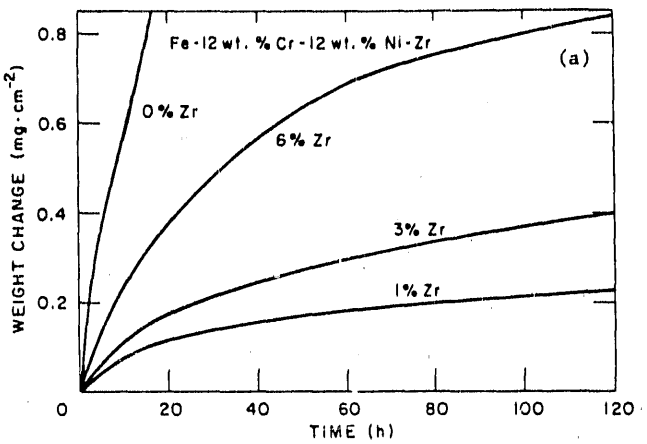

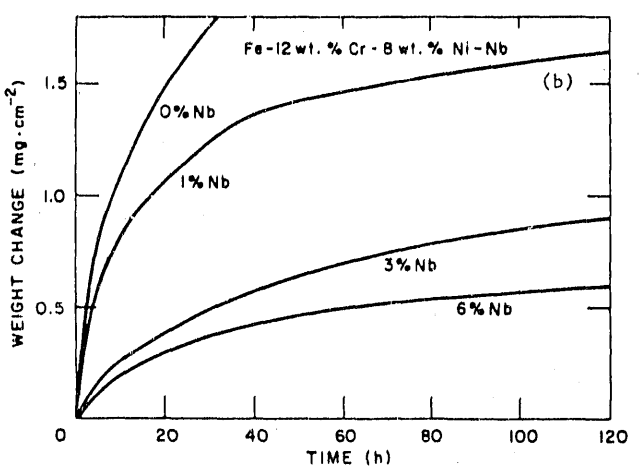

Fig. 13. Thermogravimetric data for (a) Zr-modified and (b) Nb-modified alloys exposed to air at 875°C

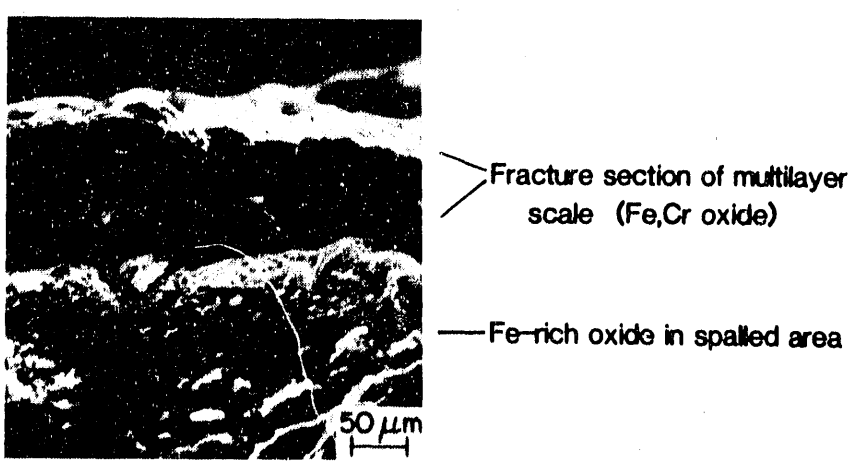

Fig. 14. SEM photograph of partially spalled oxide scale formed on Fe–12 wt.% Cr–8 wt.% Ni alloy in air at 875°C

where w is weight gain, k is a constant, t is time, and the rate exponent n is independent of Zr or Nb content in the alloy and falls in the range of 2 to 2.2. The values of the parabolic rate constant, k, are listed in Table 5; they increase with increasing Zr content, but decrease with increasing Nb content of the alloys. The time of transient oxidation decreased with an increase in Nb content, but is independent of Zr content. Transient oxidation is the period of scale growth before a continuous, rate-controlling, protective oxide layer is established, from which time the oxidation rate exponent, n, will be ≈2. For example, the transient period for the Zr-free alloy is 20 h, but decreases to <2 h for 1 and 3 wt.% Zr alloys.

The scales formed on the Nb-modified alloys were composed principally of Cr-rich $(Fe,Cr)_2O_3$. Evidence of accelerated scale growth was clearly apparent on the 1 wt.% Nb alloy (see Fig. 15a). The oxide blisters, which contain Fe-rich $(Fe,Cr)_2O_3$ and interrupt the continuity of the Cr-rich $(Fe,Cr)_2O_3$ oxide, are presumed to have formed in the transient stages of oxidation before parabolic growth kinetics were established. The size and extent of accelerated growth are associated with a transient period of oxidation of 45 h. Oxide blisters caused by localized accelerated scale growth were not found on the alloys containing 3 or 6 wt.% Nb (see Fig. 15b). The secondary electron image photograph in Fig 15b shows oxide crystals on the outer surface of the scale formed on the 3 wt.% Nb alloy. These oxide crystals were $(Fe,Cr)_2O_3$ under which almost pure Cr_2O_3 was detected in the cross section. The oxide $(Nb,Cr)O_2$ was also detected by X-ray diffraction, but its location was not determined. Scale on the 6 wt.% Nb alloy also contained the $(Nb,Cr)O_2$ phase, but in greater proportion to that detected in the scale on the 3 wt.% Nb alloy. The additional $(Nb,Cr)O_2$ phase in the scale on the 6 wt.% Nb alloy could conceivably contribute to the lowered rate of scale growth compared to that of the 3 wt.% Nb alloy. Alloy grain size and slight differences in Cr content could also contribute to the differing rates of oxidation. The oxidation rates of so-called Cr_2O_3-forming alloys can span wide ranges,[26] but, the different times of transient oxidation of the 3 and 6 wt.% Nb alloys may be explained by the

Table 5. Parabolic rate constants and duration of transient oxidation of the alloys upon exposure to air at 875°C

Alloy	Time of Transient Oxidation (h)	Parabolic Rate Constant ($g^2\ cm^{-4}\ s^{-1}$)
Fe–12Cr–12Ni–0Zr	–	–
1Zr	2	1.3×10^{-7}
3Zr	2	3.9×10^{-7}
6Zr	2	1.8×10^{-6}
Fe–12Cr–8Ni–0Nb	–	–
1Nb	45	3.6×10^{-6}
3Nb	8	2.4×10^{-6}
6Nb	4	1.9×10^{-6}

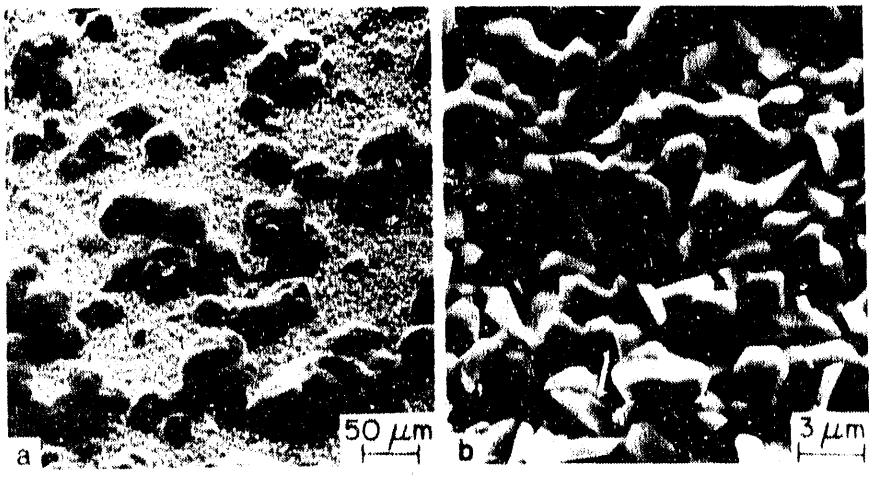

Fig. 15. SEM photographs of (a) nodule-containing scale on Fe-12 wt.% Cr-8 wt.% Ni-1 wt.% Nb and (b) crystals of (Fe,Cr) oxide in nodule-free scale on Fe-12 wt.% Cr-8 wt.% Ni-3 wt.% Nb after oxidation for 120 h in air at 875°C

grain size (12 and 6 μm, respectively).[27] The formation rates of scales on the Nb-modified alloys are similar to those quoted for Cr_2O_3-forming alloys.[26] Minimal internal oxidation of the Nb-modified alloys occurred.

Scales that formed on the Zr-modified alloys were composed principally of Cr_2O_3 with outer regions containing $FeCr_2O_4$. The duration of transient oxidation was short and independent of Zr content, and in no case were oxide blisters (which are associated with accelerated rates of oxidation) detected. Examination of outer surfaces of oxidized specimens revealed nodules of oxide (see Fig. 16), predominantly Cr_2O_3 with some $FeCr_2O_4$, whose population increased with increasing Zr content. In cross section, it was found that the oxide nodules formed at the former locations of intermetallic particles in the alloy surfaces. Oxidation of the Zr-containing intermetallic particles resulted in both nodule formation in the oxide scale and internal oxidation of the alloys to a depth of 30 μm (see Fig. 17). Zirconium was oxidized in the locations of intermetallic particles and appeared in discrete oxide colonies in the vicinity of the scale/metal interface. Zirconium was not found in the oxide scales. The increased rate of scale growth with increasing Zr content is attributed to a corresponding increase in the population of oxide nodules, and thus the increasing volume of oxide formed is proportional to the Zr content.

The rate of oxidation of the 1 wt.% Zr alloy was ≈5 times less than the lowest rate quoted for Cr_2O_3 formation in the absence of a reactive metal addition.[26] Any influence of Cr content and grain size on the oxidation behavior of Zr-modified alloys was clearly overshadowed by the presence of Zr. Grain size alone was shown to have little influence, by oxidation of a version of the Zr-free, Fe-12 wt.% Cr-12 wt.% Ni alloy that has a grain size of 30 μm, i.e., equivalent to that of the 1 wt.% Zr alloy. The oxidation behavior was very similar to that of the same alloy with a grain size of 50 μm. It is conceivable that once the internal oxidation of intermetallic particles occurs, the concentration of Cr in the alloy matrices will approach that of the bulk alloy composition, and thus the minor benefits

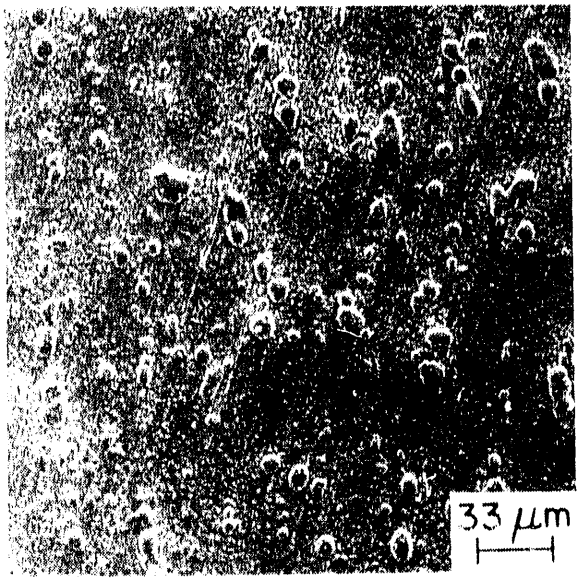

Fig. 16.
SEM photograph of outer surface of nodule-containing oxide scale formed on Fe–12 wt.% Cr–12 wt.% Ni–1 wt.% Zr alloy in air at 875°C

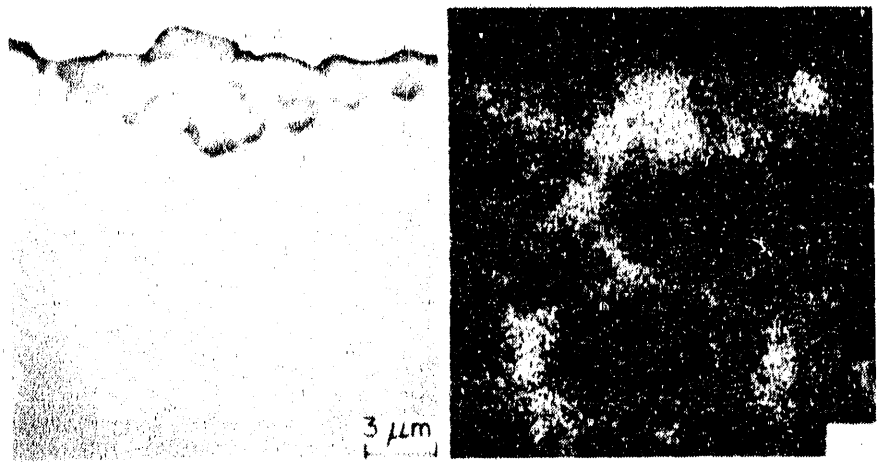

Fig. 17. Cross section of Fe–12 wt.% Cr–12 wt.% Ni–6 wt.% Zr with Zr map after exposure in air at 875°C

resulting from the initial increased Cr concentration in the alloy matrices will be lost. A secondary influence of the presence of internal oxide particles can be to trap vacancies present in the alloy or produced during oxidation, which might otherwise condense at the scale/metal interface and adversely affect scale/metal adhesion.[9]

The mechanisms by which Zr and Nb promote protective oxidation behavior of alloys containing only 12 wt.% Cr are not completely clear. In the case of Nb, an oxide containing Nb is present in the scale that is composed predominantly of the (Fe,Cr) sesquioxide. Because the steady-state rate of scale growth decreases as the volume fraction of the Nb-containing oxide increases, it is possible that the presence of Nb modifies the rate of transport of scale-forming species in the scale. Whether the rate change is caused by the blocking of grain boundary transport (the major path for diffusing species at temperatures below about 1050°C), changing of oxide grain size, or modification of grain boundary

structure cannot be determined from available information. In addition, while the discrete particles of (Nb,Cr) oxide were detected, Wagner-Hauffe-type doping cannot be discounted. Because of the variable valence of Nb, both accelerated and retarded rates of oxidation could be expected due to Nb doping of the principal (Fe,Cr) oxide, while Zr (Zr^{4+}) doping should increase the rate of oxidation if Cr ions migrate via vacancies on the Cr sublattice in Cr_2O_3. A change in the mechanism of scale formation from cationic to anionic transport, or at least to mixed cation and anion diffusion control, which has been shown for alloys containing reactive metal additions,[8,9] should not in itself promote formation of a protective oxide scale. Also, because neither Zr nor Nb form complete layers of oxide, which could provide protection, it is therefore necessary to consider the transient stages of oxidation in order to explain the protective behavior that is imparted by the quarternary additions.

The thermodynamic stability of oxides of Nb and Zr should inhibit formation of less stable oxides such as Fe mainly by competing for sites on the alloy surface, particularly if they are comparatively fast-growing. While oxide layers of ZrO_2 on Zr grow approximately four times as fast as Cr_2O_3 layers,[28] little is known of the rate at which stable nuclei of the respective alloying elements form. When reactive elements are present in an alloy, it has been proposed that they can enhance nucleation of Cr_2O_3 and thus promote formation of a continuous rate-controlling surface oxide scale.[4] There is also evidence for altering the oxide grain size due to refractory metal additions, which can exert a pronounced influence on the growth rate of the oxide.

3.1.2 Oxidation in Low Partial Pressure Oxygen

Specimens of all alloys were isothermally oxidized for 100 h in an oxygen partial pressure of 1.6×10^{-19} atm at 875°C. This environment should permit only the oxides of Zr, Nb, and Cr to form. Continuous weight-change recordings were not obtained, but the specimens were examined in detail after exposure. As with oxidation in air, the scaling behavior of all alloys was strongly influenced by Zr or Nb additions. The addition-free Fe-12 wt.% Cr-12 wt.% Ni and Fe-12 wt.% Cr-8 wt.% Ni alloys formed Cr-rich oxide scales 1-3 μm thick that contained ≈4 wt.% iron. Scale spallation was clearly evident, revealing voids in the vicinity of the scale/metal interface (see Fig. 18a). Globular metallic particles were present on the outer surface (see Fig. 18b) of the Fe-12 wt.% Cr-12 wt.% Ni specimen. Few metallic particles containing 85 wt.% Fe and 15 wt.% Ni were present in the 1 wt.% Zr alloy, and scales on the 3 and 6 wt.% Zr alloys were free from metallic particles. The Fe-12 wt.% Cr-8 wt.% Ni and all Nb-modified alloys were also free from metallic particles; this may be attributable to the presence of Si oxide at the scale/metal interfaces. The scales on all Zr- and Nb-modified alloys were predominantly Cr_2O_3, but under the low pO_2 conditions it is evident that at least 1 wt.% Nb or Zr is required to ensure formation of a complete, protective layer of the oxide. The consequences of incomplete coverage with Cr_2O_3 became clear when alloys were exposed to an environment containing sulfur after preoxidation. Incomplete coverage by the protective oxide resulted in the immediate onset of accelerated scale growth via sulfidation, the details of which will be discussed in Section 3.1.3 below.

3.1.3 Behavior in Mixed-Gas Environments

A number of gas mixtures (listed in Table 4) were used to examine the corrosion behavior of the alloys over a range of oxygen and sulfur partial pressures that generally fell within the bounds of the conditions expected in coal-gasification systems (e.g., pS_2 of 10^{-5} to 10^{-9} atm and pO_2 of 10^{-16} to 10^{-18} atm at 875°C). The threshold boundary, which

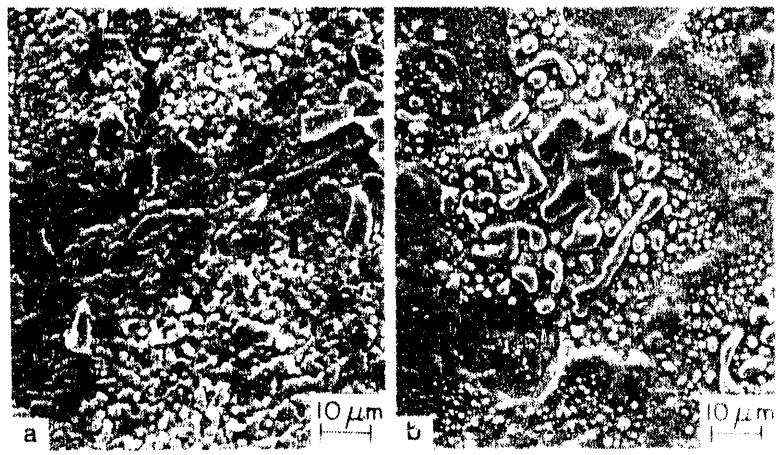

Fig. 18. SEM photographs of outer surfaces of scales formed on (a) Fe–12 wt.% Cr–8 wt.% Ni and (b) Fe–12 wt.% Cr–12 wt.% Ni in sulfur-free, low-pO_2 atmosphere at 875°C

separates regimes of protective oxidation behavior and breakaway sulfidation, in terms of pO_2, is $\approx 10^3$ times higher than the pressures that define the thermodynamic equilibrium boundary between Cr_2O_3 and Cr sulfide at sulfur partial pressures below the Fe-FeS equilibrium level. At sulfur partial pressures higher than the Fe-FeS equilibrium level, a threshold boundary was not established; a major factor contributing to the positioning of the threshold boundary for all 12 wt.% Cr alloys was that in all test atmospheres in which FeS was stable, accelerated corrosive attack occurred. As will be seen, however, the presence of Zr or Nb reduced the severity of attack under sulfidation conditions.

The behavior of the alloys can be described with reference to the two modes of attack observed in the oxygen/sulfur mixed-gas atmospheres (see Table 4) used in the present investigation.

Protective Scaling Behavior

Protective oxidation behavior was exhibited by all 12 wt.% Cr alloys upon exposure to gas mixtures 1, 2, and 3. In gas mixtures 1 and 3, the scales contained $(Fe,Cr)_2O_3$ and the spinel oxide $FeCr_2O_4$; additionally, $(Nb,Cr)O_2$ was present in scales formed on Nb-containing alloys. The spinel oxide was not detected upon exposure to gas mixture 2. The lower limit of thermodynamic stability of $FeCr_2O_4$, at an oxygen partial pressure of 1.3×10^{-19} atm at 875°C, should preclude its formation in gas mixture 2. Despite the formation and maintenance of protective oxide scales in gas mixtures 1, 2, and 3, intergranular Cr, Zr, or Nb sulfides formed internally in the alloy substrates. In each case, small (<2 μm) discrete particles were located to a depth of 10-25 μm. Increasing the Zr or Nb content within the alloy reduces the depth of sulfide formation. Reference to the thermochemical stability diagram in Fig. 11 confirms that the sulfur partial pressures in gas mixtures 1, 2, and 3 may permit sulfide formation under conditions similar to those expected beneath the Cr oxide/substrate interface. While such sulfidation attack does not appear to enhance surface scale breakdown, the presence of intergranular sulfide can degrade the mechanical properties of alloys.[29]

Unlike the results in the sulfur-free, low pO_2 atmosphere, islands of globular metallic particles containing Fe and Ni did not form on the Fe-12 wt.% Cr-12 wt.% Ni or Fe-12 wt.% Cr-6 wt.% Ni-1 wt.% Zr alloys upon exposure to gas mixtures 1, 2, or 3. In addition to the low level of sulfur, the stability of $FeCr_2O_4$ in gas mixtures 1 and 3 would permit the incorporation of available Fe in the scale into the spinel oxide, while the oxygen partial pressure in gas mixture 2 was below the limit of thermodynamic stability of $FeCr_2O_4$. The growth of continuous surface oxide scales on the Fe-12 wt.% Cr-12 wt.% Ni and Fe-12 wt.% Cr-12 wt.% Ni-1 wt.% Zr alloys in gas mixture 2, therefore, is attributed to the presence of sulfur. The manner in which sulfur influences oxide nucleation, the transient stages of scale growth, and the defect structure and transport properties of oxide scales so as to promote protective oxidation behavior cannot be determined from available data.

Sulfidation Behavior

At a pS_2 *below* the Fe-FeS thermodynamic equilibrium established by gas mixture 4, (Fe,Cr) sulfide scales formed at thicknesses (40-50 μm) that were independent of alloy Zr or Nb content. Continuous monitoring of the weight change of one alloy (Fe-12 wt.% Cr-12 wt.% Ni-6 wt.% Zr) indicated that parabolic scaling kinetics were obeyed with a rate constant of 2×10^{-10} g^2 cm^{-4} s^{-1}. This value compares with $\approx 2 \times 10^{-12}$ g^2 cm^{-4} s^{-1} for the rate of oxidation of the same alloy (see Table 5). Intergranular internal sulfide formation increased in depth from 100 to 160 μm with decreasing Zr or Nb content from 6 to 0 wt.%. The maximum Fe content of (Fe,Cr) sulfides was on the order of 30 wt.% and was contained in Fe-rich and Fe-depleted lamellae. The lamellae of differing compositions probably formed from a uniform (Fe,Cr) sulfide solid solution during cooling.

Despite the presence of a substantial amount of Fe in the sulfide scale, nodules of metallic material were formed on the outer surfaces of some scales (see Fig. 19). This material, containing 85 wt.% Fe and 15 wt.% Ni, was of similar composition to the globular metallic material formed on the outer surfaces of oxide scales on the Fe-12 wt.% Cr-12 wt.% Ni and Fe-12 wt.% Cr-12 wt.% Ni-1 wt.% Zr alloys upon exposure to the sulfur-free, low-pO_2 environment. The presence of the void at the interface of the sulfide and metallic nodule in Fig. 19 suggests that dissociation of the sulfide scale may have contributed to the formation of the metallic material in a manner similar to that described previously,[30] while rapid transport through the thin sulfide scale beneath the nodule should have ensured a steady supply of Fe and Ni to the surface of the void. Enhanced localized internal sulfidation of Cr adjacent to the region where nodules are formed (Fig. 19) should also increase the concentration of both Fe and Ni in the scale.

At a pS_2 in *excess* of the Fe-FeS thermodynamic equilibrium, the rate of alloy degradation was very high. In gas mixtures 6, 7, and 9, specimens 0.8 mm in thickness were consumed due to sulfide formation within 100 h of exposure at 875°C. Porous scales composed of Fe-rich sulfide outer layers with (Fe,Cr) sulfide inner layers were accompanied by completely sulfidized alloy matrices. Nickel also participated in the formation of the scales, as evidenced by the partially molten sulfide scales at 875°C. Nickel was a minor constituent of the Fe-rich sulfide outer layer of scale, but was contained in Ni-rich metallic material located as a film on grain boundaries in the Fe-rich sulfide. It has previously been proposed that in alloys containing Fe and Ni, an $(Fe,Ni)_9S_8$ phase with a solidus temperature of ≈857°C may form and permits rapid transport of material.[31] Cooling the mixed sulfide to room temperature causes rejection of a solid solution of Fe and Ni, leaving an iron-rich

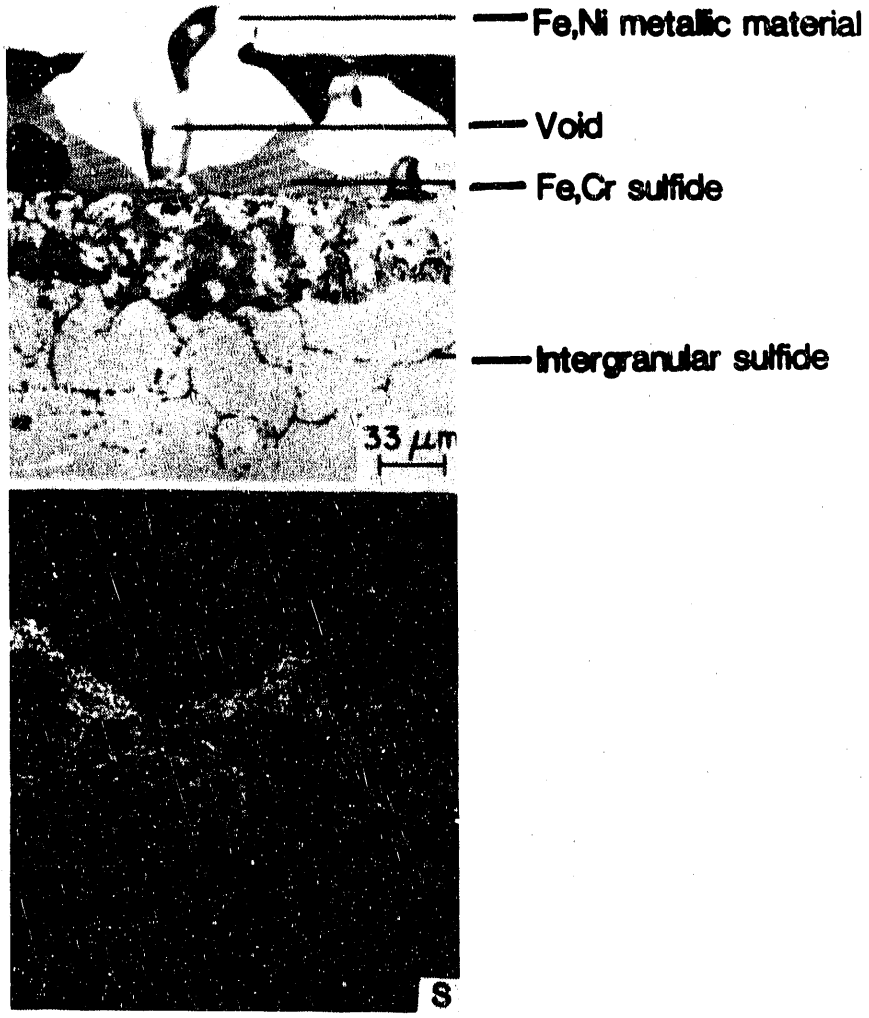

Fig. 19. Cross section of Fe–12 wt.% Cr–8 wt.% Ni with sulfur map after exposure to gas mixture 4 for 100 h at 875°C

sulfide.[32] The presence of Ni sulfide with a melting temperature of 645°C was not observed despite the thermodynamic stability of NiS.

In gas mixture 8, sulfidation attack occurred in all alloys, with the severity of attack decreasing with increasing Zr or Nb content (see Fig. 20). The scale compositions were similar to those of scales formed in gas mixtures 6, 7, and 9, described above, but the incomplete consumption of the alloy substrates enabled evaluation of the mode of internal attack. A region containing the front of internal attack of the Fe-12 wt.% Cr-12 wt.% Ni-6 wt.% Zr alloy is shown in Fig. 21. The region adjacent to the scale/metal interface (region A) in Fig. 21 contains randomly distributed Cr oxide and Zr oxide particles in a matrix of mixed (Fe,Cr) sulfides (light bands with Fe:Cr = 5:1 and dark bands with Fe:Cr = 2.5:1) and numerous voids. Deeper into the substrate (region B), essentially the same (Fe,Cr) sulfides coexist with Zr sulfide, islands of (Fe,Ni) metallic material (55 wt.% Fe, 45 wt.% Ni), and some voids. Still deeper into the substrate (region C) is the region of greatest sulfur penetration where the intermetallics, alloy matrix, and sulfur contribute to the formation of a

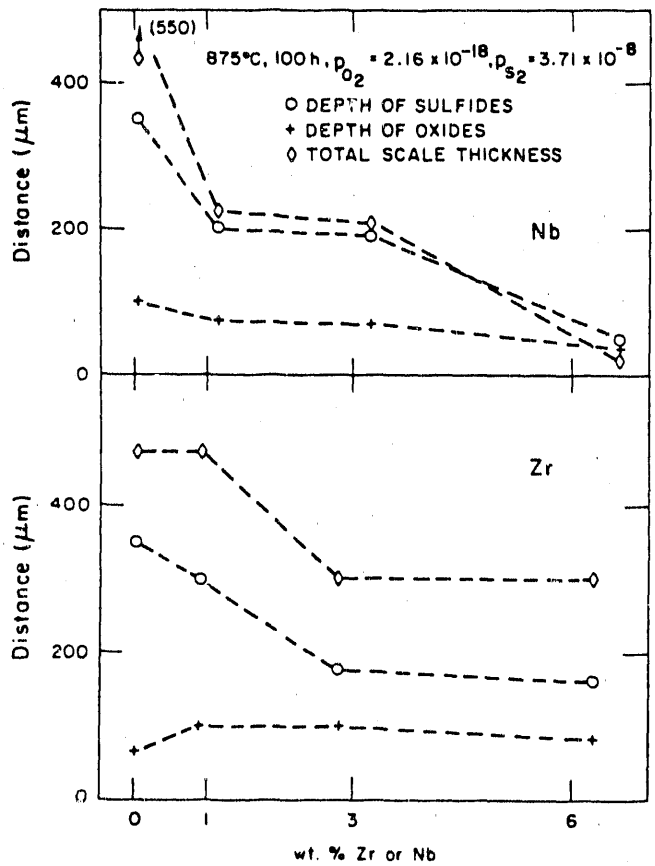

Fig. 20.
Scale thickness and depth of internal attack as a function of alloy Zr/Nb content after exposure to gas mixture 6 for 100 h at 875°C

Cr-depleted solid solution containing Fe, Ni, Zr, and S. In the 1 and 3 wt.% Zr or Nb alloys, the solid solution of Fe, Ni, Zr/Nb, and S formed interconnecting veins of material, whereas in the 6 wt.% Zr/Nb alloys, a continuous zone of the material 20-30 μm thick was observed.

From the various products of internal attack, the following reaction model is proposed:

1. Internal oxidation of Zr occurs rapidly in a region close to the scale/metal interface in the initial stages of exposure.

2. Sulfur penetration results in the formation of sulfides rich in iron in Cr-depleted regions close to the substrate surface.

3. Deeper penetration of sulfur beyond the depth of Zr oxide particles results in direct interaction between sulfur and the Zr-containing intermetallics.

4. Sulfur combines with intermetallics and the alloy matrix to form a solid solution that is depleted in Cr.

5. Chromium is incorporated into the Fe-rich sulfide to form (Fe,Cr) sulfide.

6. From the solid solution, almost pure Zr sulfide, additional Fe-rich sulfide, and islands of metallic (Fe,Ni) material are formed.

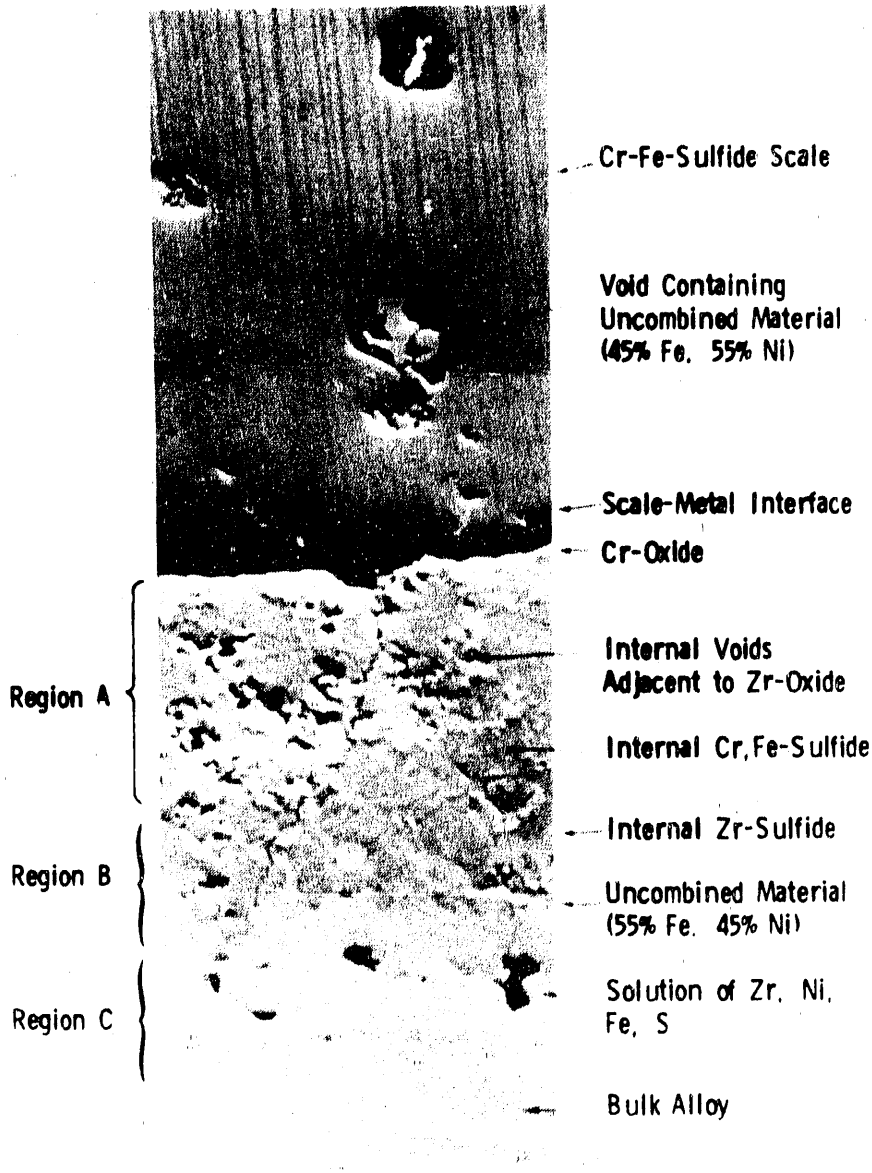

Fig. 21. Cross section of Fe–12 wt.% Cr–12 wt.% Ni–6 wt.% Zr exposed to gas mixture 6 for 100 h at 875°C

7. Continued sulfur penetration results in gradual sulfidation of the (Fe,Ni) metallic material.

8. Additional ingress of oxygen results in oxidation of the Zr sulfides, forming new Zr oxide and releasing sulfur that then penetrates deeper into the substrate. Void formation in the subscale region may be associated with many of the dissociation reactions occurring with the progress of internal attack.

At the same pS_2 as in gas mixture 8, but at the higher pO_2 established in gas mixture 10, the corrosion behavior of all alloys was borderline between protective oxide formation and rapid sulfidation. In some regions on specimen surfaces, sulfide formed in the early stages of exposure, whereas in other regions protective oxide formed. Exposures of up to 5000 h in gas mixture 10 with intermittent visual inspection of the specimens showed that in most cases, the zones of surface sulfide did not spread laterally with time (see Fig. 22). Long-term exposure resulted in the accumulation of Zr oxide or Nb oxide at the scale/metal interface (see Fig. 23). The presence of the stable oxide, in particulate form in the case of Zr oxide, or as a continuous layer in the case of Nb oxide, could be responsible for improved resistance to corrosion by providing an additional blocking layer to the transport of active corrosion-product-forming species.

3.2 Fe-25 wt.% Cr-20 wt.% Ni-Zr/Nb Alloys

3.2.1 Oxidation in Air

All alloys containing 25 wt.% Cr exhibited protective oxidation behavior, as shown in Fig. 24, according to thermogravimetric analysis (TGA) data. Cr_2O_3 was the principal constituent of scales formed on all 25 wt.% Cr alloys. Similar parabolic rate constants of $\approx 3.8 \times 10^{-13}$ g^2 cm^{-4} s^{-1} were determined for alloys containing 0, 1, and 3 wt.% Nb, whereas the parabolic rate constant of the 6 wt.% Nb alloy was 5.8×10^{-13} g^2 cm^{-4} s^{-1}. The value for the rate constant at 871°C for the 0, 1, and 3 wt.% Zr alloys was $\approx 2.1 \times 10^{-13}$ g^2 cm^{-4} s^{-1} while that for the 6% Zr alloy was 8.5×10^{-13} g^2 cm^{-4} s^{-1}.

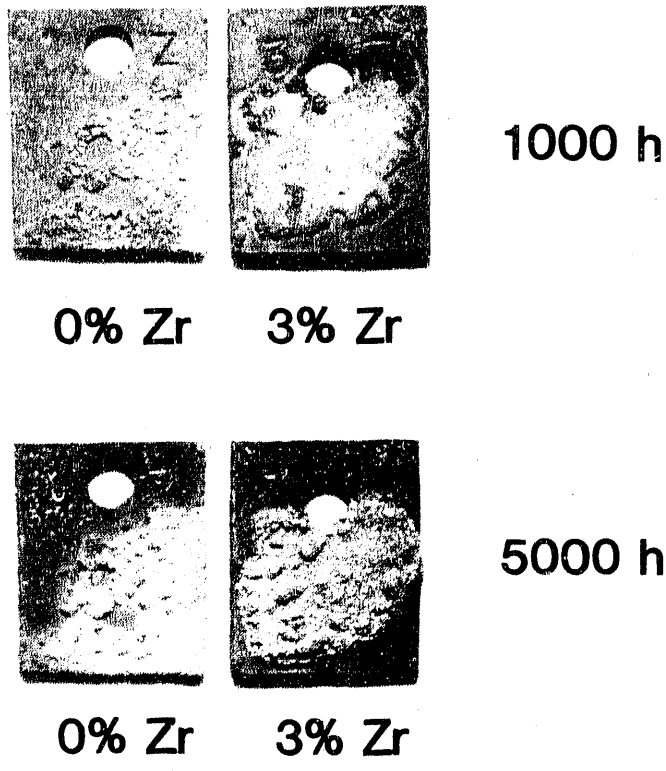

Fig. 22. Macrographs of specimens of Fe–12 wt.% Cr–12 wt.% Ni–O and 3 wt.% Zr exposed to gas mixture 8 for (a) 1000 and (b) 5000 h at 875°C

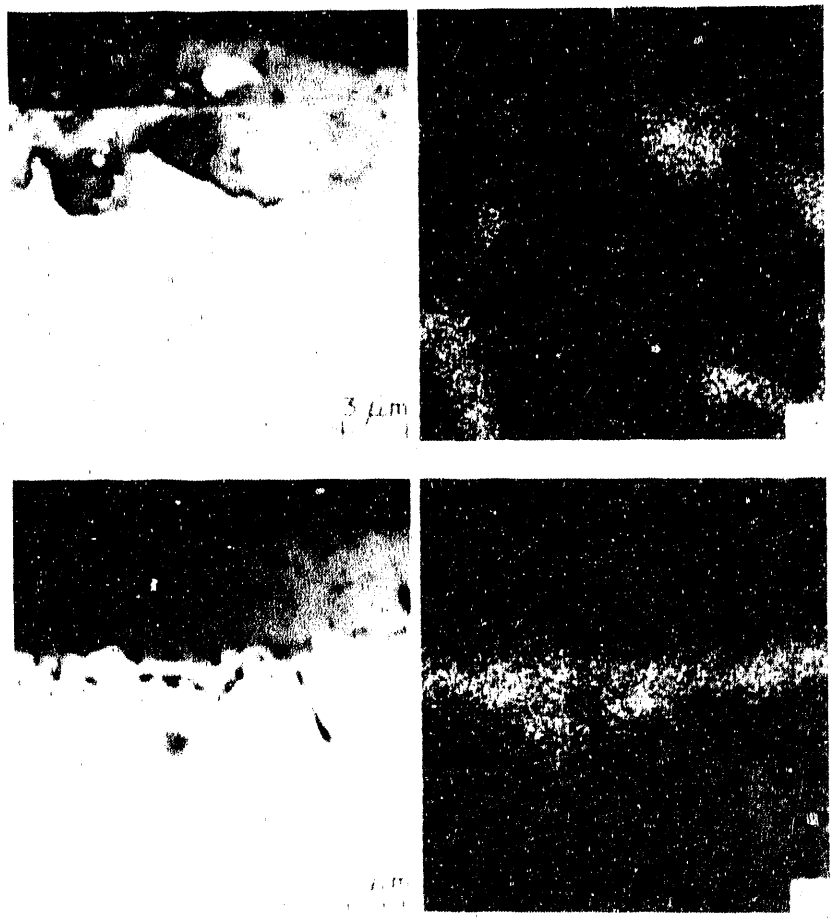

Fig. 23. Cross sections of (a) Fe–12 wt.% Cr–12 wt.% Ni–3 wt.% Zr with Zr map, and (b) Fe–12 wt.% Cr–8 wt.% Ni–3 wt.% Nb with Nb map, both after exposure to gas mixture 8 for 1000 h at 875°C

Examination of oxidized specimens revealed that the Zr-free alloy had a 4-μm-thick scale and the Zr-containing alloys exhibited nodules (5–8 μm thick) interrupting the continuity of the otherwise uniform, thin (1 μm) surface layer Nodule scale growth is associated with the oxidation of Zr-containing intermetallics at the surface of the metal substrate. No Zr oxide was detected in the thin surface layers between the nodules on any of the alloys. Negligible void formation at the scale/metal interface occurred on the Zr-containing alloys, in contrast to the Zr-free alloys, where large voids formed. Internal oxidation occured in alloys via oxidation of intermetallic particles. The depth to which intermetallics are oxidized increases with increasing Zr content in the alloy, ranging from 15 to 40 μm. Absence of zirconium in the Cr oxide scale, coupled with deep internal oxidation of the element, suggests low Zr mobility in the alloy. The greater volume of surface oxide due to nodule formation on Zr-containing alloys, combined with the proportional relationship between Zr content and the volume of internal oxides, undoubtedly accounts for the differences in weight gain observed for alloys containing different

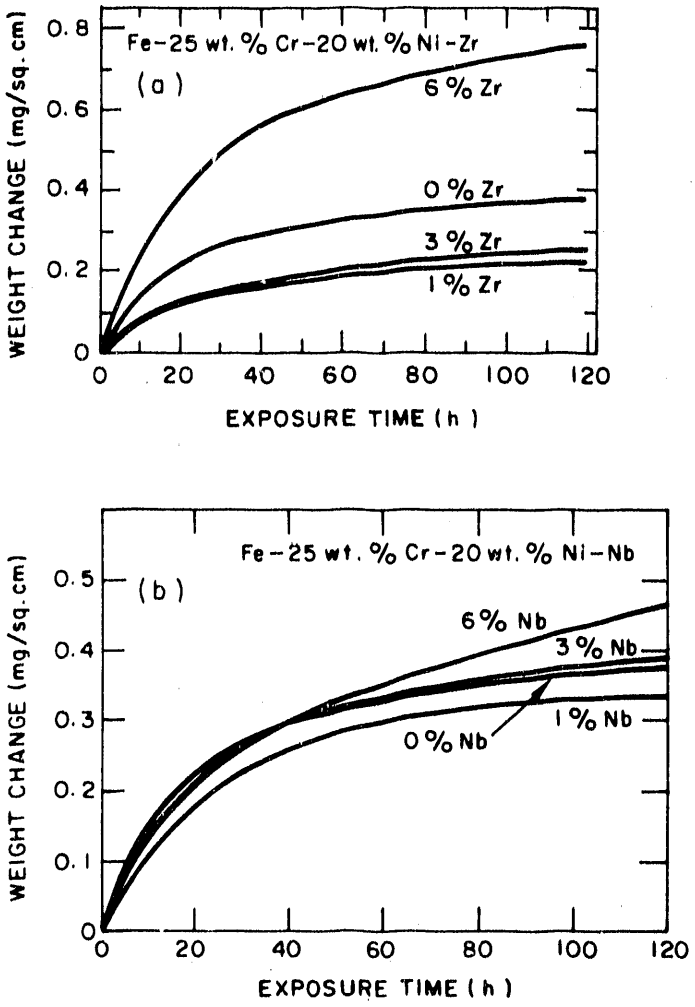

Fig. 24.
Thermogravimetric test data for Zr- and Nb-modified alloys containing 25 wt.% Cr exposed in air

concentrations of zirconium. While zirconium appears to accelerate the oxidation rate of the 25 wt.% Cr alloys during the initial period of exposure at 871°C in air, the rate of steady-state scale growth differs little for alloys of different Zr content.

In the case of Nb-containing alloys, the amount of a mixed (Nb,Cr) oxide increased with alloy Nb content. Examination of the scales in cross section revealed the location of the Nb-containing oxide to coincide closely with the locations of intermetallic particles at the surfaces of the alloys. Energy-dispersive X-ray analysis showed that the (Nb,Cr) oxide contained a low level of Si.

Scale adhesion to the alloy is improved by the addition of either Zr or Nb. The condensation of vacancies at the scale/metal interface is demonstrated by the presence of interfacial voids on the Zr/Nb-free alloys; few such interfacial voids occur on alloys containing Zr or Nb. Maintenance of contact between the scale and the alloy should allow more even load transfer and reduce the possibility of scale buckling. While it may be assumed that vacancies condense internally in these alloys, the possibility that scale growth is controlled by anionic diffusion cannot be discounted. Enhanced surface roughening due to the oxidation of intermetallics could conceivably contribute to improved mechanical keying of the scale to the alloy.

3.2.2 Oxidation at Low Oxygen Partial Pressure

Specimens of all alloys were isothermally oxidized at a pO_2 of 1.6×10^{-19} atm at 875°C for 100 h. Continuous weight-change recordings were not obtained, but the specimens were examined in detail after exposure. All 25% Cr alloys formed scales composed of thin (1–2 μm) continuous oxide layers. In the case of Zr/Nb modified alloys, the scale was interrupted by thicker (≈5 μm) nodular growths associated with the oxidation of intermetallics. The composition of both the scale and the nodules was found to be almost pure Cr oxide. Based on thermodynamic stability data, essentially only Zr, Nb, and Cr in the alloy should oxidize in the low-pO_2 atmosphere, and the Fe and Ni can play an active role only in solution in the surface scale. From the similarity of scaling behavior exhibited in the low-pO_2 and air environments, it appears that a Cr content of 25 wt.% is adequate in supporting selective oxidation, and the Fe and Ni exert little influence on scaling kinetics during at least the first 100 h of exposure of the 25 wt.% Cr alloys. Internal oxidation at low pO_2 is slightly less severe than in air for the same time and temperature of exposure.

Doping of the metal-deficient Cr oxide by Zr ions (Zr^{4+}) can result in an increase in the vacancy concentration of the oxide and produce a greater rate of oxidation. However, conventional analytical techniques such as scanning electron microscopy, electron microprobe, and Auger electron spectroscopy, failed to detect substitutional Zr in the Cr oxide. Another possible factor is the ability of a reactive element such as Zr and Nb to enhance nucleation of Cr oxide especially in the early stages of exposure. Of all possible oxides, those of Zr and Nb are more stable than Cr_2O_3 and form at rates about four times greater than that for Cr_2O_3. However, the low mobility and low concentration of Zr and Nb in the alloys prevent them from forming a continuous surface layer; it is feasible that oxide particles on the metal surface could enhance heterogeneous nucleation of Cr oxide. Because the oxidation behavior of Zr/Nb modified alloys cannot be fully explained on the basis of thermodynamic data and microstructural analysis, it was apparent that a study of the initial stages of oxidation of these alloys was necessary. With the use of a reaction cell capable of being heated to more than 500°C in gaseous environments of the desired pO_2, the initial stages of oxide formation on Fe–25 wt.% Cr–20 wt.% Ni alloys with and without Zr were studied in-situ in a high-voltage electron microscope (HVEM).

Specimens for transmission electron microscopy were prepared by grinding the annealed alloy sheet samples to a thickness of 300 μm, punching out 3-mm-diameter disks, and electrochemically polishing away material from the centers of the disks with a 4:1 solution of CH_3OH and H_2SO_4 to produce adequately large electron-thin areas for subsequent examination. While the central regions of Zr-free alloy disks were relatively uniform in thickness, slight preferential removal of material from the intermetallic particles caused some unevenness in the thickness of disks of the Zr-modified alloy. In the present study, a mixture of 99 vol.% CO_2–CO was passed through the reaction cell at a maximum pressure of 1.3×10^{-2} atm. At this pressure, a temperature of 500°C could be obtained. Heating to 500°C in a period of ≈30 s and cooling to <100°C in less than 15 s could be achieved. An accelerating voltage of 600 kV was used throughout the work. Thin-foil specimens were first examined so that features such as grain boundaries, twins, dislocation structures, and inclusions, as well as the phases present, could be located in the Zr-modified alloys. Oxidation in the CO_2–CO gas mixture was carried out for periods of up

to 1800 s. In general, exposure times of less than 240 s were adequate to allow complete coverage of the metal surface with oxide, while progressively longer exposure times enabled oxide grain growth and changes in the chemical composition of the oxide films.

Electropolishing of the Zr-free alloy resulted in slight preferential attack of alloy grain boundaries but more significantly in the formation of slight undulations on the surfaces of grains, giving a rumpled appearance on a very fine scale. Upon exposure at 500°C, relatively even coverage of the surface of alloy grains by oxide particles was observed after less than 60 s of oxidation. The time for the first detectable oxide particles to appear was similar on all grains, i.e., preferential oxide nucleation/growth on certain grain orientations was not observed. The growth of oxide gave a typical equiaxed structure to the film when viewed perpendicularly to the metal foil (Fig. 25) and a progressive increase in oxide grain size with time (Fig. 26). The oxide grain sizes displayed in Fig. 26 represent the range of sizes measured at numerous points on several specimens after the same exposure time. In the early stages of oxidation, differences were observed in the sizes of oxide grains formed on grains of different orientation in the substrate. Oxide growth was enhanced on alloy grain boundaries, which became lighter, while the growth of oxide on the alloy grains caused darkening. Voids gradually accumulated at the grain boundaries even after 300 s of oxidation at 500°C (Fig. 27a) and coalesced to produce larger voids at the alloy grain boundaries after longer times (Fig. 27b). Over long periods of exposure of coupon-size specimens of the Zr-free alloy, voids formed at the scale/metal interface, with the largest voids located at the grain boundaries on the substrate surface. Grain growth of the oxide continued at a parabolic rate over the first 1800 s of oxidation with a rate constant of 1.1×10^{-12} cm^2 s^{-1}.

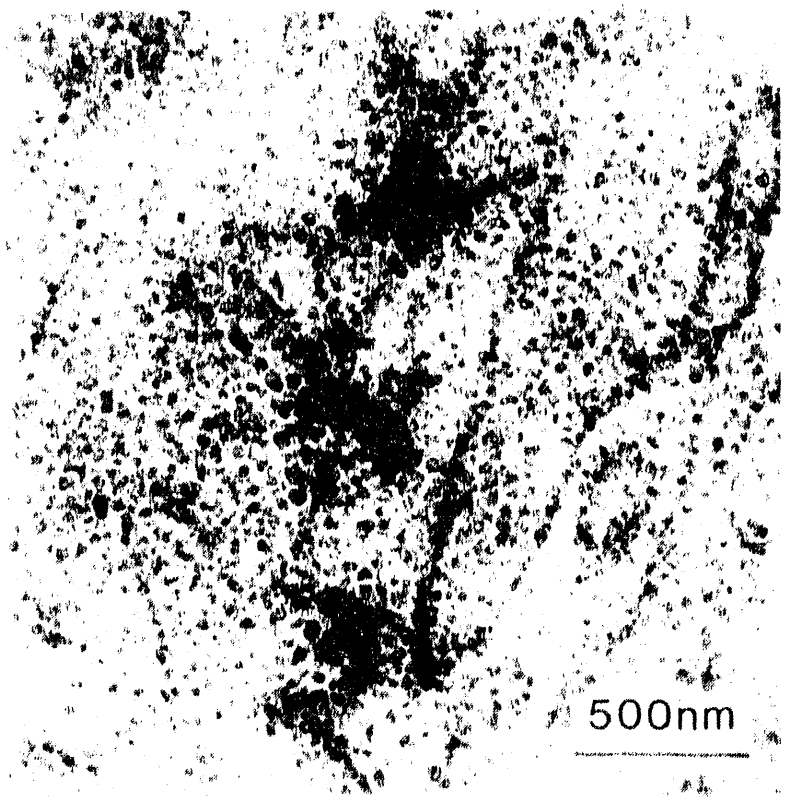

Fig. 25.
Surface oxide formed on Zr-free alloy during oxidation at 500°C for 240 s

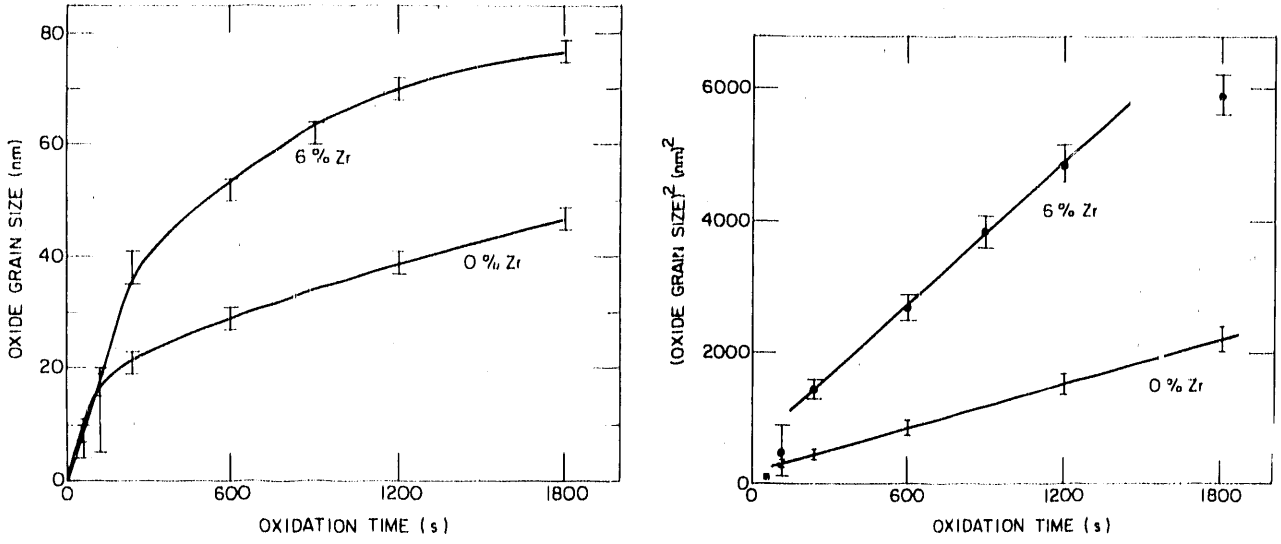

Fig. 26. Variation of oxide grain size with time and rate of oxide grain growth for oxidation at 500°C

The chemical compositions of oxide films as a function of time during the first 1800 s of exposure at 500°C are summarized in Table 6. Analysis of the scale was achieved with electron diffraction patterns. Using an accelerating voltage of 600 kV and a camera length of 2 m, lattice d-spacings in the range of 110 to 480 pm (110–480 x 10^{-12} m) could be measured with the HVEM system. Normally, up to 15 rings were produced in each diffraction pattern of about 50 mm in diameter. A combination of the similarity of some of the oxide phases and the squeezing of diffraction data onto a small piece of film resulted in frequent overlap of individual rings. Thus, rather than taking calculated lattice constants alone as definitive proof of the existence of phases, the number of rings present from the eight strongest lines of diffraction listed in the powder diffraction file and the shapes of the oxide crystals were used as additional evidence for phase identification. Lattice constants for standards of the oxides of interest are listed in Table 7.

From the data in Table 6, it is apparent that the predominant phase in the layer formed on the Zr-free alloy over the first 1800 s of exposure is cubic, although there is some evidence for the occurrence of hexagonal and tetragonal phases during oxidation. The cubic phase was deduced to be Fe_3O_4. Lattice constants for the tetragonal phase suggest that it was, in fact, almost cubic. While pure $FeCr_2O_4$ has lattice constants of a = 849.7 and c = 811.5 pm, the spinel oxide can exist over a wide range of Fe and Cr contents with extremes of $FeCr_2O_4$ and Fe_3O_4, so that the general formula $FeFe_{2-x}Cr_xO_4$, where $0 < x < 2$, is probably more appropriate. Because the tetragonal phase has almost equal lattice constants for a and c, it is believed that the value of x in the general formula must be close to zero, i.e., the spinel oxide has a very low Cr content.

Lattice parameters of the hexagonal phase suggest an oxide of a composition similar to Cr_2O_3 or Fe_2O_3. However, while essentially pure Cr_2O_3 was not detected in scales formed on coupon-size specimens oxidized at 600°C, and while Fe_2O_3 is not thermodynamically stable in the CO_2–CO gas mixture, the two oxides are mutually soluble in each other. Because Cr_2O_3 is a minor constituent oxide in scales formed at lower temperatures due

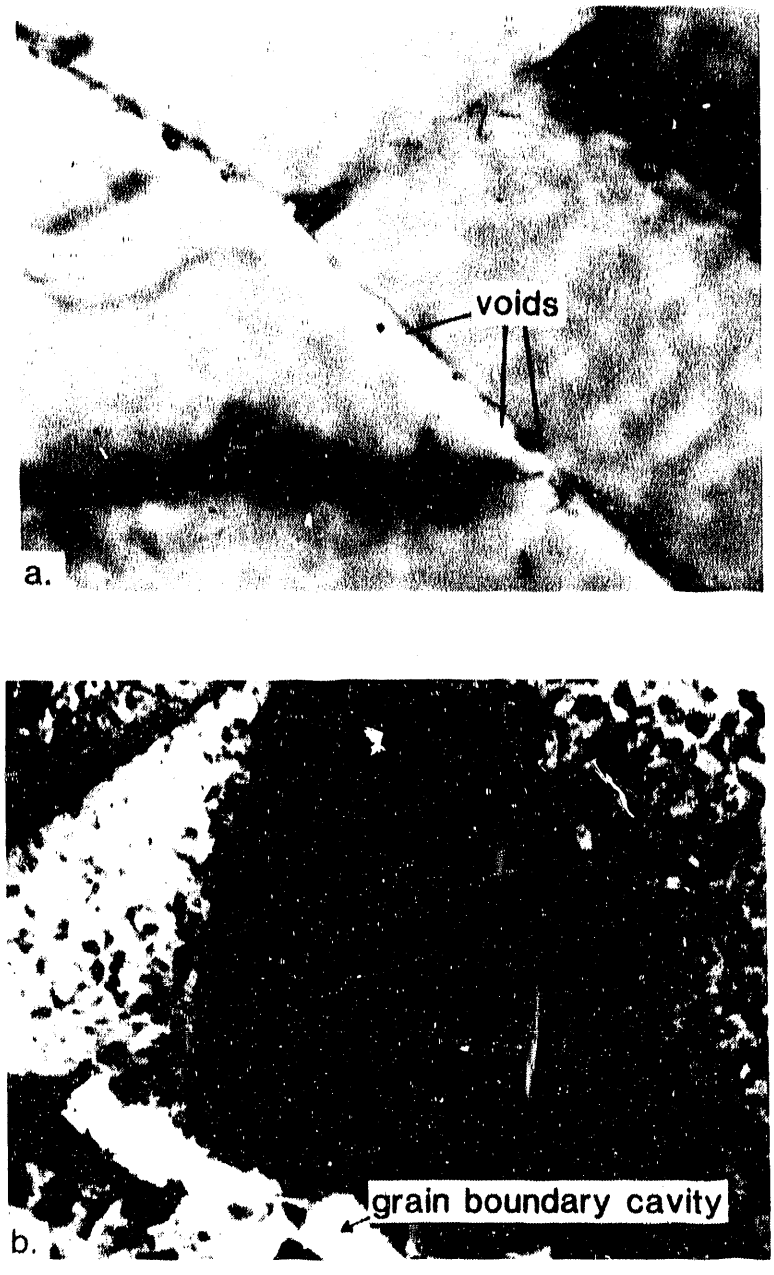

Fig. 27.
Micrographs showing (a) small voids at alloy boundaries after oxidation for 300 s and (b) cavities at alloy grain boundaries on the Zr-free alloy after 1200 s at 500°C

predominantly to kinetic reasons, it is probable that the participation of Cr in the oxidation reaction leads to stability of an oxide with a hexagonal structure based on Cr_2O_3 and containing Fe. Selected-area diffraction also revealed random orientation of grains in the oxide film, given by complete rings of uniform density of illumination. Complete diffraction rings were observed after oxidation times of ≈60 s at 500°C (less than 60 s at 600°C), while oxidation for times exceeding about 600 s produced progressively more spotty rings, presumably due to the increased oxide grain size.

Table 6. Data for the composition of oxides as a function of oxidation time

Oxide	Structure	Lattice Constants a (pm)	b (pm)	c (pm)	β
Cr_2O_3	Hexagonal	495.4	–	1358.4	–
Fe_2O_3	Hexagonal	503.6	–	1374.9	–
$(Fe,Cr)_2O_3$	Hexagonal	a	–	a	–
$FeCr_2O_4$	Tetragonal	849.7	–	811.5	–
Fe_3O_4	Cubic	839.6	–	–	–
FeO	Cubic	430.7	–	–	–
Fe_2O_3	Cubic	939.3	–	–	–
ZrO_2	Monoclinic	514.8	520.3	531.6	99° 23'

[a]Constants between those of Cr_2O_3 and Fe_2O_3.

Table 7. Reference lattice-parameter constants of various oxides that can form on Fe–Cr–Ni–Zr alloys

Time of Oxidation at 500°C (s)	Number of Strongest Diffraction Lines of Standard Observed (of 8)			Lattice Parameters of Component Oxides (pm)						Inferred Components of Oxide Film
					Hex.		Tet.			
	Cubic	Hex.	Tet.	Cubic	a	c	a	c	Other	
0% Zr										
60	7	2	3	827.2	–	–	–	–	–	cubic
120	7	3	3	822.5	–	–	–	–	–	cubic
240	7	3	4	830.6	–	–	827.6	–	–	cubic (+ tet.)
600	7	4	4	828.9	499.5[a]	1366.0[a]	832.2[a]	–	–	cubic (+ hex. + tet.)
1800	8	5	5	834.1	500.1	1370.6	828.8	–	–	cubic + hex. + tet.
6% Zr, matrix										
60	6	5	3	846.2	497.6[a]	1381.0[a]	–	–	–	cubic + hex.
120	6	5	3	842.5	496.6	1371.2	–	–	–	cubic + hex.
240	6	5	5	841.7	492.7	1385.3[a]	852.5	820.1	–	cubic + hex. + tet.
900	6	7	5	855.4[a]	495.7	1358.2	859.2[a]	801.5[a]	–	cubic + hex. + tet.
1800	6	7	5	850.7[a]	494.1	1362.9	856.1	822.5	–	cubic + hex. + tet.
6% Zr, intermet.										
60	7	3	3	842.8	–	–	–	–	ZrO_2[b]	cubic + ZrO_2
120	7	3	3	845.4	–	–	–	–	–	–
240	7	3	2	820.7[a]	–	–	–	–	–	–
900	5	3	2	836.9	–	–	–	–	–	–

[a]Uncertainty greater than 5 pm.
[b]Monoclinic phase.

Electropolishing of the Zr-modified alloy resulted in preferential removal of material from Zr-containing intermetallic particles, but unlike the unmodified alloy, polishing did not produce undulations on the surface of the matrix grains. Exposure to the oxidizing environment resulted in the formation of small, uniformly distributed colonies of oxide grains over the surface of matrix grains of the alloy (Fig. 28). The structure of the oxide in the dispersed colonies was predominantly cubic. Each colony consisted of numerous oxide grains covering a range of sizes up to 10 nm after 60 s of oxidation at 500°C, with the

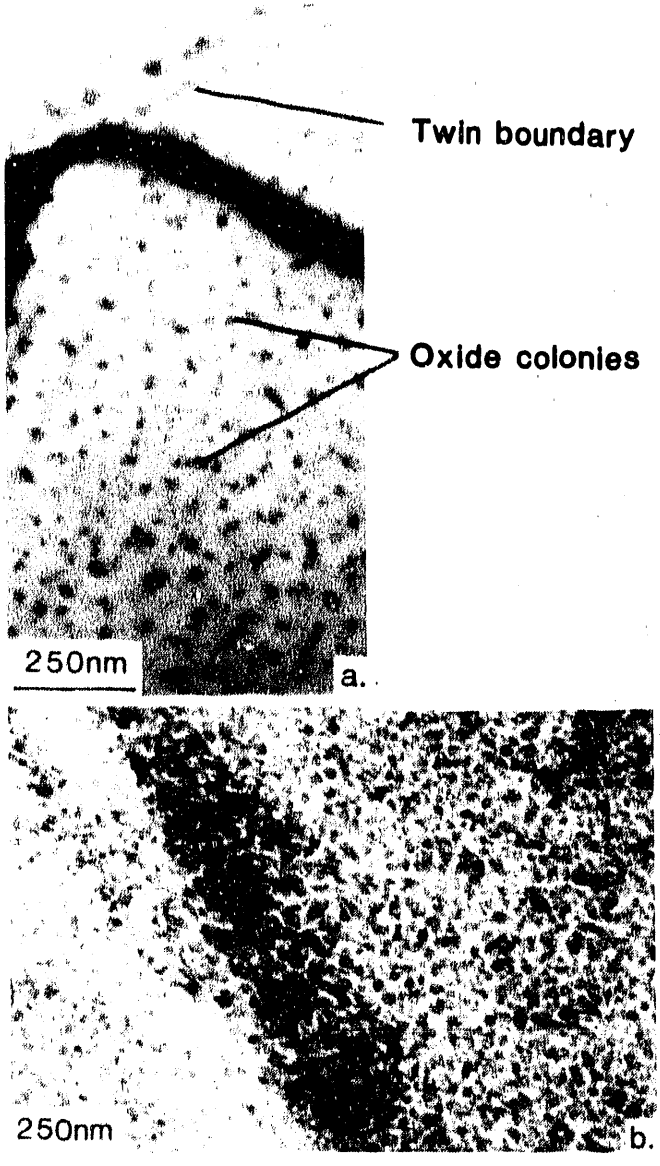

Fig. 28.
Micrographs showing (a) colonies of oxide formed during first 60 s of oxidation and (b) uniform coverage of oxide on Zr-modified alloy after 240 s at 500°C

largest grains located in the centers and progressively smaller grains at increasing distances from the centers. Also apparent in Fig. 28a, is the greater number of oxide colonies on the twin boundary than on the faces of the austenite grain. Similar enhanced nucleation of oxide was also observed at the grain boundaries. Lateral expansion due to both new grain formation and grain growth with increased time of oxidation resulted in impingement of the colonies and a uniform grain size (Fig. 28b).

Over the first 1800 s of exposure, the rate of oxide grain growth on the Zr-modified alloy was consistently greater than that on the unmodified alloy. However, while the rate of growth on the Zr-free alloy was parabolic after the initial stage of exposure (<100 s), a substantial deviation from uniform parabolic kinetics for oxide grain growth was observed for the Zr-modified alloy. The low rate of growth during approximately the first 150 s can be attributed to the formation of many new oxide grains, rather than merely to growth of the first-formed oxide grains, as the colonies expanded laterally. Between about 150 and

240 s, a comparatively high rate of grain growth occurred, apparently mainly in regions where the smallest grains were present, i.e., between the sites of the initial oxide colonies. Afterwards, a steady regime ensued with a rate constant of 3.6×10^{-14} cm^2 s^{-1} before evidence of a further break in kinetics was observed after more than 1200 s of exposure. Longer oxidation times resulted in total consumption of the metal locally, with the appearance of islands of oxide through the section of the metal foils.

The structure and composition of oxide films formed on matrix grains of the Zr-modified alloy were also monitored by electron diffraction. The data in Table 6 indicate that the predominant phase in the very early stages of oxidation was cubic and was deduced to be Fe_3O_4. Both the hexagonal and tetragonal phases were detected at an earlier stage of oxidation on the Zr-modified alloy than on the Zr-free alloy. The lattice constants of the hexagonal phase were generally lower for the Zr-free alloy at equivalent times of oxidation, indicating a comparatively higher Cr content, assuming the general oxide composition to be $(Fe,Cr)_2O_3$. Lattice parameters of the tetragonal phase suggest a composition closer to $FeCr_2O_4$ compared with the tetragonal phase on the Zr-free alloy. Selected-area diffraction also indicated random orientation of oxide grains. After 60 s of oxidation at 500°C, small oxide colonies formed on the matrix grains, and total coverage of the intermetallic particles with an uniform layer of very small (<5 nm) oxide grains occured. The oxide films formed on intermetallic particles were mainly composed of a cubic phase (Fe_3O_4) with little evidence for the development of either hexagonal or tetragonal phases. Two strong diffraction rings corresponding to the two strongest diffraction peaks for the monoclinic ZrO_2 phase were detected. From the study of the initial stages of oxidation of austenitic Fe-Cr-Ni-Zr alloys in low-pO_2 environments, three major points have arisen.

First, it has long been considered that reactive-metal additions may exert a beneficial influence on oxidation behavior by enhancing the oxide nucleation process, thereby reducing the time required for a complete, protective surface oxide layer to form. In the current work, it was observed that a complete oxide film forms more rapidly on the Zr-free alloy than on the Zr-modified alloy. While nucleation of oxide on the Zr-free alloy appeared to occur everywhere simultaneously, and a complete oxide film formed within 60 s of exposure, colonies of oxide with a separation of ≈ 0.1 μm were established at the same time on the Zr-modified alloy, and it took about 120 s of exposure for the colonies to expand enough laterally to impinge upon one another to form a complete oxide film. From this evidence, it would appear that the presence of Zr does not promote nucleation, despite smaller alloy grain size of the starting material. However, once the colonies are established, their growth is rapid, and the appearance of a hexagonal oxide phase (containing Cr) takes less time on the alloy containing Zr. Second, it was observed that the addition of Zr influences the grain size of surface oxide films.

Over the duration of tests undertaken in the HVEM study, the rate of oxide grain growth was consistently higher on the Zr-modified alloy, although the rate of grain growth progressively decreased with increasing time of exposure. Third, it has commonly been observed that such factors as small alloy grain size and the presence of reactive elements reduce the duration of transient oxidation and promote rapid formation of a protective oxide scale. Long-term tests have shown that the duration of transient oxidation of Fe-Cr-Ni alloys is reduced by the addition of Zr and after 100 h of exposure in low-oxygen partial pressure environment, scales on 0 and 6 wt.% Zr alloys contained 0.75 and 0.14 wt.% Fe (depicting transient oxide component), respectively.[6] Thus, the ability of Zr to promote the

growth of a hexagonal phase containing Cr, over the cubic phase Fe_3O_4, during the very early stages of oxide growth may contribute to lower Fe content of the steady-state scale. This could have important consequences on overall scale stability, especially in mixed oxygen-sulfur environments to be discussed in the next section of this report.

3.2.3 Behavior in Mixed-Gas Environments

A number of gas mixtures were used to establish the corrosion behavior of alloys over the range of oxygen and sulfur partial pressures generally expected in coal-gasification systems. Partial pressures resulting from each of the gas mixtures are listed in Table 4. There are essentially two aspects to the subject of stability of Cr oxide scales on alloys used in aggressive environments at high temperatures. Both thermodynamic and kinetic considerations determine whether a protective surface scale can form.

The threshold boundary separating the regime of protective oxide scale formation, to the right, from the regime of rapid sulfidation, to the left, for both the base and modified alloys is shown in Fig. 29. From the positions of the threshold boundaries for the respective alloys, it is inferred that the capacity to form a protective oxide scale is dependent upon alloy composition. In order of increasing capacity to provide protection are the Type 310 stainless steel, the pure ternary alloy, and the alloys containing additions of Zr or Nb. Progressively larger additions of the refractory elements appeared to impart proportionately greater corrosion resistance. It will become apparent from test results, however, that the threshold boundaries do not run approximately parallel to the Cr_2O_3/"CrS" thermodynamic equilibrium line over the whole range of pS_2 used in the investigation. At a pS_2 above about 10^{-7} atm, it appears that a greater excess concentration of oxygen is required to inhibit sulfidation than at a pS_2 below about 10^{-7} atm. The reason for this behavior will be discussed later in this section. The scaling characteristics of the range of alloys will begin with details of the behavior of the unmodified pure ternary and commercial Type 310 stainless steel, to which reference will be made in the discussion of the behavior of the modified alloys.

Behavior of Unmodified Alloys

In gas mixtures 6 and 7, rapid scale formation occurred from the beginning of exposure and continued at an almost linear rate to the end of the 100-h tests. At the high pS_2 of gas mix 6, 0.8-mm-thick specimens of Type 310 stainless steel were completely sulfidized within the 100-h test period because sulfide scales rich in Fe and Ni and internal sulfides rich in Fe and Cr were formed. In gas mix 7, thick (300-μm) sulfide scales formed, and internal attack of the alloy reached a depth of 100 μm. In the one other environment where the sulfidation reaction played a major role in the corrosion process (in gas mix 4), a relatively thin (90-μm) Cr-rich sulfide scale formed on top of a thin incomplete, Cr-rich oxide layer with particulate morphology. Continuous weight-change measurements in gas mix 4 indicated that the rate of scale formation was approximately parabolic, with a rate constant of about 10^{-10} g^2 cm^{-4} s^{-1}. The rate of scale formation on the model alloys in gas mix 4 was almost independent of Zr or Nb content and about a factor of 10 lower (10^{-11} g^2 cm^{-4} s^{-1}) than that for Type 310 stainless steel.

From a comparison of the behavior of Type 310 stainless steel with the pure ternary alloy in gas mix 4, it is apparent that Si and/or Mn contribute to the observed differences in scaling rate. Whereas Si is a stable oxide former in the environment of gas mix 4, Mn forms

a stable sulfide (see Fig. 29). Under oxidizing conditions, it has been shown that the interplay between respective contributions of Si and Mn is quite complex.[33] Silicon is rarely present in a sufficiently large concentration in an alloy to permit formation of a continuous Si oxide layer at the surface, but it strongly enhances intergranular attack of the alloy[34] and can adversely influence scale adhesion.[35,36] The presence of carbon in Type 310 stainless steel would tie up a small amount of Cr in the alloy grain boundary regions; this would have a negligible influence on scaling kinetics.

For the range of alloys under investigation, internal attack could be characterized by the presence of small, discrete, intergranular particles of Cr-, Zr-, or Nb-rich sulfide at the front of penetration beyond a region of intergranular and intragranular sulfides and oxides near the metal surface. Whereas intergranular Cr-rich oxide formed a depth of 50 μm in the pure ternary alloy in gas mix 4, intergranular oxides rich in Si formed to a depth of 150 μm in Type 310 stainless steel. While preferential formation of Si internally might be expected to free more Cr for formation of a surface scale, the depth to which sulfide particles were able to form was greater in the alloy containing Si. A consequence of the enhanced sulfur penetration may be a reduction in mechanical performance.[29] Thus, it is possible that both Si and Mn can enhance the severity of attack of austenitic stainless steels in gaseous environments containing oxygen and sulfur.

In gas mix 3, small particles of Cr-rich sulfide formed on the surfaces of Cr-rich oxide scales (3–6 μm thick) on Type 310 stainless steel and pure ternary alloys. Internal intergranular penetration of sulfur resulted in the formation of a number of very small (<1 μm) Cr-rich sulfide particles to depths of 35 and 60 μm, respectively, in the two alloys. In gas

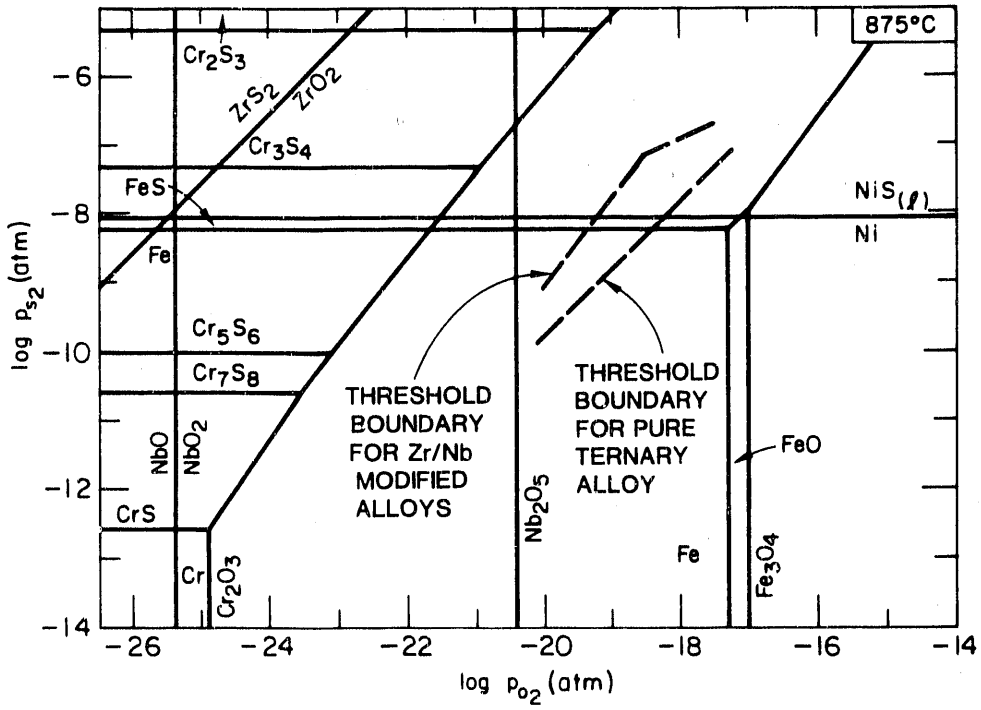

Fig. 29. Thermochemical diagram for Fe–25 wt.% Cr–20 wt.% Ni system at 875°C, showing threshold boundaries for base and modified alloys

mixtures 1 and 2, the scaling behavior of all alloys was closely similar. Adherent oxide scales (2–4 μm thick) containing a negligible amount of sulfur were deduced from X-ray diffraction data to be Cr_2O_3.

To this point in the discussion, except for the relatively minor influences of Si and Mn, the behavior of Type 310 stainless steel and the pure ternary alloys in gas mixtures 1–4, 6, and 7 has been shown to be similar. However, in the environments with moderately high pS_2, where oxidation is the predominant reaction but sulfides of Fe and Ni are stable (gas mixtures 8 and 10), the scaling characteristics of the two alloys differ significantly.

In gas mix 8, whereas the pure ternary alloy formed a protective scale, Type 310 stainless steel exhibited breakaway scaling kinetics. A 5–μm–thick scale of Cr oxide containing a small amount of sulfur formed on Type 310 stainless steel with sulfide particles (2–4 μm in diameter) on the outer surface (see Fig. 30). Blisters of sulfide containing mainly Fe and Cr with some Mn formed at widely scattered locations on the outer scale surface as a result of breakaway corrosion (see Fig. 31). Growth of large surface blisters was accompanied by formation of sulfides internally in the alloy. The time required for breakaway kinetics differed from specimen to specimen up to a maximum of approximately 100 h. The specific sites of breakaway corrosion could not be related to particular features of the oxide scale or of the alloy substrate.

At the same pS_2, but at a higher pO_2 (gas mix 10), random breakaway behavior of Type 310 stainless steel was sometimes observed in the early stages of exposure. In cases where breakaway occurred, continued exposure for longer times (up to 5000 h) resulted in lateral spreading of the affected regions so that eventually the whole surface of a specimen would be covered by a thick sulfide scale, accompanied by internal attack of the alloy. In cases where breakaway corrosion failed to occur, the oxide scale remained intact and protective up to the longest duration of the test. In gas mix 10, the pure ternary alloy formed a Cr oxide scale that remained protective over 5000 h of exposure at 875°C. Because the principal difference between the two unmodified alloys is the presence of Si and Mn, one or both of these elements may again be considered responsible for differences in corrosion behavior in the regime of gas mixtures 8 and 10.

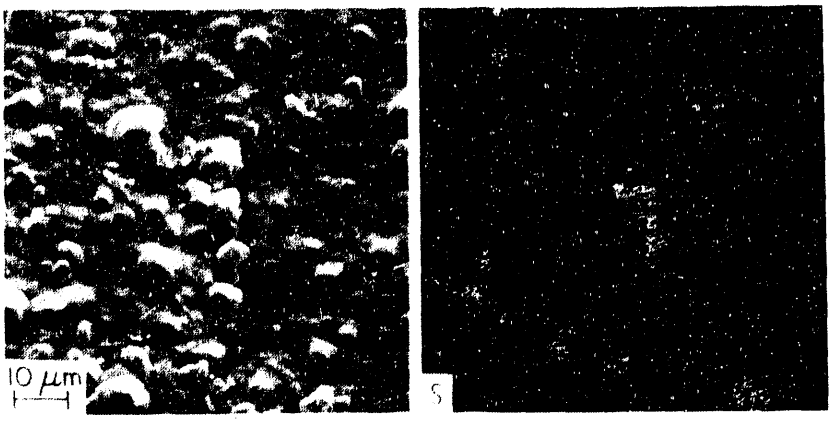

Fig. 30. SEM micrograph and sulfur mapping of surface of Type 310 stainless steel after exposure to gas mixture 8 (sulfide particles are rich in Mn)

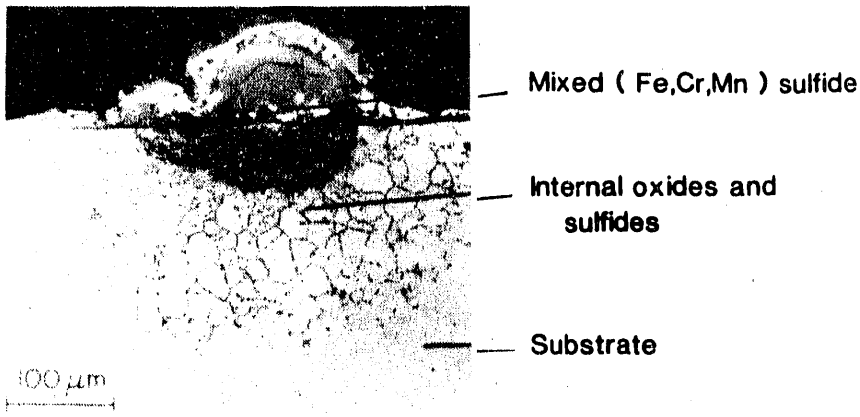

Fig. 31. SEM micrograph of cross section through Type 310 stainless steel after exposure to gas mixture 8

Behavior of Modified Alloys

In describing the effects of alloying additions of Zr or Nb on corrosion behavior, it is useful to make direct comparisons with the behavior of the unmodified, pure ternary alloy. In the first instance, additions of Zr or Nb promote the oxidation reaction over the sulfidation reaction so that the threshold boundary for the modified alloys is shifted to the left. The degree to which the boundary is shifted depends on the concentration of the refractory metal addition. In gas mix 7, alloys containing 3 or 6 wt.% Zr (1, 3, or 6 wt.% Nb) formed and maintained protective scales for test times up to 300 h at 875°C, while alloys containing only a 1 wt.% addition of Zr underwent continuous rapid degradation (see Fig. 32). All modified alloys degraded rapidly in gas mix 5. While Zr or Nb promoted oxide formation in gas mix 4, the presence of the particulate oxide did not appear to inhibit continued development of a relatively thick (40–70 μm) sulfide scale, presumably because of its inability to form a complete barrier layer. Although growth of a sulfide dominates the kinetics of scale formation in gas mix 4, the rate of growth is approximately parabolic, and rate constants for all alloys are in the range of 10^{-10}–10^{-11} $g^2\ cm^{-4}\ s^{-1}$. Assuming that the scale formed is Cr_3S_4, a rate constant of 10^{-10} $g^2\ cm^{-4}\ s^{-1}$ corresponds to a metal loss of 85 μm in one year, which may not appear excessive.

In gas mix 6, specimens of all alloys were totally consumed within 100 h of exposure at 875°C. Examination of the scales revealed evidence of a liquid phase at the elevated temperature of test. Chemical analysis showed the scale to contain large quantities of Fe and Ni. Considerable phase separation/dissociation appears to have occurred during the cooling process; therefore, it is possible only to speculate as to the phases present at the temperature of exposure. Iron forms a highly defective sulfide (FeS_{1+x}) that grows at a high rate and has a melting point of 1195°C.[37] Nickel sulfide "NiS" may melt at 637°C, although melting points of various Ni sulfides rich in S can be as high as 982°C.[38] When Fe joins in sulfide formation with Ni, the compound $(Fe,Ni)_9S_8$, with a melting point of 857°C, may form.[31] From the work completed thus far, it is possible to conclude that Fe and Ni become significant participants in the scaling process only at a pO_2 lower than those defining the position of the threshold boundary. However, with increasing pS_2, it is apparent that the tendency for a liquid phase to form increases such that the relative threshold pO_2 for

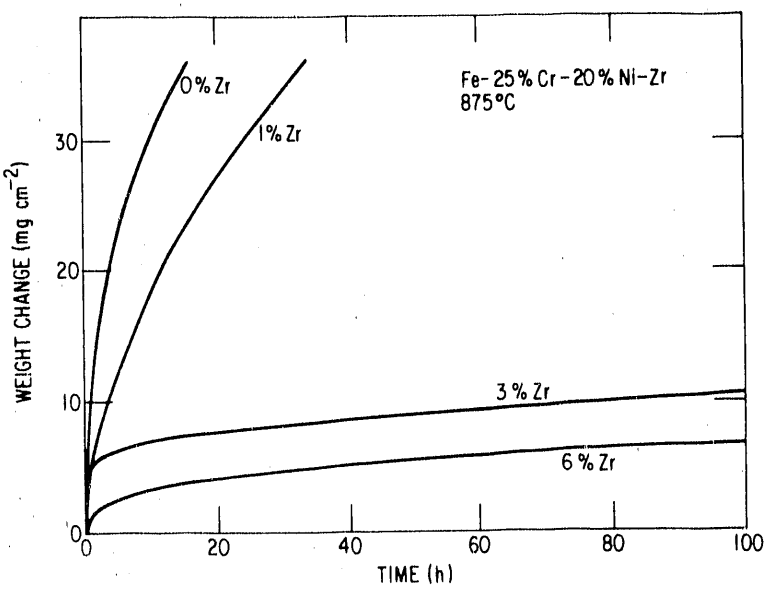

Fig. 32.
Kinetic data for Zr-modified and pure ternary Fe-25 wt.% Cr-20 wt.% Ni exposed to gas mixture 7

protective oxide scale formation at high pS_2 is increased (i.e., the ratio of threshold pO_2/pO_2 for Cr_2O_3–"CrS" equilibrium increases with increasing pS_2).

It was shown earlier that the presence of Zr or Nb induced a relative increase in the initial rate of oxidation of Fe–Cr–Ni alloys in sulfur-free environments. Both Zr and Nb form more thermodynamically stable oxides than do Cr, and thus they might be expected to compete more strongly for the available oxygen, particularly during the early stages of exposure until depletion leads to preferential oxidation of Cr. In addition, at least for Zr, an oxide can be formed at about four times the rate that Cr_2O_3 is formed.[28] These factors combined could therefore promote enhanced nucleation of the Cr_2O_3 that eventually forms the protective oxide layer. The speed with which the Cr oxide rate-controlling surface layer can be established is important in determining the level of undesirable species, such as sulfides, incorporated into the scale during the transient stages of growth. The enhanced rate of formation of a protective scale is the first step in providing additional protection of alloys containing Zr or Nb. It is not the only step, however. Tests on pre-oxidized material reveal, in addition, that the presence of the refractory elements affects the breakdown characteristics of oxide scales, the details of which will be discussed later in this report.

Tests were carried out for periods of up to 5000 h in gas mix 10. While Type 310 stainless steel exhibited random behavior in that breakaway kinetics were sometimes observed, the pure ternary and modified alloys exhibited only protective behavior. The apparent negative effects of the presence of Si and Mn in Type 310 stainless steel have already been discussed, but additional information concerning effects of the refractory metal additions is presented. Scale/metal contact, which conceivably is one of the major factors influencing scale adhesion to the substrate, is not affected by the formation of voids in these alloys, unlike on the unmodified pure ternary alloy (see Fig. 33). In addition, presumably due to enhanced nucleation and the increased speed of establishment of a protective surface layer, additions of Zr or Nb reduced or eliminated the tendency for a layer of sulfide to form at the scale/metal interface as shown in Fig. 33 for the pure ternary alloy. The refractory additions promote formation of a rough, undulating scale/metal interface with evidence of inward growth of oxide (Fig. 34). Oxides formed from Zr- or

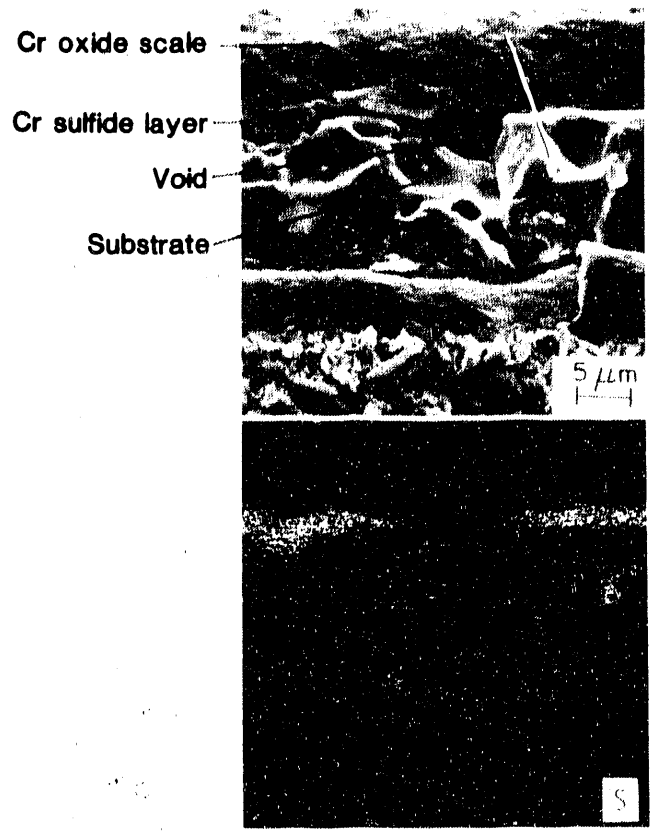

Fig. 33.
Scale/metal interface region of pure ternary alloy exposed to gas mixture 10

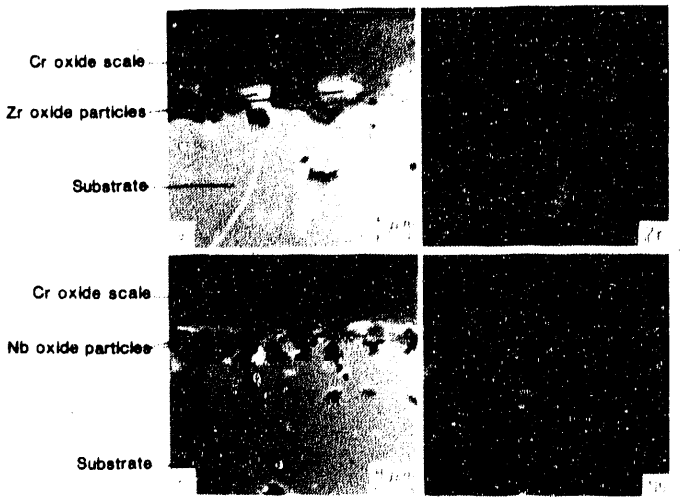

Fig. 34.
Cross sections through (a) 3 wt.% Zr and (b) 3 wt.% Nb alloys exposed for 5000 h to gas mixture 10

Nb–containing intermetallic particles near the original metal surface of the alloy are gradually engulfed by growth of Cr oxide as oxidation proceeds. Inward growth of oxide by the predominance of anion diffusion, as opposed to the normal cation-controlled growth of Cr_2O_3, can be promoted by the presence of reactive elements.[8,9] Although changing the scale growth mechanism should diminish the problem of vacancy condensation at the scale/metal interface and may also have some effect on the transport of impurity species such as sulfur, formation of new oxide in the confines of the scale/metal interface region could possibly result in the generation of more stress than when scale is formed by the

cation diffusion mechanism. If the mechanical integrity of the scale is a prime property governing its stability and resistance to breakdown, the question of the scale growth mechanism will be important.

Protective oxide scales formed on all the modified alloys in gas mixtures 1–3, 8, and 10, with rate constants in the range of 10^{-12} to 10^{-13} g^2 cm^{-4} s^{-1} at 875°C. The major difference in behavior between the modified alloys and the pure ternary alloy is the degree to which internal oxidation occurs. The presence of the refractory elements results in the formation of internal oxides in the alloys (mainly in the locations of intermetallic particles) to depths of 20–30 μm. As with Type 310 stainless steel, it appears that the internal oxides also enable penetration of sulfur to form intergranular sulfides to depths of 5–10 μm greater than the deepest oxides, even though no sulfur could be detected in the scales. Zirconium could not be detected in the scale on the Zr-modified alloys; the scales consisted of nearly pure Cr_2O_3. On the Nb-modified alloys, Cr_2O_3 forms, but in addition, Nb contributes to the formation of either a mixed (Nb,Cr) oxide or Nb_2O_5, according to X-ray diffraction data.

Upon exposure of the Nb-modified alloy to an oxidizing environment at 1000°C, it was found that a discrete layer of Nb oxide could form (see Fig. 35). At a pO_2 of 10^{-16} atm with or without sulfur (i.e., pS_2 too low to support sulfidation as the dominant reaction), a discrete layer of oxide, 1 μm thick, formed between the outer Cr-rich oxide and the metal substrate in 100 h of oxidation. Analysis by X-ray diffraction showed the two layers to be Cr_2O_3 and Nb_2O_5, respectively. Sulfur resistance of the two-layer scale will be discussed in the next section of this report.

3.2.4 Behavior of Preoxidized Material

Due in part to poor behavior exhibited by the chromia-forming alloys in relatively high-pO_2 environments and the possibility of structural alloys experiencing sulfidation attack due to changes in operating conditions after an oxide had formed, it was considered necessary to examine the behavior of preformed oxide scales in a systematic manner. On the premise that reaction kinetics strongly influence the nature of corrosion in environments in which both oxides and sulfides are stable, it should be possible to extend the useful life of an alloy by eliminating sulfur from the starting gas mixture and thus removing the competition between the two reactants. Preoxidation of alloys in sulfur-free environments permits protective oxide scales to form before their exposure to sulfur. Following preoxidation, the rate of alloy degradation depends on the ability of the preformed oxide layer to form a barrier layer between the alloy and the S-containing gaseous atmosphere. The protective nature of preformed oxide scales is thus a subject of considerable interest. The present investigation was conducted to evaluate the behavior of preformed protective oxide scales on Fe-Cr-Ni base alloys and those modified by Zr and Nb additions. The aims of the investigation were to (1) determine the ability of preformed oxide scales to extend alloy life, and (2) establish the mechanism of scale breakdown.

Scaling in Preoxidation Environments

Preoxidation at both 875 and 1000°C was conducted in low-pO_2 atmospheres in which only Cr, Zr, and Nb could form thermodynamically stable binary oxides. The rate of scale formation on all alloys was parabolic and the rate constants ranged from 4×10^{-13} to 1×10^{-12} g^2 cm^{-4} s^{-1} at 875°C and from 1×10^{-11} to 2×10^{-11} g^2 cm^{-4} s^{-1} at 1000°C. At both temperatures, the slightly higher rates of oxidation occurred for the pure ternary alloy.

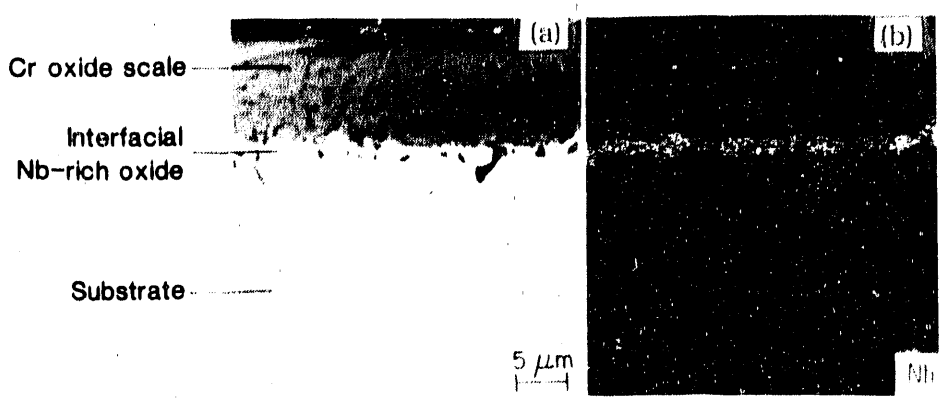

Fig. 35. (a) Cross section of an Nb-modified alloy specimen after preoxidation at 1000°C, showing two-layer scale; (b) Nb X-ray map

For pure Cr at 875°C, the oxidation rate constant was 8×10^{-12} g^2 cm^{-4} s^{-1}. The duration of transient oxidation was approximately twice as long for the pure ternary alloy as for the modified alloys, i.e., ≈2 h and <1 h were recorded for the latter alloys at 875 and 1000°C, respectively. Scale thicknesses of 3-4 μm at 875°C and 8-10 μm at 1000°C were obtained after 100-h exposures.

The sesquioxide, Cr_2O_3, was the principal constituent of the scales on all alloys. Approximately 0.75% of the metal-ion content of the oxide in the pure ternary alloy was Fe, compared with only 0.14% in the Zr-modified alloy, but oxidation of Zr-containing intermetallic particles on the surface of the latter alloy substrate resulted in the incorporation of some ZrO_2 into the surface scale. The ZrO_2 was contained predominantly in discrete oxide nodules (see Fig. 36) that were approximately twice the thickness of the remaining scale. Some Zr was detected at the scale/metal interface. ZrO_2 also formed internally on alloy grain boundaries. At 875°C, the Nb-modified alloy had a mixed (Nb,Cr) oxide, most prominently in regions where Nb-containing intermetallic particles were oxidized. A zone of material 10-20 μm wide at the alloy surface was free of Nb because of its incorporation into the scale. At 1000°C, the zone of Nb depletion was wider, and Nb contributed to the formation of a continuous discrete layer of Nb oxide beneath the Cr_2O_3 layer (see Fig. 35). The rate constant for the formation of the latter composite scale was 1.4×10^{-11} g^2 cm^{-4} s^{-1}.

No evidence of mechanical damage could be detected on any alloy during the isothermal growth process. However, spallation occurred over approximately 10% of the surface area of pure ternary alloy specimens on cooling. Distinct voids were evident at the scale-metal interface. Less severe spallation, particularly at specimen edges, occurred on the Nb-modified alloy oxidized at 875°C, although interfacial voids were absent. No scale spallation was evident on either the Nb-modified alloy oxidized at 1000°C or the Zr-modified alloy oxidized at 875 or 1000°C.

Scaling in O_2/S_2 Environments at 875°C

Earlier work showed that the threshold pO_2 values for protective scale formation on a pure ternary Fe-25 wt.% Cr-20 wt.% Ni alloy at 875 and 1000°C were 3.7 and 3.0 orders of magnitude greater, respectively, than the pO_2 values defining equilibrium between Cr_2O_3

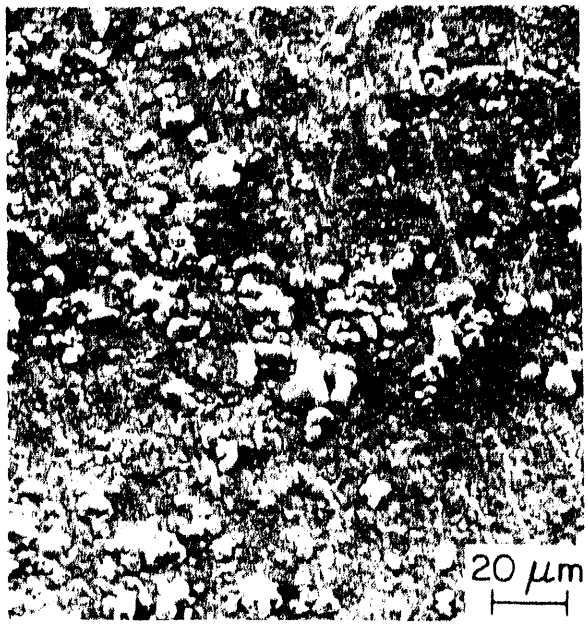

Fig. 36.
SEM micrograph of outer surface of Zr-modified alloy specimen after preoxidation for 72 h at 875°C, showing nodular morphology of oxide scale

and CrS_{1+x}.[39] Alloying with 3 wt.% Zr or Nb reduces the level of excess oxygen required for surface oxide scale formation by approximately 1.5 orders of magnitude at both temperatures (see Figs. 37 and 38).[39,40] Chemical compositions and reactant activities of oxygen/sulfur in gas mixtures used for this study are listed in Table 8. At 875°C in gas mixture A (Fig. 37), nonpreoxidized specimens of the pure ternary alloy sulfidized, whereas the Zr- or Nb-modified alloys formed protective oxide scales. In gas mixture B, all alloys exhibited rapid sulfidation. At 1000°C (Fig. 38), the nonpreoxidized pure ternary and 3 wt.% Zr- or Nb-modified alloys exhibited breakaway corrosion and protective scaling behavior, respectively, in gas mixture C. Breakaway corrosion occurred on all nonpreoxidized alloys in gas mixtures D, E, and F. In general, pure Cr exhibited oxidation/corrosion behavior similar to that of the pure ternary alloy, with the threshold boundary for protective oxidation on nonpreoxidized alloy similarly placed

To evaluate the influence of preformed oxide scales on the threshold level of oxygen required to maintain protection by the scales, all alloys were preoxidized for 72 h and subsequently exposed to a series of gas mixtures with successively lower pO_2 and higher pS_2 levels. Breakaway corrosion occurred with only a slight shift in gas composition, toward either increasing pS_2 or decreasing pO_2, from the threshold boundary values for the nonpreoxidized alloys. The protection by the preformed oxide was maintained for <10 h. A typical weight-change curve associated with breakaway corrosion is shown in Fig. 39. For the pure ternary alloy in gas mixture A over a period of approximately 1 h, the rate of scale growth changed from a low rate (similar to that under preoxidation conditions) to a high rate of linear growth. In the same gas mixture, the modified alloys did not exhibit breakaway corrosion during 150 h of exposure before the tests were terminated, but the rates of scale growth were approximately linear ($\approx 1.7 \times 10^{-9}$ g cm^{-2} s^{-1}). In the modified alloys, breakaway corrosion occurred upon exposure to gas mixture B.

The specimens exposed in gas mixture B were used to explore the relationship between time of preoxidation and time of time to onset of breakaway corrosion. In general, increasing the time of preoxidation in the range from 4 to 200 h increased the time

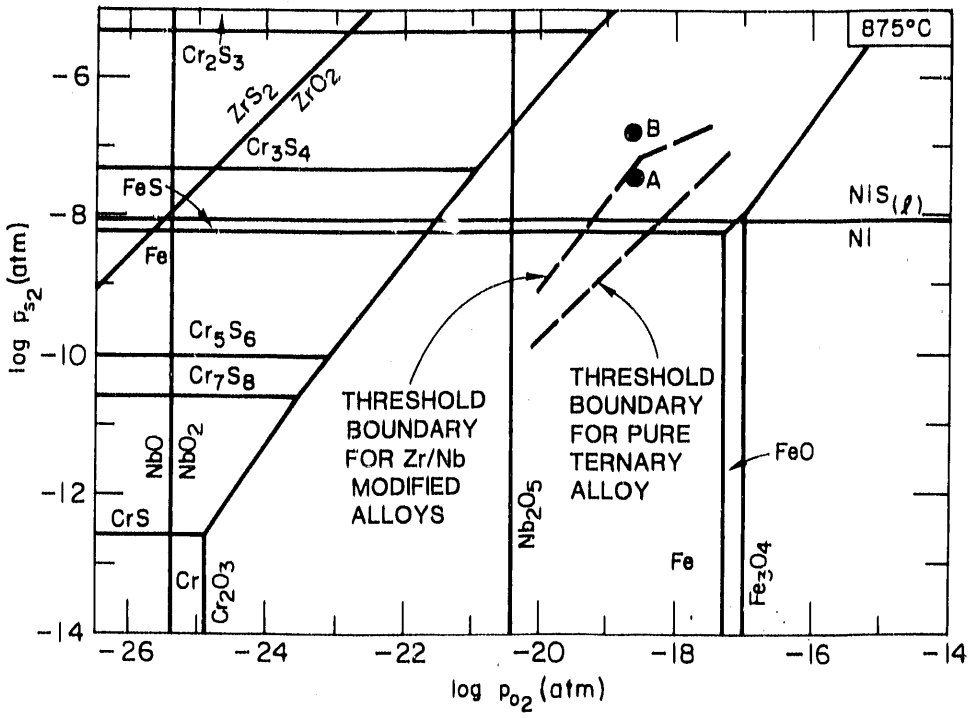

Fig. 37. Thermochemical stability diagram for Fe–S–O, Cr–S–O, Ni–S–O, Zr–S–O, and Nb–O systems at 875°C, with threshold pO_2 boundaries for alloys in both preoxidized and nonpreoxidized conditions. Black symbols represent gas mixtures used.

required for the initiation of breakaway corrosion (see Fig. 40). However, there is wide scatter in the data even though the tests were conducted under nominally identical conditions. For short times of preoxidation (<50 h), breakaway occurred within 5 h of admitting the O_2/S_2 gas mixture. For longer times, an incubation period ranging from 6 to 50 h was observed before breakaway corrosion occurred. Once breakaway corrosion initiated, the subsequent rate of scale growth was high and approximately linear. In the case of pure Cr, sulfidation occurred after an incubation period of approximately 2 h in gas mixture A, but the rate of subsequent scale growth -- although almost linear -- was relatively low.

During the early stages of exposure to the S-containing environment, the sulfur concentration in the outer region of the oxide scale increased, as shown in Fig. 41. Within a short time, discrete particles of Cr-rich sulfide nucleated on the surface of the oxide scale, as shown in Fig. 42. The particles were randomly dispersed over the oxide surface, and their formation marked the beginning of an increase in the rate of weight gain. Over much of the specimen surface, these sulfides particles continued to grow relatively slowly for many hours, while the preformed oxide layer largely retained its integrity. However, in some areas, particularly around specimen corners and holes (used for suspension in the thermogravimetric experiment) and along specimen edges, complete loss of protection by the preformed oxide occurred (see Fig. 43) and formation of a thick surface-sulfide layer and internal sulfidation of the alloy followed rapidly. In a single case, total breakdown of the

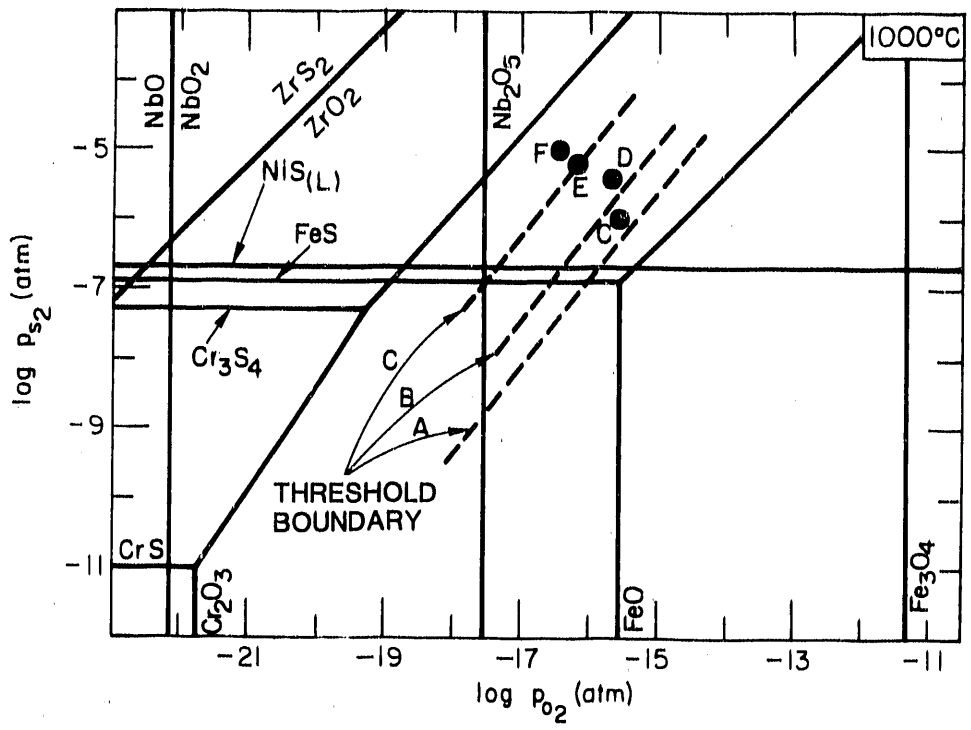

Fig. 38. Thermochemical stability diagram for Fe–S–O, Cr–S–O, Ni–S–O, Zr–S–O, and Nb–O systems at 1000°C, with threshold pO_2 boundaries for (a) preoxidized and nonpreoxidized pure ternary alloy, (b) preoxidized and nonpreoxidized Zr-modified alloy and nonpreoxidized Ni-modified alloy, and (c) preoxidized Nb-modified alloy. Black symbols represent gas mixtures used.

Table 8. Gas compositions and partial pressures of oxygen and sulfur in gas mixtures used in the exposure of preoxidized specimens

Gas Mix	Gas Composition (vol.%)					T (°C)	Reactant Activities	
	CO	CO_2	CH_4	H_2S	H_2		pO_2 (atm)	pS_2 (atm)
A	13.05	13.05	2.90	0.479	70.50	875	2.1×10^{-19}	3.80×10^{-8}
B	13.05	13.05	2.90	1.03	69.97	875	2.1×10^{-19}	1.90×10^{-7}
C	25.40	25.40	5.65	0.493	42.985	1000	3.3×10^{-16}	5.80×10^{-7}
D	30.00	30.00	6.67	0.758	32.542	1000	3.4×10^{-16}	2.41×10^{-6}
E	15.00	15.00	3.33	2.268	64.432	1000	5.9×10^{-17}	6.60×10^{-6}
F	12.00	12.00	2.67	2.70	70.60	1000	3.6×10^{-17}	7.90×10^{-6}

preformed oxide (after 47 h) occurred on a flat surface. The point at which rapid sulfidation initiated was marked by the formation of a continuous channel of sulfide across the oxide scale (see Fig. 44).

In general, the sulfide channels did not widen with time as both surface and internal oxide/sulfide nodular growths expanded outward from the initial points of breakthrough

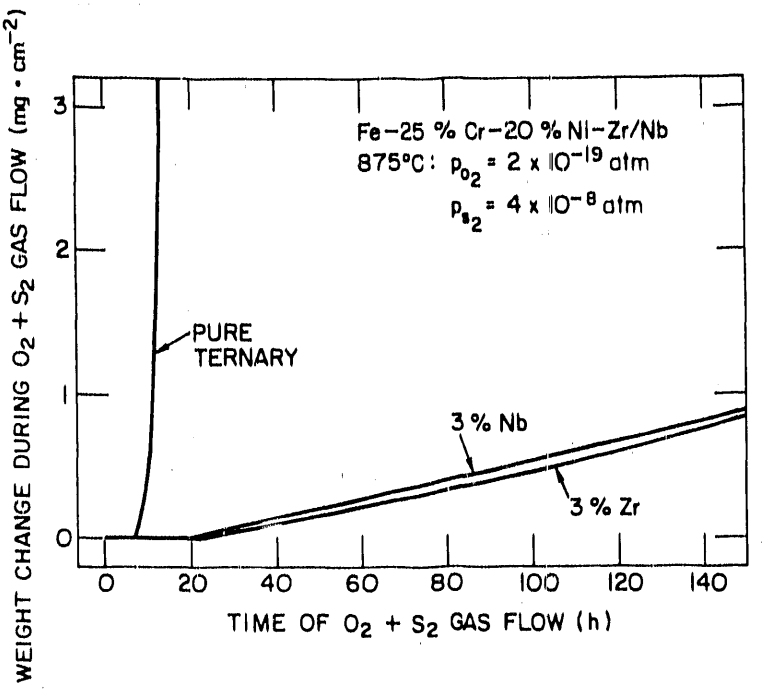

Fig. 39.
Thermogravimetric test data for alloys exposed to gas mixture A at 875°C following preoxidation for 72 h at 875°C in atmosphere with $pO_2 = 2 \times 10^{-19}$ atm

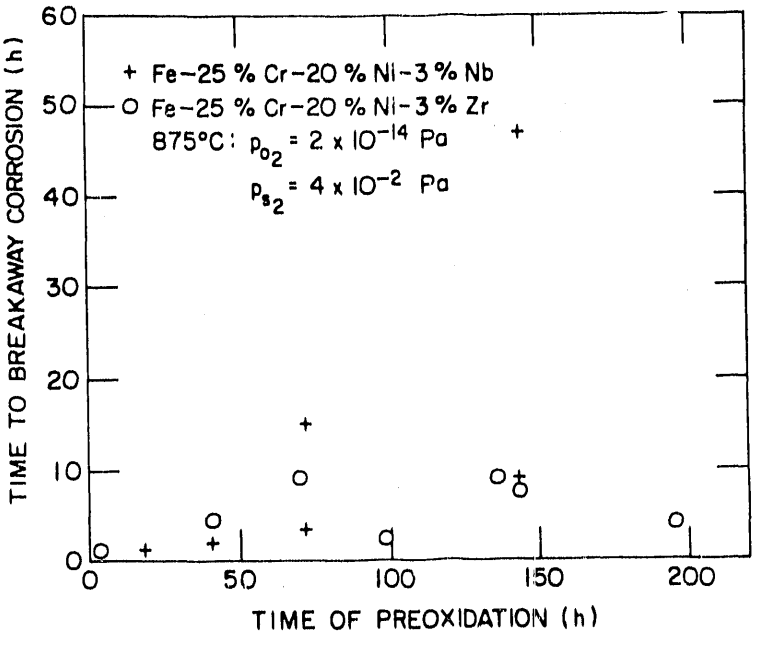

Fig. 40.
Thermogravimetric test data for alloys exposed to gas mixture A at 875°C following preoxidation for 72 h at 875°C in atmosphere with $pO_2 = 2 \times 10^{-19}$ atm

(Fig. 45). From the time when breakaway sulfidation was initiated, the composition of the surface sulfide rapidly changed from almost pure Cr sulfide to Fe-rich sulfide. With increasing pS_2, the proportion of Ni in the sulfide scale increased. At 875°C, Ni contributed to the formation of liquid-sulfide corrosion products whose presence further accelerated the rate of alloy degradation. Intergranular Zr or Nb sulfides formed ahead of the internal sulfur penetration in the alloys. The mode of breakdown of the preformed oxide scales was the same for all alloys studied in the present investigation.

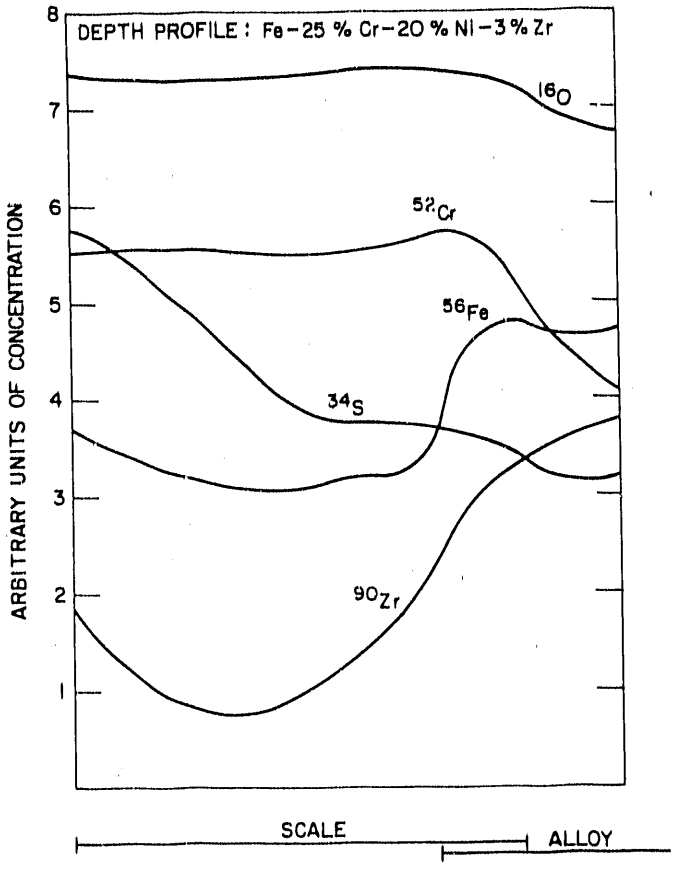

Fig. 41.
Elemental concentration profiles obtained by secondary ion mass spectroscopy across the scale in Fe–25 wt.% Cr–20 wt.% Ni-3 wt.% Zr specimen preoxidized for 72 h at 875°C and subsequently exposed to gas mixture B for 23 h

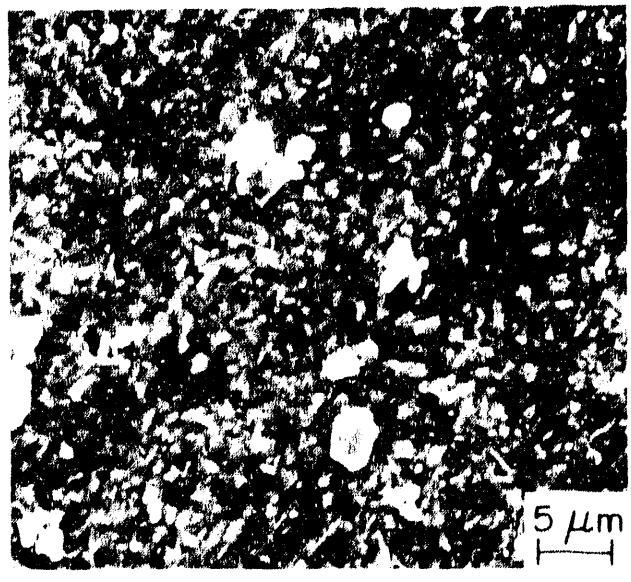

Fig. 42.
SEM micrograph of outer surface of Fe–25 wt.% Cr–20 wt.% Ni–3 wt.% Nb specimen preoxidized for 72 h at 875°C and subsequently exposed to gas mixture B, showing discrete (light) Cr-rich sulfide particles

Scaling in O_2/S_2 Environments at 1000°C

Corrosion tests conducted with several levels of pO_2 and pS_2 showed that preoxidation induced a negligible shift in the position of threshold boundaries for oxide formation established for nonpreoxidized pure ternary and Zr-modified alloys. In each case, for a preoxidation time of 100 h, the incubation period before the initiation of breakaway

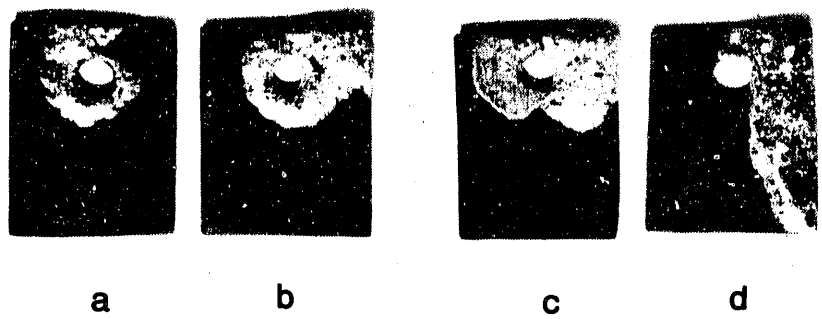

Fig. 43. Macrographs of specimens preoxidized at 875°C and exposed to gas mixture B, showing localized nature of breakaway corrosion. (Top) Zr-modified alloys after (a) 70-h preoxidation and (b) 143-h preoxidation; (bottom) Nb-modified alloys after (c) 143-h preoxidation and (d) 18-h preoxidation.

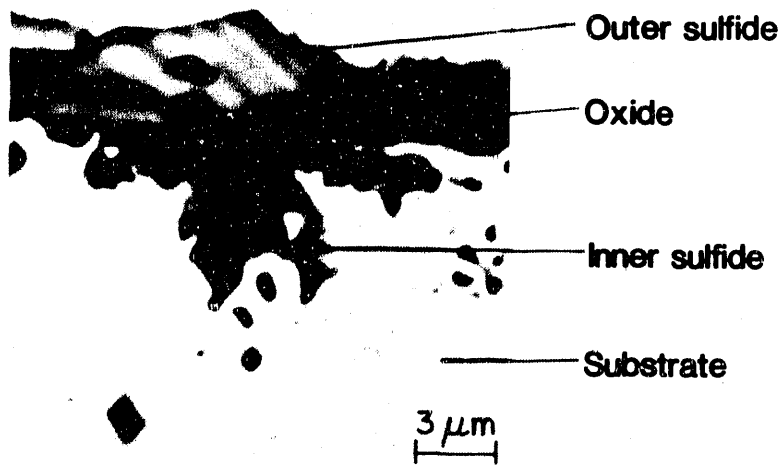

Fig. 44. Cross section of pure ternary alloy specimen after preoxidation at 875°C and exposure to gas mixture A, showing presence of sulfide phase across preformed oxide scale

corrosion was <6 h. In contrast, preoxidation resulted in a substantial improvement in the ability of the Nb-modified alloy to resist rapid degradation. At a given pS_2 value, the pO_2 level required to cause breakaway corrosion was approximately 1.5 orders of magnitude lower that of the threshold boundary for the nonpreoxidized alloy. Breakaway corrosion occurred consistently within 20 h of exposure to gas mixture F. In gas mixture E, a high linear rate of sulfidation was not induced, but the formation of Cr-rich sulfide at the scale/gas interface resulted in a substantial increase in the rate of weight gain for the specimen.

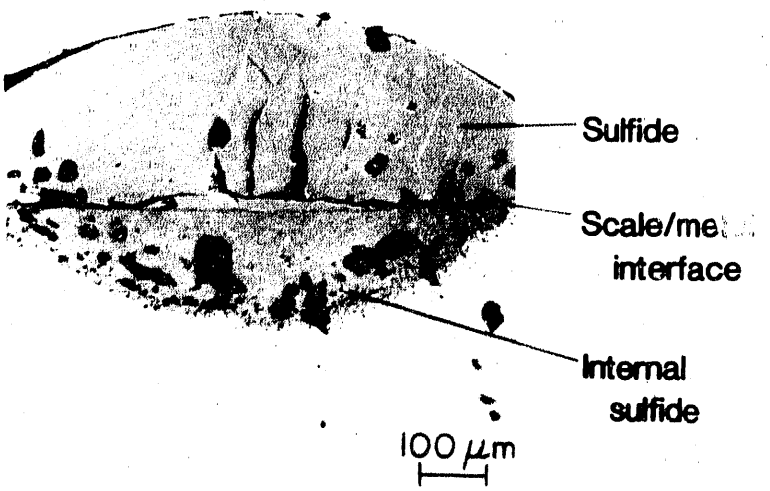

Fig. 45.
Cross section of thick sulfide scale and deep internal of Fe–25 wt.% Cr–20 wt.% Ni–1 wt.% Zr after complete loss of protection of preformed oxide scale. Preoxidation and sulfur exposure periods were 95 and 21 h, respectively.

The mode of breakdown of protection of the two-layer scale in the Nb-modified alloy preoxidized at 1000°C was closely similar to that observed for the other alloys. The buildup of adsorbed sulfur at the scale/gas interface led to the nucleation of sulfide particles, initially rich in Cr (Fig. 46). Continued exposure permitted growth of the sulfide particles, leading to an increased rate of weight gain, and an eventual breach of the protective oxide layers. Breakaway occurred locally, usually at specimen edges and corners, and lateral growth was mainly responsible for the rapid coverage of the preformed oxide scale with Fe-rich sulfide.

The effectiveness of preformed oxide scales in inhibiting breakaway corrosion in structural alloys exposed to O_2/S_2 mixed-gas atmospheres can be measured in two ways. First is the length of time that protection is maintained in the environment before breakaway corrosion initiates relative to that for nonpreoxidized alloys. The second is the degree to which the threshold oxygen partial pressure for protective oxide scale maintenance is shifted to lower pO_2 levels because of the presence of a preformed oxide scale. For the alloys studied, when breakaway corrosion occurred, it initiated within 20 h of the beginning of exposure to the O_2/S_2-containing gas mixture. Only for the Nb-modified alloy preoxidized at 1000°C was a substantial shift in the threshold boundary observed. The threshold boundary shift for the Nb-modified alloy at 1000°C gives a much wider envelope in terms of pO_2 and pS_2 ranges in which the alloy should exhibit protective scaling behavior.

In the present experiments, sulfur entered the oxide scale and established a concentration profile of the form shown in Fig. 41. The initial absence of sulfur in the preoxidized specimen ensured inward transport of sulfur. The diffusion coefficient for sulfur in Cr_2O_3, established by tracer techniques, is reported to be 1 to 2 x 10^{-10} cm^2 s^{-1} in the temperature range of 875 to 1000°C.[41,42] These data can be compared with the diffusivity value of 10^{-12} cm^2 s^{-1} and 10^{-17} cm^2 s^{-1} for Cr^{3+} and O_2- ions, respectively, in Cr_2O_3 at 1000°C.[43,44] The higher diffusion rate of S relative to Cr or O suggests that sulfidation could occur beneath the scale/gas interface. Indeed, accelerated rates of corrosion have been attributed to a mechanism by which sulfur diffuses to the scale/metal interface where sulfides form,[45] although for this mechanism to operate, molecular transport of SO_2 is assumed. In addition, sulfur transport via oxygen vacancies,[46] albeit in single crystals of NiO, and via grain boundaries[47] has been proposed. Alternatively, development of mechanical defects,[48] often influenced by specimen geometry,[49] can permit access of S-containing gas to the metal

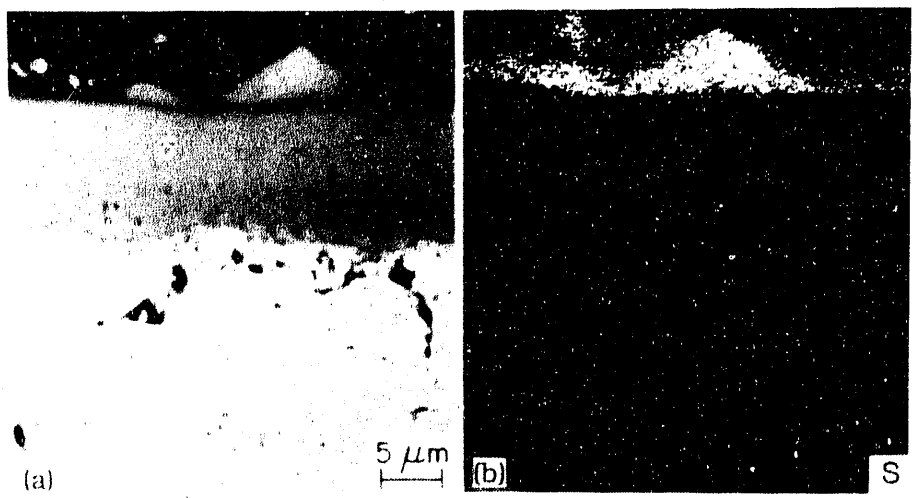

Fig. 46. (a) Cross section of Fe–25 wt.% Cr–20 wt.% Ni–3 wt.% Nb specimen after preoxidation at 1000°C, showing discrete sulfide particle on outer surface of oxide scale; (b) sulfur X-ray map

surface where sulfide phase can form. However, in the present work and past studies on preformed Cr_2O_3 scales exposed to oxygen/sulfur mixed-gas environments, the sulfide phase nucleated predominantly at the scale/gas interface.[13,15,18,20,50,51]

The thermodynamic stability data (Figs. 37 and 38) suggest that in any of the S-containing environments used in the present investigation, the sulfide formed at the scale/gas interface should be either FeS or an Fe-containing spinel sulfide; however, the sulfide particles that developed on the sample surfaces were predominantly CrS_{1+x} and were almost devoid of Fe. Sulfide formation at the scale/gas interface may be facilitated by an increase in the diffusivity of Cr^{3+} ions in Cr_2O_3 when sulfur enters the oxide as an electron donor and reduces the electron hole concentration, thereby increasing the Cr defect concentration.[52] The enhanced rate of Cr transport, by up to three orders of magnitude,[51,52] facilitates formation of sulfides on the scale surface. The approximately linear rate of subsequent scale formation suggests that the recorded weight increase is primarily due to the growth of sulfide particles, while the thickness of the oxide remains comparatively constant.

Iron may play an important role in the breakdown of Cr_2O_3 scales on Fe-base alloys. The presence of sulfur in the gaseous atmosphere can lead to increased concentrations of Fe in Cr_2O_3 scales,[16,20] which can promote formation of Cr-rich sulfide on the outer scale surface.[50] The Fe content in preformed oxide scales was dependent on the alloy composition. The levels of 0.14 and 0.75% Fe in Cr_2O_3 on the modified and pure ternary alloys, respectively, are attributable to a combination of shorter transient oxidation times for the Zr- and Nb-modified alloys and lower dissociation pressures owing to the presence of Zr or Nb oxides in the Cr_2O_3 scale or at the scale/metal interface. In Cr_2O_3, Fe increases the entropy of the oxide, owing to increased atomic disorder, which reduces its thermodynamic stability.[53] Iron also affects the mechanical properties of Cr_2O_3, enhancing the tendency for spallation.[54] With Fe in Cr_2O_3, Fe-doped CrS_{1+x} forms more readily than does pure CrS_{1+x}.[50] Once breakaway initiates, alloy degradation occurs at a significantly higher

rate for Fe-base alloys than for pure Cr. However, because breakdown of protection of Cr_2O_3 on pure Cr occurs at pO_2 values higher than those corresponding to Cr_2O_3/CrS_{1+x} equilibrium, Fe cannot be solely responsible for the initiation of the breakdown process. Although Fe concentration in the surface sulfides increased with time over much of the surface area of preoxidized specimens, complete breakdown of the oxide scale did not occur within 150 h of exposure.

Complete breakdown of the preformed oxide almost always occurred at specimen edges, corners, or around the suspension hole. The localized nature of breakaway corrosion on flat surfaces may be attributable to nonuniformities in scale thickness and/or morphological effects. The oxidation of reactive-element-containing intermetallic particles at the alloy surface can result in oxide nodule formation in the surface scale; the interfaces between the nodules and the adjacent scale, acting as easy diffusion paths, can act as initiation sites for breakaway corrosion. This mechanism has been demonstrated for Y-containing alloys,[15] but for the nodular scales on Zr-modified alloys, similar behavior was not observed. Localized variations in scale composition, other than those caused by the presence of the nodules, were not observed. However, it should be stressed that detailed characterization of the grain and grain boundary structures and grain sizes is needed before the influence of scale morphology on the resistance of oxide scales to breakdown by sulfur can be established. The characterization of oxide scales should also include an evaluation of stress distribution in the scales and the substrate alloy and formation of defects such as voids and cracks. Although the mechanical behavior of surface oxide scales has been evaluated in a primarily qualitative manner to date, evidence strongly suggests that mechanical effects play a large role in the breakaway process.

Stresses are generated during the growth of surface scales. The magnitude of the stresses can be large enough to cause deformation in the underlying substrate,[55] or in some cases may result in fracture.[48] Curved metal surfaces and sharp edges act to magnify the level of stress, thereby increasing the need for stress relief.[56] Microcracking, which is observed for some scale/alloy systems,[48] should occur where stresses are highest, that is, at specimen edges and corners. During cooling, spallation of the scale occurred mainly at specimen edges and around the suspension hole, indicating the potentially mechanically weak areas of scale-covered specimens. In addition, if sulfur migrates to the scale/metal interface, which it can do in approximately 0.5 h (based on a diffusion coefficient of 10^{-10} $cm^2\ s^{-1}$), adhesion of the scale to the substrate should be impaired,[56,57] rendering the scale more susceptible to mechanical damage. Because in almost all cases of breakaway corrosion, the initiation site was at a specimen edge or corner, the critical factor that promotes rapid sulfidation is most likely a mechanical defect.

A significant shift in the threshold boundary to lower pO_2 by preoxidation was only possible (in the time scale of the present experiments) for the Nb-modified alloy, and only at 1000°C. Because only the Nb-modified alloy formed a scale composed of two discrete layers upon preoxidation at 1000°C, the enhanced resistance to breakdown in sulfur-containing atmospheres can be attributed to this scale morphology. The precise composition of the Nb oxide layer was not established, but for stability to be maintained it should be either NbO or NbO_2. Although Nb oxide, like other refractory metal oxides, grows relatively fast, no data are available for the transport of sulfur or cations through it. However, when breakaway corrosion occurred, the operative mechanism appeared to be the same as that

described above for single-layer scales, in which mechanical defects were considered to play a dominant role.

The beneficial effects of Nb added to the bulk alloy have been observed only at 1000°C primarily because the exposure times used in the present investigation are not sufficient at lower temperatures to enable diffusion of Nb to the Cr_2O_3/alloy interface. An alternative approach of modifying the surface via Nb sputter deposition or Nb implantation may facilitate formation of two-layer protective scales at lower temperatures.

3.2.5 Analysis of Scale/Metal Interface Region

Scale/metal interface regions of specimens from several experiments were examined by mechanically stripping the scale from the substrate alloy or dissolving the substrate alloy in an acid solution. Figure 47 shows SEM photographs of the scale underside of a specimen of Fe–25 wt.% Cr–20 wt.% Ni–3 wt.% Zr alloy after exposure to a sulfur-free low-pO_2 environment at 875°C. Light regions in the photographs are predominantly Zr-oxide and seem to have formed in regions containing intermetallics, and the oxide is aligned with the rolling direction of the substrate alloy. The magnified photographs (top right and bottom left in Fig. 47) show that the ZrO_2 phase grew from the back side of the Cr_2O_3 (smooth region between ridges), and an additional phas of (Cr,Zr) oxide was observed between the ZrO_2 (light) and Cr_2O_3 (smooth) phases. The photograph in the bottom right in Fig. 47 shows the sample in 45° tilt position and indicates that the ZrO_2 is in filament form and is projecting into the alloy.

Figures 48 and 49 are SEM photographs of the alloy and scale sides of the scale/metal interface for an Fe–25 wt.% Cr–20 wt.% Ni ternary alloy after exposure to an O_2/S_2 environment with $pS_2 > pS_2$ for Fe–FeS equilibrium. It is evident from Fig. 48 that the metal side of the interface is heavily concentrated with voids, primarily along the grain boundaries. In Fig. 48, the metal is thicker toward the bottom and as a result, twins within grains and a ridge of metal at grain boundaries are clearly visible. In the top portion of the photograph, the twins disappear, grain boundary voids become prominent, and no oxide can be seen protruding into substrate. The photographs in Fig. 49 shows typical areas on the scale side of the interface in which the voided regions are spotty and a continuous smooth Cr_2O_3 layer is predominant. The top right corner of the picture on the right in Fig. 49 is undissolved metal and the few isolated particles are sulfides. The sulfide particles are away from the grain boundaries and probably formed during the early transient stage of oxidation. As oxidation proceeds, sulfide is converted into oxide and the released sulfur is driven further into the alloy.

Figure 50 shows SEM photographs of the alloy and scale sides of the scale/metal interface for an Fe–25 wt.% Cr–20 wt.% Ni–3 wt.% Zr specimen after exposure to an O_2/S_2 mixed gas environment with $pS_2 > pS_2$ for Fe–FeS equilibrium. The light areas of the photographs correspond to the ZrO_2 phase, which is present on both sides of the scale/metal interface. The smooth and nodular regions in the top photographs depict Cr_2O_3 scale; also, some undissolved alloy can be seen at isolated locations. A comparison of these morphologies with those in Figs. 48 and 49 clearly shows the absence of interfacial voids in the Zr-modified alloy. Figure 51 shows the SEM photographs and energy-dispersive X-ray (EDAX) mapping for Nb and Si of the scale side of the scale/metal interface on Fe–25 wt.% Cr–20 wt.% Ni–3 wt.% Nb alloy after exposure at 1000°C to an oxygen/sulfur mixed gas with $pS_2 > pS_2$ for Fe–FeS equilibrium. The oxide scale is Cr_2O_3 with significant

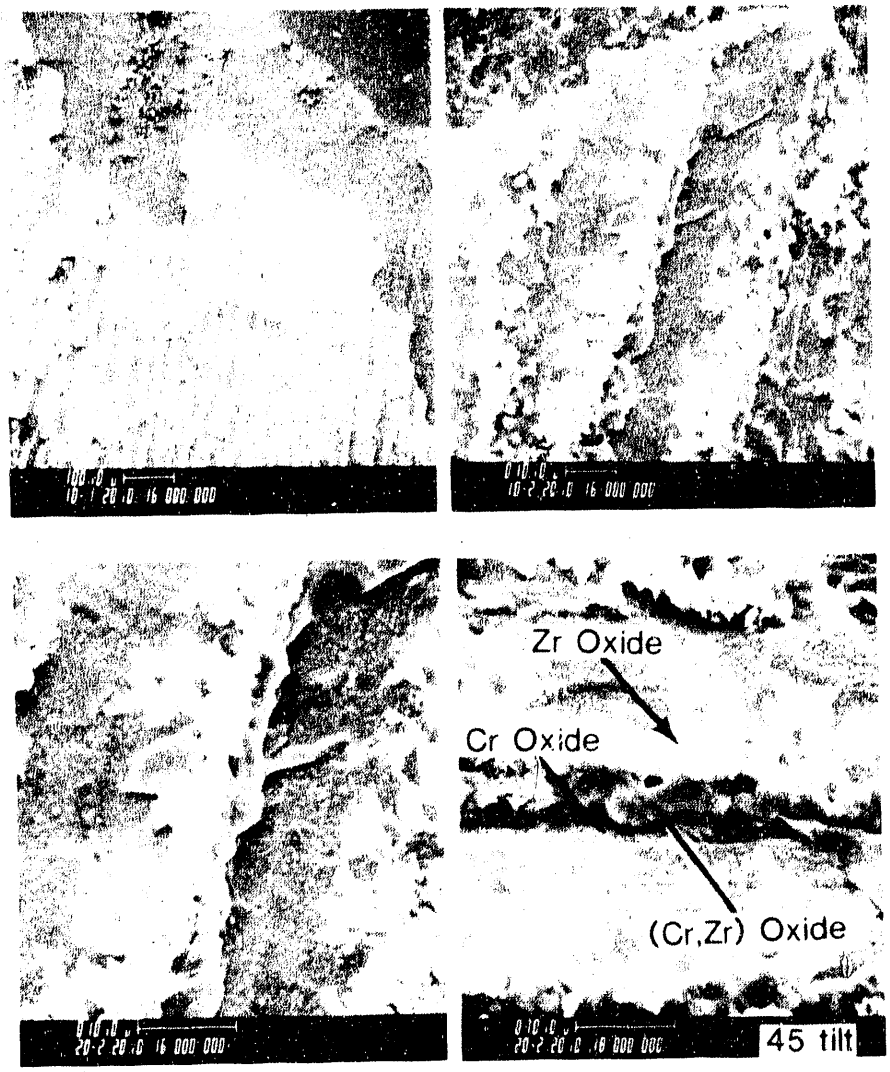

Fig. 47. SEM photographs of scale side of scale/metal interface on Fe-25 wt.% Cr-20 wt.% Ni-3 wt.% Zr after exposure to sulfur-free low-pO_2 environment at 875°C

enrichment of Nb, substantiated by the elemental mapping. Some undissolved alloy can also be seen in the photographs. The Cr_2O_3 scale is granular but no sulfur was detected. EDAX analysis also showed that the grain boundaries in the scale side of the scale/metal interface (probably a replica of the alloy grain boundary because the grain size of the alloy containing 3 wt.% Nb is in the range of 8 to 10 μm) are enriched in Si that is probably present as silica. The Nb-modified alloys initially contained 0.23 to 0.42 wt.% Si. The absence of sulfur on either side of the scale/metal interface signifies that the Nb/Si enriched layer can act as a barrier to migration of both base metal cations outward and sulfur inward. In addition, the absence of voids in the interface region, coupled with the pegging effect of oxide protrusion, can only improve the adhesion of the scale to the substrate alloy.

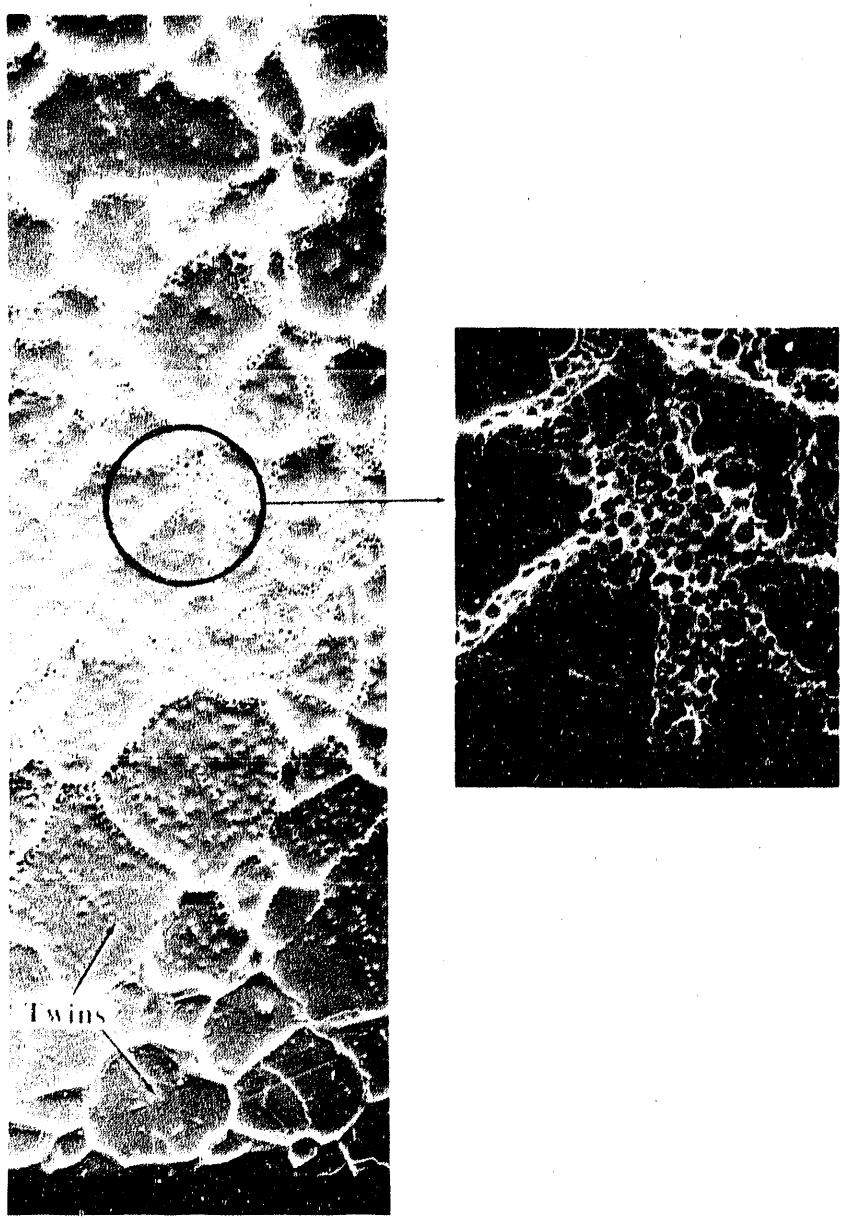

Fig. 48. SEM photographs of metal side of scale/metal interface on Fe–25 wt.% Cr–20 wt.% Ni ternary after exposure to oxygen/sulfur environment with $pS_2 > pS_2$ for Fe–FeS equilibrium

Figures 52 and 53 show the alloy and scale sides of the scale/metal interface for an Fe–25 wt.% Cr–20 wt.% Ni–3 wt.% Zr alloy after preoxidation and preoxidation/sulfur exposure, respectively, at 875°C. In the preoxidized specimen, ZrO_2 developed profusely and grew into the alloy (see Fig. 52) and the underside of the Cr_2O_3 scale was almost fully covered with ZrO_2. In the sulfur-exposed specimen, the Cr_2O_3 scale (see Fig. 53) was very smooth and the enrichment of Zr along the grain boundaries (see EDAX mapping in Fig. 53) and growing into the alloy is evident. Furthermore, neither interfacial voids nor sulfur were detected in the interface region.

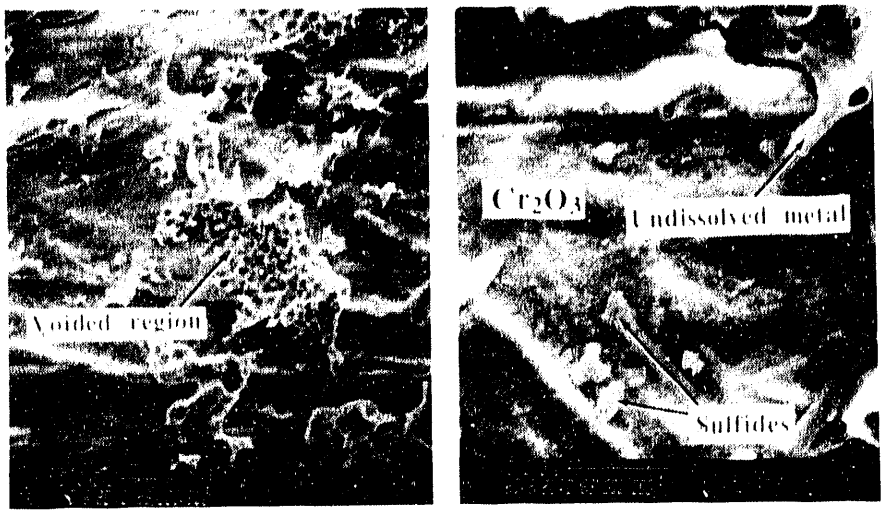

Fig. 49. SEM micrographs of scale side of scale/metal interface on Fe-25 wt.% Cr-20 wt.% Ni ternary alloy after exposure to oxygen/sulfur environment with $pS_2 > pS_2$ for Fe-FeS equilibrium

4 Thermal Cycling Tests

Exposure of metallic components to elevated temperatures in fossil-energy systems almost invariably results in an interaction between the constituents of a gaseous atmosphere and the surfaces of structural alloys. Ideally, the amount of alloy/gas interaction should be negligible, but at best a slow-growing surface scale will form and be retained, ensuring a low rate of alloy degradation. Low parabolic rates of surface oxide scale growth generally result in acceptable metal wastage rates, but unfortunately, the low rates of scale growth can usually be maintained only if the exposure temperature remains reasonably constant. In practice, experience shows that temperature cycling frequently causes a breakdown in protection of the surface scale because of the combination of (1) a wide mismatch in physical properties of an alloy and its thermally formed oxide scale and (2) the relatively low ductility of oxide scales. Once a scale is mechanically damaged, the alloy, which is depleted in protective oxide-forming element(s), may not be capable of reforming a new protective scale. Moreover, the presence of aggressive species such as chlorine in the gaseous atmosphere can exacerbate the problem. Loss of protection can be induced by the introduction of sulfur to normally oxidizing atmospheres even if temperature is held constant.[15,58] Clearly, the combination of temperature cycling and the presence of sulfur would be expected to increase the rate of the degradation process.

In coal-gasification and -combustion environments, oxygen and sulfur compete in reactions to form surface scales on component materials. Under the most severe conditions, a fast-growing sulfide scale normally leads to an inadequate level of protection for the underlying alloy. Therefore, selection of alloys is based on their ability to form an oxide scale in the exposure environment. However, fluctuations in temperature can affect the delicate balance between regimes of protective and nonprotective scale growth. Two aspects affecting protective scale stability were examined in O_2/S_2 mixed-gas environments. First, the effect of thermal cycling was addressed. Second, the effect of alloy

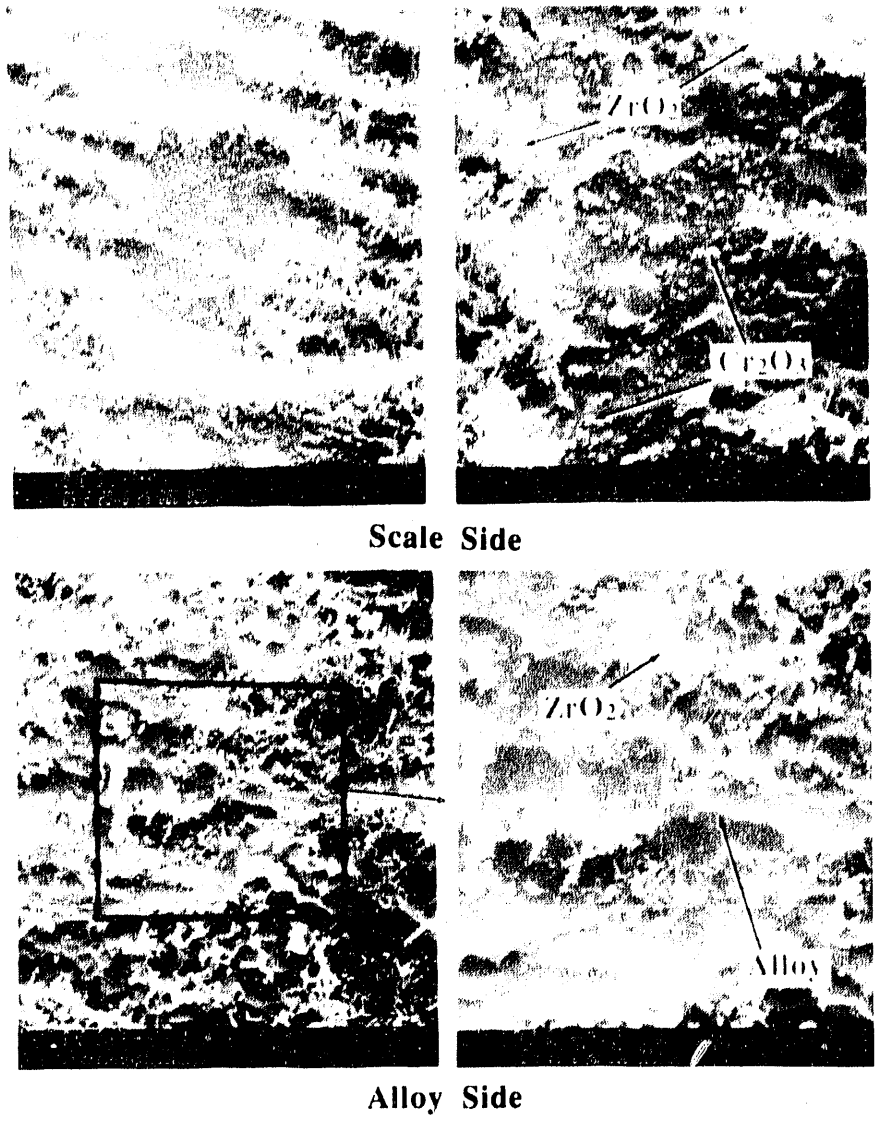

Fig. 50. SEM micrographs of scale and metal sides of scale/metal interface for Fe–25 wt.% Cr–20 wt.% Ni–3 wt.% Zr specimen after exposure to oxygen/sulfur environment with $pS_2 > pS_2$ for Fe–FeS equilibrium

composition, in particular additions of Zr or Nb to Fe–25 wt.% Cr–20 wt.% Ni alloy, was studied because additions of these elements enhance protective scale formation and promote scale stability in O_2/S_2 mixed-gas atmospheres. Specimens were exposed simultaneously to cycling temperature conditions and to a gas mixture containing oxygen and sulfur. Equilibrium partial pressures of oxygen and sulfur in the exposure environment were 2.2×10^{-18} and 3.2×10^{-8} atm, respectively, at the exposure temperature of 875°C. Thermal cycling consisted of repeated periods of heating to 875°C in 2 h, holding at 875°C for 16 h, and slow cooling to 200°C. Cycles were repeated every 24 h and specimens were weighed and examined after 3, 6, 11, 17, 23, and 28 cycles.

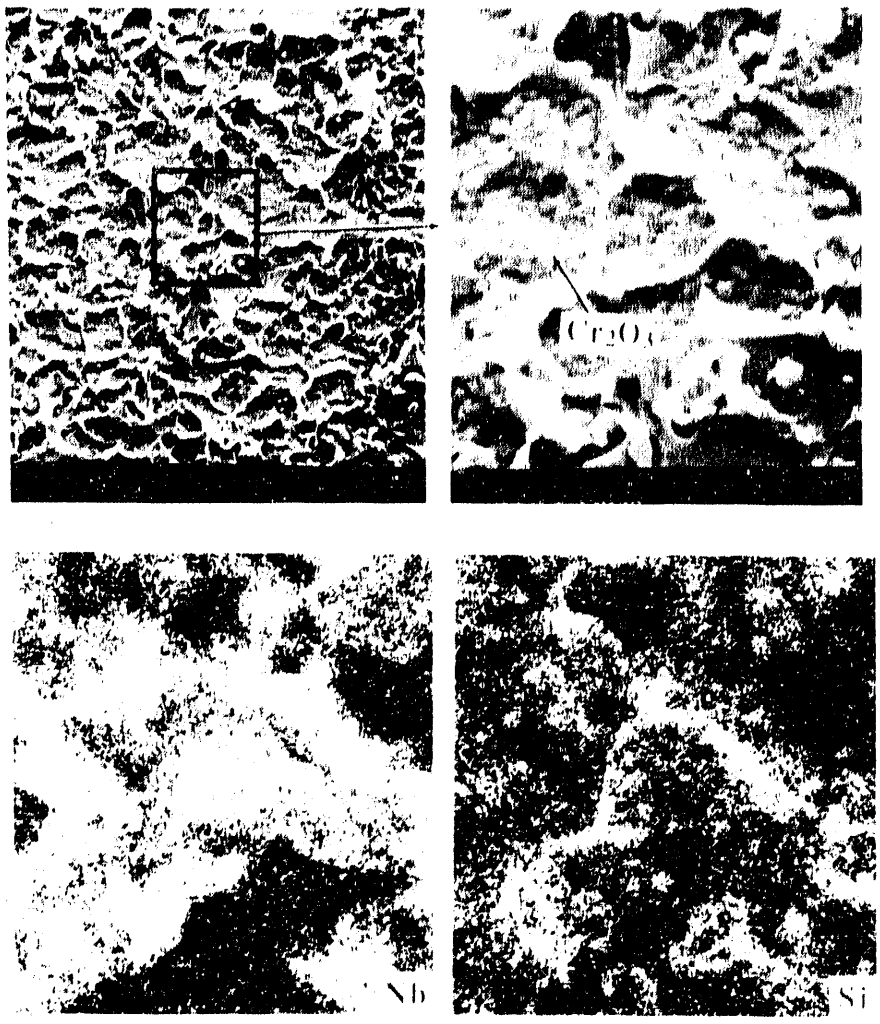

Fig. 51. SEM micrographs of scale side of scale/metal interface of Fe-25 wt.% Cr-20 wt.% Ni-3 wt.% Nb alloy after exposure at 1000°C to oxygen/sulfur environment with $pS_2 > pS_2$ for Fe-FeS equilibrium

Because thermal cycling involves exposure of alloys to a range of temperatures, it is important to consider the relative position of the threshold boundaries for the alloys under consideration with respect to the oxygen and sulfur partial pressures of the gas mixture used in the study. Both pO_2 and pS_2 of a given gas mixture decrease with decreasing temperature, while the displacement between the thermodynamic equilibrium Cr_2O_3/"CrS" and the threshold pO_2 for oxidation increases. The result is that while oxidation occurs at 875°C, a decrease in temperature causes a shift to the sulfidation regime. The composition dependence of the position of the threshold boundary naturally results in the shift in corrosion behavior occurring at different temperatures for different alloys. The transition occurs for the unmodified 25 wt.% Cr alloy at ≈750°C, compared with 600°C for the 3 wt.% Zr/Nb alloys. Thus, even if mechanical disruption of the oxide scale can be avoided during thermal cycling, the increased sulfidizing potential of the gas mixture may alone result in loss of protection. Given that protective oxide scaling initially occurs at 875°C and that mechanical

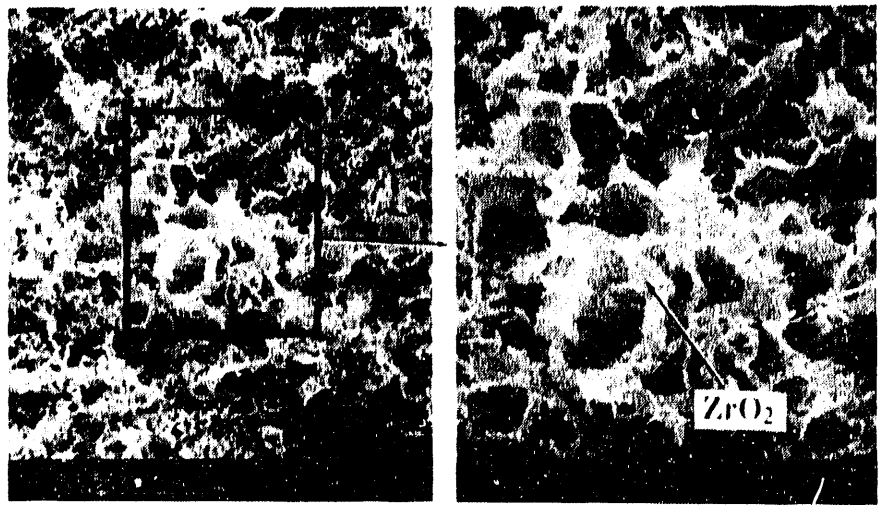

Fig. 52. SEM micrographs of scale side of scale/metal interface on Fe–25 wt.% Cr–20 wt.% Ni–3 wt.% Zr alloy after preoxidation in low-pO_2 environment at 875°C

defects are not induced by thermal cycling, the incubation time prior to breakdown of the oxide scale will determine whether breakaway can be avoided before the temperature is again raised to a level where oxidation can occur. In this way, the ability of preformed oxide scales to resist breakdown, as discussed earlier in this report, will be important.

Figures 54 and 55 show the weight-change data for Zr- and Nb-modified alloys, respectively, determined after various times of exposure. In each case, the data are compared with those for commercial Type 310 stainless steel.

4.1 Zr–Modified Alloys

For alloys containing 25 wt.% Cr, an increase in Zr content induced progressively smaller net weight changes (see Fig. 54). Examination of the specimens showed little spalling of surfaces that were covered predominantly with either oxide or sulfide. Short-term isothermal tests confirmed that all alloys formed scales dominated by growth of Cr-rich oxide with the presence of small, discrete Cr-rich sulfide nodules on the outer surface. However, while the 3 wt.% Zr alloy was able to maintain an intact oxide scale, oxide on the 1 and 0 wt.% Zr alloys invariably experienced loss of protection manifest by the formation of sulfide blisters on the outer surface of the oxide. Blisters occurred more frequently at specimen edges than on flat surfaces, which tends to suggest a mechanical contribution to the breakdown process due to inherently higher stresses prevalent at edges and further magnification of these stresses due to thermal cycling.

In the early stages after the initiation of breakaway sulfidation, sulfides were mainly Cr-rich and Fe became the dominant sulfide-former as the blisters grew vertically and laterally, eventually impinging on one another. In the advanced stages of breakaway sulfidation, the first-formed oxide apparently offered negligible resistance to alloy degradation. The alloy containing 12 wt.% Cr and 6 wt.% Zr performed measurably better than did the 25 wt.% Cr–1 wt.% Zr alloy and, in general, after an initial relatively sharp increase in weight, resisted the near catastrophic rate of degradation exhibited by the latter alloy. High Zr

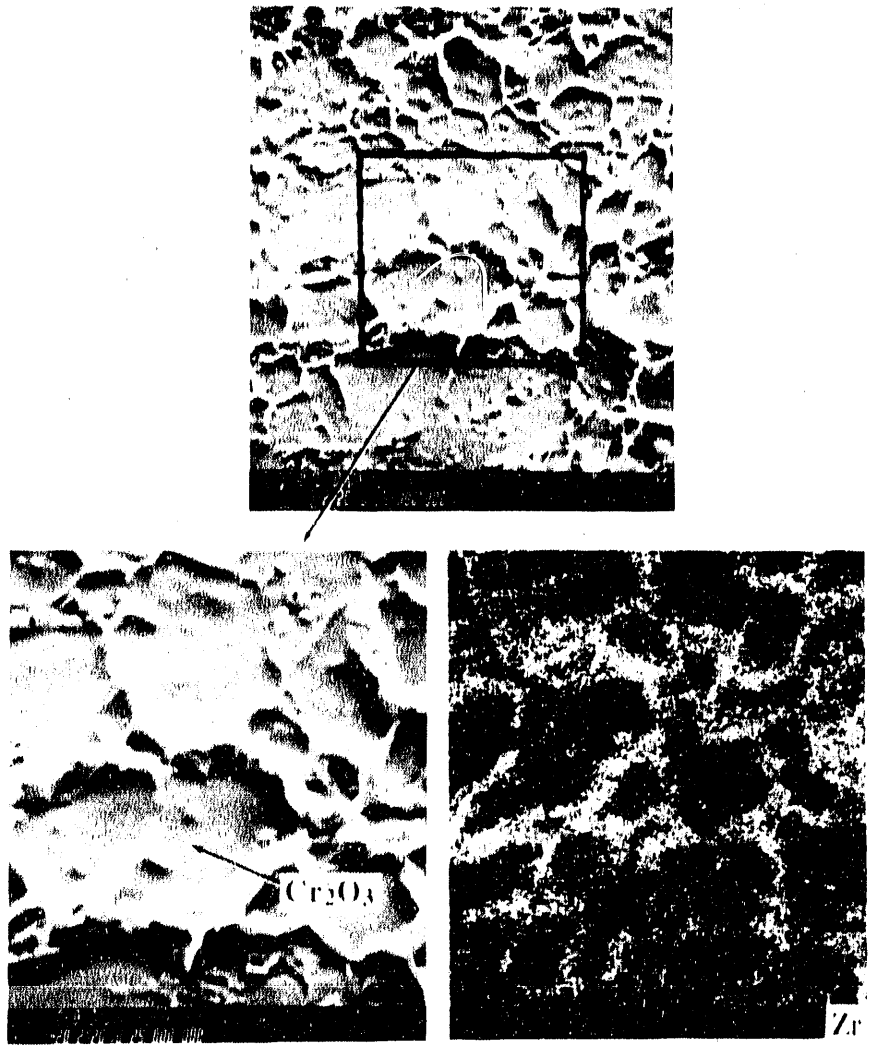

Fig. 53. SEM micrographs of scale side of scale/metal interface on preoxidized Fe–25 wt.% Cr–20 wt.% Ni–3 wt.% Zr specimen after exposure to oxygen/sulfur environment with $pS_2 > pS_2$ for Fe–FeS equilibrium

concentrations proved to be an effective sink for sulfur by inhibiting sulfur ingress into the alloy substrate and promoting stability of the surface oxide scale by delaying total breakdown of protection despite the presence of small sulfide nodules from the early stages of exposure. The scales on the Zr-modified alloys exhibited greater resistance to spallation than the scale on the commercial Type 310 stainless steel.

4.2 Nb–Modified Alloys

Internal intergranular sulfidation was a normal feature of all the Nb-modified alloys, although the depth decreased with smaller amounts of surface sulfidation, reflecting the beneficial effect of increasing Nb content. The alloy with 12 wt.% Cr and 6 wt.% Nb performed similarly to the 25 wt.% Cr and 1 wt.% Nb alloy. While the weight increases of the Nb-modified alloys were generally lower than those of the corresponding Zr-modified alloys, the weight-change trends exhibited by the two alloy families were similar.

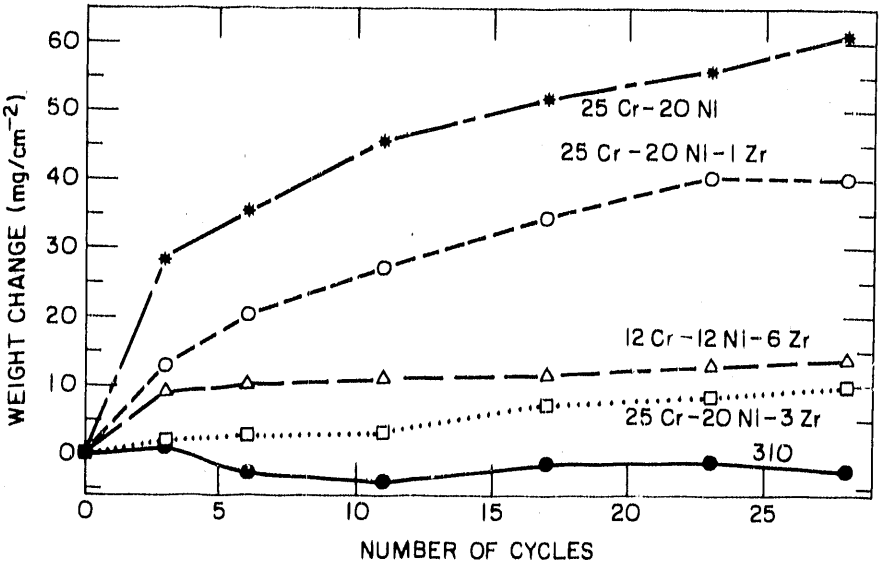

Fig. 54. Weight-change data for Zr-modified alloys determined after various exposure times under thermal cycling

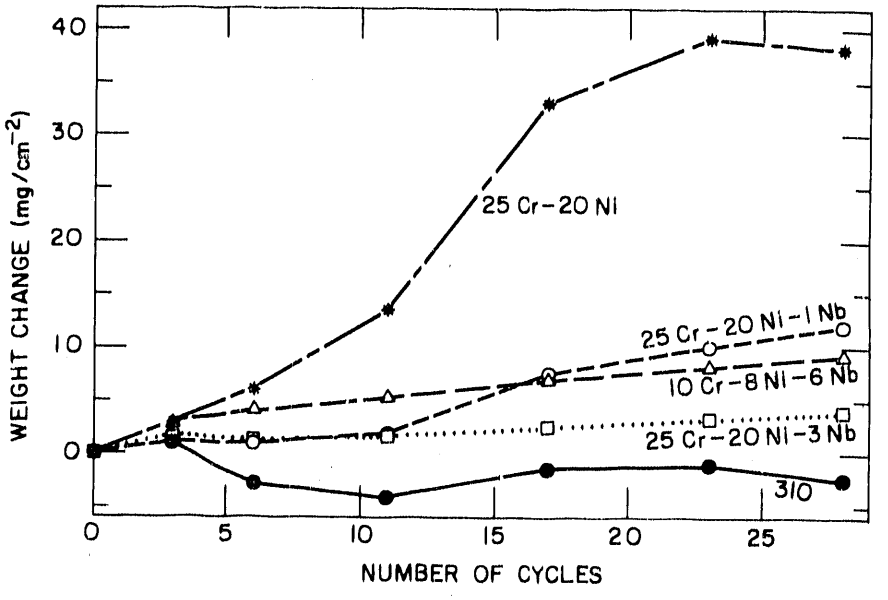

Fig. 55. Weight-change data for Nb-modified alloys determined after various exposure times under thermal cycling

5 Summary

The oxidation and oxidation/sulfidation behavior of Fe-Cr-Ni alloys with additions of Nb or Zr was investigated in air, low partial pressures of oxygen (pO_2), and mixed oxygen/sulfur environments. Based on the results from this study, a number of conclusions can be made.

The minimum pO_2 for protective oxide scale formation on the Zr- or Nb-free, 25 wt.% Cr alloy is $\approx 10^4$ to 10^3 times that defining thermodynamic equilibrium between Cr_2O_3 and sulfides of Cr at temperatures between 650 and 1000°C.

Alloying additions of Zr or Nb pushed the threshold pO_2 to lower levels; e.g., a 6 wt.% addition to the 25 wt.% Cr alloy decreases the threshold pO_2 by 1.5 orders of magnitude. Addition of refractory metals also reduced the depth of internal sulfidation.

While a Cr content of 12 wt.% is insufficient to support protective scale formation in a sulfur-free, low-pO2 environment at 875°C, an addition of more than 1 wt.% Nb or 3 wt.% Zr enabled a protective scale to form. Additions of these elements also promoted improved scale adhesion.

The major beneficial influence of Nb and Zr was their ability to promote the formation of a continuous external layer of Cr_2O_3 while forming a layer of Nb- or Zr-oxide at the scale/metal interface. This internal layer acts as barrier to transport of base-metal cations outward and anions inward, thereby extending the time before breakaway corrosion ensues.

Preformed oxide scales delay the onset of breakaway corrosion upon exposure to a sulfur-containing gas.

Preformed single-layer oxide scales rapidly sulfidized in ≈50 h of exposure to oxygen/sulfur mixed-gas atmospheres; in contrast, nonpreoxidized alloys exhibited immediate breakaway corrosion.

The presence of a two-layer oxide scale on the 3 wt.% Nb-modified alloy inhibited breakaway corrosion in sulfur-containing atmospheres in 150-h tests, pushing the threshold boundary for oxide formation and maintenance to a pO_2 that is approximately one order of magnitude lower.

The mechanism of breakaway in sulfur-containing atmospheres of preformed oxide scales appears to be dominated by mechanical defects associated primarily with specimen edges and corners.

Thermal cycling can result in repeated exposures to regimes of oxidation at high temperatures and sulfidation at lower temperatures. The temperature for transition from oxidation to sulfidation and vice versa is dependent on alloy composition: 750°C for Fe-25 wt.% Cr-20 wt.% Ni ternary alloy, and 600°C for the 3 wt.% Zr/Nb-added alloys.

The severity of corrosive attack during thermal cycling is dependent on alloy composition, with increasing resistance to breakaway corrosion promoted by increased Nb/Zr content in the 25 wt.% Cr alloys.

The beneficial effect of the barrier layer is dependent on the diffusion rate of the alloying addition. At temperatures of <875°C, alternative approaches to surface modification via sputter-deposition and ion implantation may facilitate formation of protective oxide scales.

Acknowledgments

This work was supported by the U.S. Department of Energy, Office of Fossil Energy, Advanced Research and Technology Development Materials Program, Work Breakdown Structure Element ANL-3, under Contract W-31-109-Eng-38. The authors acknowledge the Fabrication Technology Section of the Materials and Components Technology Division at Argonne for its assistance in the fabrication of the alloys. D. L. Rink and R. W. Pucetti assisted in the corrosion tests and microstructural analysis of the exposed specimens. A. Philippides and R. W. Pucetti assisted with in-situ tests in the HVEM.

References

1. T. C. Tiearney, Jr., and K. Natesan, *Metallic Corrosion in Simulated Low-Btu Coal-Gasification Atmospheres*, J. Mater. Energy Syst. 1, 13 (1980).

2. K. Natesan and M. B. Delaplane, *Oxidation-Sulfidation Behavior of Materials for Use in Coal-conversion Systems*, Proc. Symp. on Corrosion-Erosion Behavior of Materials, Fall Mtg. of TMS-AIME, October 1978, ed. K. Natesan (Warrendale, PA: The Metallurgical Society of AIME), 1 (1980).

3. K. Natesan, *High Temperature Alloy Corrosion in Coal Conversion Environments*, Proc. Symp. High Temperature Corrosion, San Diego, CA, ed. R. A. Rapp, NACE, 336 (1983).

4. T. C. Tiearney, Jr., and K. Natesan, *Sulfidation-Oxidation Behavior of Advanced Metallic Materials in Simulated Low-Btu Coal-Gasifier Environments*, Oxid. Met. 17, 1 (1982).

5. R. C. Lobb and H. E. Evans, *An Evaluation of the Effect of Surface Chromium Concentration on the Oxidation of a Stainless Steel*, Corros. Sci. 23, 55 (1983).

6. D. J. Baxter and K. Natesan, *Oxidation-Sulfidation Behavior of Fe-Cr-Ni-Zr Alloys in Mixed-Gas Environments*, Proc. Symp. Corrosion in Fossil Fuel Systems, ed. I. G. Wright, The Electrochemical Society, Vol. 83-5, 213 (1983).

7. D. Delaunay, A. M. Huntz, and P. Lacombe, *Mechanical Stresses Developed in High Temperature Resistant Alloys During Isothermal and Cyclic Oxidation Treatments: The Influence of Yttrium Additions on Oxide Scale Adherence*, Corros. Sci. 20, 1109 (1980).

8. G. R. Wallwork and A. Z. Hed, *The Oxidation of Ni-20%Cr-2%ThO_2*, Oxid. Met. 3, 229 (1971).

9. C. S. Giggins and F. S. Pettit, *The Oxidation of TD NiCr Between 900 and 1200°C*, Met. Trans. 2, 1071 (1971).

10. D. J. Baxter and K. Natesan, *Mechanical Considerations in the Degradation of Structural Materials in Aggressive Environments at High Temperatures*, Rev. High-Temp. Mater. 5, 149 (1983).

11. T. T. Huang, *Formation of Aluminum Oxide Scales in Sulfur-containing High Temperature Environments*, Metall. Trans. A, 16A, 2051 (1985).

12. K. Natesan, *Materials Technology for Coal Conversion Processes, Semiannual Report*, Argonne National Laboratory Reports ANL/FE-82-13 (for period October 1981-March 1982) and ANL/FE-82-23 (for period April-September 1982) (1982).

13. K. Natesan and S. J. Dapkunas, *Oxidation-Sulfidation Behavior of Materials in Coal Conversion Environments*, Proc. JIMIS-3 Conf. Supplement to Trans. Japan Inst. Metals, 24, 411 (1983).

14. R. A. Perkins, W. C. Coons, and S. J. Vonk, *Materials Problems in Fluidized-bed Combustion and Coal Gasification Systems*, Electric Power Research Institute Report EPRI-CS-2452 (1982).

15. F. H. Stott, F. M. F. Chong, and C. A. Stirling, *Effectiveness of Preformed Oxides for Protection of Alloys in Sulfidizing Gases at High Temperature*, Proc. 9th Intl. Congress Metallic Corrosion, National Research Council, Canada, Vol. 2, 1 (1984).

16. J. T. Prater and D. R. Baer, *High Temperature Corrosion in Coal Gasification Systems*, Proc. Symp. Corrosion in Fossil Fuel Systems, ed. I. G. Wright, The Electrochemical Society, Vol. 83-5, 202 (1983).

17. K. Natesan, *High-Temperature Corrosion in Coal Gasification Systems*, Corrosion, 41(11), 646 (1985).

18. M. LaBranche, A. Garrett-Reed, and G. J. Yurek, *Early Stages of the Oxidation of Chromium in $H2$-H_2O-H_2S Gas Mixtures*, J. Electrochem. Soc., 130(12), 2405 (1983).

19. K. Natesan, *Oxidation of Alloys in Bioxidants*, Proc. N. L. Peterson Memorial Symp. on Oxidation of Metals and Associated Mass Transport, Orlando, FL, October 6-7, 1986, eds. M. Dayananda, S. J. Rothman, and W. E. King, TMS-AIME, 161 (1987).

20. K. Natesan and D. J. Baxter, *Oxygen-Sulfur Corrosion of Metals in Mixed-Gas Atmospheres*, Proc. Conf. Corrosion-Erosion-Wear of Materials at Elevated Temperatures, Berkeley, CA, January 27-29, 1986, ed. A. V. Levy, NACE, 1 (1987).

21. R. A. Perkins and M. S. Bhat, *Sulfidation-Resistant Alloy for Coal Gasification Service*, Lockheed Palo Alto Research Laboratories, FE-2299-12 (1977).

22. K. Natesan, *Alloy Performance in Coal Gasification Environments*, Proc. Symp. Materials for Coal Gasification. ASM Metals Congress, Cincinnati, October 10-15, 1987, eds. W. T. Bakker, S. J. Dapkunas, and V. Hill, ASM, 51 (1988).

23. I. Barin and O. Knacke, *Thermochemical Properties of Inorganic Substances*, Springer-Verlag, New York (1973).

24. W. D. Halstead, *A Review of Saturated Vapor Pressures and Allied Data for the Principal Corrosion Products of Fe, Cr, Ni, and Co in Flue Gases*, Corros. Sci. 15, 603 (1975).

25. E. A. Gulbransen and G. H. Meier, *Thermochemical Stability Diagrams for Condensed Phases and Volatility Diagrams for Volatile Species over Condensed Phases in Twenty Metal-Sulfur-Oxygen Systems Between 1150 and 1450 K*, U.S. Department of Energy Report DOE/FE/13547-01 (1980).

26. H. Hindam and D. P. Whittle, *Microstructure, Adhesion, and Growth Kinetics of Protective Scales on Metals and Alloys*, Oxid. Metals, 18, 245 (1982).

27. P. Moulin, F. Armanet, G. Beranger, and P. Lacombe, *Relation Entre La Structure des Alliages Ni-Cr 80/20 et Leur Comportement a L'Oxydation a Haute Temperature*, Mem. Sci. Rev. Metall. 143 (1977).

28. K. H. Akram and W. W. Smeltzer, *The High Temperature Oxidation Kinetics of Zirconium*, Can. Metall. Quarterly, 1, 41 (1962).

29. S. Floreen and R. H. Kane, *Elevated Temperature Fatigue Crack Growth in Incoloy 800 in Sulfidizing Environments*, Metall. Trans. 134, 145 (1982).

30. S. Mrowec, T. Werber, and M. Zasawnik, *The Mechanism of High Temperature Sulfur Corrosion of Ni-Cr Alloys*, Corros. Sci. 6, 47 (1966).

31. B. R. Conrad, R. Sridhar, and J. S. Warner, *High Temperature Enthalpies of Ni Sulfides*, Paper Presented at 106th Annual AIME Meeting, Atlanta, March 7-11, 1977.

32. D. Bhogeswara Rao and H. G. Nelson, *Influence of Temperature and the Role of Cr on the Kinetics of Sulfidation of 310 Stainless Steel*, Oxid. Metals, 12, 111 (1978)

33. J. M. Francis, *Influence of Minor Alloying Elements on the Structure of Surface Oxides Formed During High Temperature Oxidation of an Austenitic Steel*, J. Iron Steel Inst., 204, 910 (1966).

34. K. H. VanHeek, W. Wanzl, A. Gala, and G. Kalwa, *Materials for Steam Gasification of Coal with HTR Heat*, Rev. Int. Hautes Temp. Refract., 13, 217 (1976).

35. J. M. Francis and J. A. Jutson, *The Role of Silicon in Determining the Oxidation Resistance of a 20Cr-25Ni-Nb Stabilized Steel*, CEGB Report RD/B/N989, U.K.

36. D. J. Baxter, R. C. Hurst, and R. T. Derricott, *The Influence of Silicon and Yttrium on the Scaling Behavior of an Austenitic Fe-Cr-Ni Alloy Under Athermal Conditions*, Werkstoffe und Korrosion, 35, 266 (1984).

37. M. Hansen and K. Anderko, *Constitution of Binary Alloys*, McGraw Hill, New York (1958).

38. R. P. Elliott, *Constitution of Binary Alloys*, First Supplement, McGraw Hill, New York (1965).

39. D. J. Baxter and K. Natesan, *The Corrosion Behavior of Fe-Cr-Ni-Zr Alloys in Coal Gasification Environments at High Temperatures*, Corr. Sci. 26, 153 (1986).

40. D. J. Baxter and K. Natesan, *The Oxidation/Sulfidation Behavior of Fe–Cr–Ni–Nb Alloys at Elevated Temperatures*, Proc. Third Berkeley Conf. on Corrosion–Erosion–Wear of Materials at Elevated Temperatures, Berkeley, CA, January 27–29, 1986, ed. A. V. Levy (NACE, Houston, 1987), 309.

41. A. U. Seybolt, *Sulfur Diffusion through Cr_2O_3 at 1000°C*, Trans. Metall. Soc. AIME, 242, 752 (1968).

42. J. B. Wagner, Jr., *Electrical Conductivity, Diffusion, and Minority Defects in Some Transition–metal Oxides*, in Defects and Transport in Oxides, eds. M. S. Seltzer and R. I. Jaffee, Plenum, New York, 283 (1974).

43. W. C. Hagel and A. U. Seybolt, *Cation Diffusion in Cr_2O_3*, J. Electrochem. Soc. 108, 1146 (1961).

44. W. C. Hagel, *Anion Diffusion in Cr_2O_3*, J. Am. Ceram. Soc. 48, 70 (1965).

45. P. Singh and N. Birks, *Penetration of Sulfur Through Preformed Protective Oxide Scales*, Oxid. Met. 19, 37 (1983).

46. R. H. Chang, W. Stewart, and J. B. Wagner, Jr., *Diffusion of Sulfur–35 in NiO and CoO*, Symp. Reactivity of Solids, eds. J. S. Anderson, M. W. Roberts, and F. S. Stone, Chapman and Hall Publishers, U.K., p. 231 (1972).

47. F. C. Yang and D. P. Whittle, *Sulfur Diffusion in Oxide Grain Boundaries*, Corr. Sci. 23, 285 (1983).

48. J. B. Johnson, J. R. Nicholls, R. C. Hurst and P. Hancock, *The Mechanical Properties of Surface Oxides on Nickel–base Superalloys–I. Oxidation*, Corr. Sci. 18, 527 (1978).

49. W. F. Chu and A. Rahmel, *The Scaling of Metals in Oxygen– and Sulfur–containing Atmospheres*, Rev. High Temp. Mat. 4, 139 (1979).

50. T. T. Huang, B. Peterson, D. A. Shores, and E. Pfender, *XPS and EES Studies of the High Temperature Corrosion Mechanism of Fe–30Cr Alloy*, Corr. Sci. 24, 167 (1984).

51. G. Romeo and H. S. Spacil, *Effect of Pre–Existing Oxide on the High–Temperature Sulfidation of Chromium*, Proc. Symp. High Temperature Gas–Metal Reactions in Mixed Environments (TMS–AIME, Boston, 1972), 299.

52. G. Romeo, H. S. Spacil, and W. J. Pasko, *The Transport of Chromium in Cr_2O_3 Scales in Sulfidizing Environments*, J. Electrochem. Soc. 122, 1329 (1975).

53. D. Mortimer and M. L. Post, *The Oxidation of Cr and Fe–50%Cr Alloy*, Corr. Sci. 8, 499 (1968).

54. R. C. Lobb and H. E. Evans, *Observations on the Effect of Low Sulfur Activity on the Oxidation of Chromium–depleted Zones in a Stainless Steel*, Oxid. Met. 16, 371 (1981).

55. J. D. Noden, C. J. Knights, and M. W. Thomas, *Growth of Austenitic Stainless Steels Oxidized in Carbon and Oxygen Bearing Gases*, Br. Corr. J. 3, 47 (1968).

56. Y. Ikeda, K. Nii, and K. Yoshihara, *High Temperature Oxidation and Surface Segregation of Sulfur*, Trans. Jpn. Inst. Met. Suppl. 24, 207 (1983).

57. J. G. Smeggil, A. W. Funkenbusch, and N. S. Bornstein, *A Relationship Between Indigeneous Impurity Elements and Protective Oxide Scale Adherence Characteristics*, Metall. Trans. 17A, 923 (1986).

58. D. J. Baxter and K. Natesan, *Breakdown of Chromium Oxide Scales in Sulfur-Containing Environments at Elevated Temperatures*, Oxid. Met. 31 305 (1989).

END

DATE FILMED

01 / 30 / 91